

NUMERICAL SIMULATIONS OF INCOMPRESSIBLE AND COMPRESSIBLE  
TRANSITIONAL TURBINE FLOWS

A Thesis  
Submitted to the Graduate Faculty  
of the  
North Dakota State University  
of Agriculture and Applied Science

By

Jamison Jared Huber

In Partial Fulfillment  
for the Degree of  
MASTER OF SCIENCE

Major Department:  
Mechanical Engineering

December, 2013

Fargo, North Dakota

North Dakota State University  
Graduate School

---

**Title**

Numerical Simulations of Incompressible and Compressible Transitional  
Turbine Flows

---

**By**

Jamison Jared Huber

---

The Supervisory Committee certifies that this *disquisition* complies with North Dakota  
State University's regulations and meets the accepted standards for the degree of

**MASTER OF SCIENCE**

SUPERVISORY COMMITTEE:

Dr. Bora Suzen

---

Chair

Dr. Ghodrat Karami

---

Dr. Sumathy Krishnan

---

Dr. Om Yadav

---

Approved:

4/15/2014

---

Date

Dr. Alan R. Kallmeyer

---

Department Chair

## **ABSTRACT**

Accurate and reliable turbulence and transition models are needed for prediction heating loads in the hot section of the turbine, and predicting aerodynamic losses when designing new blade profiles. Two dimensional compressible flow simulations were conducted at North Dakota State University on a first stage turbine vane design. Surface pressure results were compared with experimental data collected at the University of North Dakota. Results showed an under prediction of the surface pressure on the suction surface of the vane. Two and three dimensional compressible flow simulations were also conducted at NDSU on an incident tolerant blade design to look at the effect of incidence angle, Reynolds number, and turbulence intensity on transition. Results from these simulations were compared with experimental data collected at UND. The results show good agreement at higher Reynolds numbers with discrepancies being seen on the suction surface of the blade at lower Reynolds numbers.

## **ACKNOWLEDGMENTS**

I would first like to thank with extreme gratitude my advisor Dr. Bora Suzen, for this opportunity and for the continual support that he has given me over the past few years. Without his help and support this accomplishment would not have been possible.

I would like to thank Dr. Ghodrat Karami, Dr. Sumathy Krishnan, and Dr. Om Yadav for taking time and being part of my graduate committee.

I would like to thank Kelsey Kolars for her continuous motivation and encouragement, and Alex Flage for his help in conducting the simulations.

Lastly, I owe my parents for where I am and what I have accomplished. Without their constant support and motivation I would not be where I am today.

# TABLE OF CONTENTS

|   |      |
|---|------|
| ABSTRACT.....   | iii  |
| ACKNOWLEDGMENTS .....   | iv   |
| LIST OF TABLES.....   | vii  |
| LIST OF FIGURES .....   | viii |
| NOMENCLATURE .....  | xiii |
| 1. INTRODUCTION AND RESEARCH OBJECTIVES .....   | 1    |
| 2. TURBULENCE AND TRANSITION REVIEW.....  | 3    |
| 2.1. Turbulent Flow.....  | 3    |
| 2.2. Laminar to Turbulent Flow Transition .....   | 11   |
| 3. TURBULENCE AND TRANSITION MODELING.....  | 18   |
| 3.1. Turbulence Modeling.....   | 18   |
| 3.2. Transition Modeling using Intermittency .....  | 23   |
| 4. UND EXPERIMENTAL INVESTIGATION OF THE INFLUENCE OF TURBULENCE<br>INTENSITY AND REYNOLDS NUMBER ON TURBINE FLOWS..... | 32   |
| 4.1. UND Incompressible Flow Experiments .....  | 32   |
| 4.2. UND Compressible Flow Experiments .....  | 34   |
| 5. SIMULATIONS OF THE INFLUENCE OF TURBULENCE INTENSITY AND<br>REYNOLDS NUMBER ON TURBINE FLOWS .....                   | 36   |
| 5.1. Incompressible Flow Simulations of (Kingery, Suzen, & Ames, 2010) .....  | 36   |
| 5.2. Compressible Flow Simulations .....  | 41   |
| 6. UND EXPERIMENTAL INVESTIGATION OF AN INCIDENT TOLERANT BLADE<br>DESIGN.....  | 48   |
| 7. SIMULATIONS OF AN INCIDENT TOLERANT BLADE DESIGN.....  | 51   |
| 7.1. Two Dimensional Simulations.....   | 51   |
| 7.2. Three Dimensional Simulations.....   | 64   |
| 8. CONCLUSIONS AND FUTURE WORK.....   | 86   |

|   |    |
|---|----|
| 8.1. Conclusions.....   | 86 |
| 8.2. Future Work.....   | 88 |
| 9. REFERENCES.....  | 89 |
| APPENDIX.....   | 96 |
| A.1. MATLAB script for creating two dimensional geometry.....     | 96 |
| A.2. MATLAB script for creating three dimensional case plots..... | 99 |

# LIST OF TABLES

| <u>Table</u>   | <u>Page</u> |
|--|-------------|
| 4.1: Experiment Details and Turbulence Parameters (Ames, Argenziano, & Wang, 2004) ..... | 34          |
| 6.1: Tabulated List of Simulations to be Conducted.....                                  | 50          |

## LIST OF FIGURES

| <u>Figure</u>   | <u>Page</u> |
|---|-------------|
| 2.1: Schematic of Large Eddies In Turbulent Boundary Layer (Wilcox, 2000).....                                    | 4           |
| 2.2: Instantaneous and Averaged Velocity Profiles (Wilcox, 2000) .....  | 8           |
| 2.3: Natural Stages of Transition (White, 2006).....  | 12          |
| 2.4: Separated-flow Transition Stages (De Palma, 2006).....   | 13          |
| 2.5: Unsteady Wake Propagation Through Blade Row (Mayle, 1991) .....  | 14          |
| 3.1: Re <sub>v</sub> Profile for Blasius Boundary Layer (Menter & Langtry, 2012) .....                            | 26          |
| 4.1: Incompressible Flow Vane Cascade Details (Ames, Argenziano, & Wang, 2004) .....                              | 33          |
| 4.2: Layout of Cascade Test Section (Ames, Argenziano, & Wang, 2004) .....  | 33          |
| 4.3: Compressible Flow Vane Cascade Details (Mihelish & Ames, 2013).....  | 35          |
| 5.1: Incompressible Mesh with Detail .....  | 37          |
| 5.2: Computed vs Experimental Pressure Distribution.....  | 38          |
| 5.3: Low Turbulence (LC) Case Heat Transfer Coefficient (Kingery, Suzen, & Ames, 2010) .....                      | 39          |
| 5.4: Catalytic Combustor (CC) Case Heat Transfer Coefficient (Kingery, Suzen, & Ames, 2010) .....                 | 39          |
| 5.5: Grid Case Heat Transfer Coefficient (Kingery, Suzen, & Ames, 2010) .....                                     | 40          |
| 5.6: Aeroderivative Combustor with Spool (ACS) Case Heat Transfer Coefficient (Kingery, Suzen, & Ames, 2010)..... | 40          |
| 5.7: Aeroderivative Combustor (AC) Case Heat Transfer Coefficient (Kingery, Suzen, & Ames, 2010) .....            | 41          |
| 5.8: Dry Low NO <sub>x</sub> (DLN) Case Heat Transfer Coefficient (Kingery, Suzen, & Ames, 2010) ....             | 41          |
| 5.9: 2D Compressible Vane Geometry - Side View .....  | 42          |
| 5.10: 2D Compressible Vane Geometry - Isometric View .....  | 42          |



|  |    |
|--|----|
| 5.11: 2D Compressible Vane Mesh with Detail .....                  | 43 |
| 5.12: Surface Distance Diagram .....                               | 44 |
| 5.13: Re=90K, Low Turbulence Pressure Plot .....                   | 45 |
| 5.14: Re=90K, High Turbulence Pressure Plot.....                   | 45 |
| 5.15: Re=180K, Low Turbulence Pressure Plot .....                  | 46 |
| 5.16: Re=180K, High Turbulence Pressure Plot.....                  | 46 |
| 5.17: Re=360K, Low Turbulence Pressure Plot .....                  | 46 |
| 5.18: Re=360K, High Turbulence Pressure Plot.....                  | 46 |
| 5.19: Re=720K, Low Turbulence Pressure Plot .....                  | 47 |
| 5.20: Re=720K, High Turbulence Pressure Plot.....                  | 47 |
| 6.1: NASA LCTR Vehicle (Snyder, 2012).....                         | 48 |
| 6.2: Experimental SolidWorks Models.....                           | 49 |
| 6.3: 34° Experimental Surface Pressure Data for Blade 2 .....      | 50 |
| 7.1: Side and Isometric View of the Two Dimensional Geometry.....  | 52 |
| 7.2: Two Dimensional Blocking Layout.....                          | 53 |
| 7.3: Two Dimensional Mesh with Detail.....                         | 53 |
| 7.4: Two Dimensional Simulation Boundary Conditions.....           | 54 |
| 7.5: Surface Distance Diagram and Front Pressure Tap Location..... | 55 |
| 7.6: Preliminary 40° Two Dimensional Pressure Distribution .....   | 56 |
| 7.7: Preliminary 34° Two Dimensional Pressure Distribution .....   | 56 |
| 7.8: Preliminary 28° Two Dimensional Pressure Distribution .....   | 56 |
| 7.9: Preliminary 18° Two Dimensional Pressure Distribution .....   | 56 |
| 7.10: Preliminary 8° Two Dimensional Pressure Distribution .....   | 57 |

|  |    |
|--|----|
| 7.11: Preliminary -2° Two Dimensional Pressure Distribution .....                          | 57 |
| 7.12: Preliminary -12° Two Dimensional Pressure Distribution .....                         | 57 |
| 7.13: Preliminary -17° Two Dimensional Pressure Distribution .....                         | 57 |
| 7.14: Pressure Distribution for All Incidence Angles with Transition Model Active .....    | 58 |
| 7.15: Pressure Distribution for All Incidence Angles without Transition Model Active ..... | 58 |
| 7.16: Final Two Dimensional Boundary Conditions .....                                      | 59 |
| 7.17: Re = 50K, Final Two Dimensional Surface Pressure Plot.....                           | 61 |
| 7.18: Re = 66K, Final Two Dimensional Surface Pressure Plot.....                           | 61 |
| 7.19: Re = 228K, Final Two Dimensional Surface Pressure Plot.....                          | 61 |
| 7.20: Re = 568K, Final Two Dimensional Surface Pressure Plot.....                          | 61 |
| 7.21: 34° Two Dimensional Re=50K Mach Contour for Simulated Cascade .....                  | 62 |
| 7.22: 34° Two Dimensional Re=50K Mach Contour Blade Zoom-in .....                          | 62 |
| 7.23: 34° Two Dimensional Re=66K Mach Contour for Simulated Cascade .....                  | 62 |
| 7.24: 34° Two Dimensional Re=66K Mach Contour Blade Zoom-in .....                          | 62 |
| 7.25: 34° Two Dimensional Re=228K Mach Contour for Simulated Cascade .....                 | 63 |
| 7.26: 34° Two Dimensional Re=228K Mach Contour Blade Zoom-in .....                         | 63 |
| 7.27: 34° Two Dimensional Re=568K Mach Contour for Simulated Cascade .....                 | 63 |
| 7.28: 34° Two Dimensional Re=568K Mach Contour Blade Zoom-in .....                         | 63 |
| 7.29: Geometry Components .....  | 64 |
| 7.30: Flowfield Schematic .....  | 65 |
| 7.31: Coarse Mesh Used in Mesh Refinement Study .....                                      | 66 |
| 7.32: Intermediate Mesh Used in Mesh Refinement Study .....                                | 67 |
| 7.33: Fine Mesh Flowfield with Body of Influence.....                                      | 68 |

|  |    |
|--|----|
| 7.34: Fine Mesh Used in Mesh Refinement Study .....                                | 69 |
| 7.35: Loss Coefficient Plane Locations .....                                       | 71 |
| 7.36: Fully Turbulent Surface Pressures Using Coarse Mesh .....                    | 72 |
| 7.37: Fully Turbulent Surface Pressures Using Intermediate Mesh .....              | 72 |
| 7.38: Fully Turbulent Surface Pressures Using Fine Mesh .....                      | 72 |
| 7.39: Surface Pressures Using Coarse Mesh with Transition Model Active .....       | 73 |
| 7.40: Surface Pressures Using Intermediate Mesh with Transition Model Active ..... | 73 |
| 7.41: Surface Pressures Using Fine Mesh with Transition Model Active .....         | 73 |
| 7.42: Loss Coefficient Contours Using Coarse Mesh.....                             | 74 |
| 7.43: Loss Coefficient Contours Using Intermediate Mesh.....                       | 74 |
| 7.44: Loss Coefficient Contours Using Fine Mesh.....                               | 74 |
| 7.45: 40° Surface Blade Pressures .....  | 75 |
| 7.46: 34° Surface Blade Pressures .....  | 75 |
| 7.47: 28° Surface Blade Pressures .....  | 76 |
| 7.48: 18° Surface Blade Pressures .....  | 76 |
| 7.49: 8° Surface Blade Pressures .....   | 76 |
| 7.50: -2° Surface Blade Pressures .....  | 76 |
| 7.51: -12° Surface Blade Pressures.....  | 77 |
| 7.52: -17° Surface Blade Pressures.....  | 77 |
| 7.53: Downstream Mach Number Diagram.....  | 78 |
| 7.54: 34° Re=50K Initial and Adjusted Downstream Mach Number Comparison .....      | 80 |
| 7.55: Re=66K Initial and Adjusted Downstream Mach Number Comparison.....           | 80 |
| 7.56: 34° Re=228K Initial and Adjusted Downstream Mach Number Comparison .....     | 80 |

|  |    |
|--|----|
| 7.57: Re=568K Initial and Adjusted Downstream Mach Number Comparison.....            | 80 |
| 7.58: Re=50K Blade Surface Pressure Distributions.....                               | 81 |
| 7.59: Re=50K Blade Surface Pressure Distributions with Two Dimensional Results.....  | 81 |
| 7.60: Re=66K Blade Surface Pressure Distributions.....                               | 81 |
| 7.61: Re=66K Blade Surface Pressure Distributions with Two Dimensional Results.....  | 81 |
| 7.62: Re=228K Blade Surface Pressure Distributions.....                              | 82 |
| 7.63: Re=228K Blade Surface Pressure Distributions with Two Dimensional Results..... | 82 |
| 7.64: Re=568K Blade Surface Pressure Distributions.....                              | 82 |
| 7.65: Re=568K Blade Surface Pressure Distributions with Two Dimensional Results..... | 82 |
| 7.66: Re=50K Center Plane Mach Number Contour.....                                   | 83 |
| 7.67: Re=50K Center Plane Mach Contour with Wall Shear Contour on Blade 2.....       | 83 |
| 7.68: Re=66K Center Plane Mach Number Contour.....                                   | 83 |
| 7.69: Re=66K Center Plane Mach Contour with Wall Shear Contour on Blade 2.....       | 83 |
| 7.70: Re=228K Center Plane Mach Number Contour.....                                  | 84 |
| 7.71: Re=228K Center Plane Mach Contour with Wall Shear Contour on Blade 2.....      | 84 |
| 7.72: Re=568K Center Plane Mach Number Contour.....                                  | 84 |
| 7.73: Re=568K Center Plane Mach Contour with Wall Shear Contour on Blade 2.....      | 84 |
| 7.74: Re=50K Loss Coefficients.....  | 85 |
| 7.75: Re=66K Loss Coefficients.....  | 85 |
| 7.76: Re=228K Loss Coefficients.....   | 85 |
| 7.77: Re=568K Loss Coefficients.....   | 85 |

## NOMENCLATURE

- $c$  = chord length, m
- $C_f$  = skin friction,  $\frac{\tau_w}{\frac{1}{2}\rho_\infty U_\infty^2}$
- $C_p$  = pressure coefficient,  $\frac{(p_{total}-p)}{\frac{1}{2}\rho_\infty U_\infty^2}$
- $FSTI$  = free stream turbulence intensity
- $h$  = heat transfer coefficient, W/m<sup>2</sup>-K
- $K_t$  = flow acceleration parameter,  $\left(\frac{v}{U^2}\right)\left(\frac{dU}{ds}\right)$
- $L_{ref}$  = reference length
- $P_s$  = static pressure, Pa
- $P_t$  = total pressure, Pa
- $q''$  = heat flux from blade surface, W/m<sup>2</sup>
- $Re$  = Reynolds number,  $\frac{\rho_\infty U_\infty L_{ref}}{\mu_\infty}$
- $s$  = surface arc length, m
- $T_{ke}$  = turbulent kinetic energy, m<sup>2</sup>/s<sup>2</sup>
- $u'$  = streamwise fluctuation velocity, m/s
- $U$  = streamwise velocity, m/s
- $U_{in}$  = inlet velocity, m/s
- $U_{exit}$  = exit velocity, m/s
- $U_\infty$  = freestream velocity, m/s
- $\gamma$  = intermittency factor
- $\varepsilon$  = turbulent dissipation rate,  $-\frac{dk}{dt}$ , m<sup>2</sup>/s<sup>3</sup>

- $\theta$  = momentum thickness
- $\rho_\infty$  = freestream density, kg/m<sup>3</sup>
- $\mu_\infty$  = freestream molecular viscosity, Pa-s
- $\mu_t$  = eddy viscosity
- $\nu$  = kinematic viscosity,  $\frac{\mu}{\rho}$ , m<sup>2</sup>/s
- $\omega$  = turbulent eddy frequency, s<sup>-1</sup>
- $\omega_{loss}$  = loss coefficient,  $\frac{P_{in} - P_{total}}{P_{in}}$

# 1. INTRODUCTION AND RESEARCH OBJECTIVES

With the rising oil prices in recent years and the “green” movement, research efforts in lowering emissions and increasing efficiency of gas turbines has increased, which has led to new combustor technology and designs. Many of these new designs increase the turbulent mixing of the flow to improve the combustion process. This increase in the turbulence intensity directly leads to a higher turbulence level and a substantial increase in heat transfer distributions in the hot section of the gas turbine, primarily the first stage vanes of the high pressure turbines (Anderson, 2011) (Ames, Wang, & Barbot, 2003) (Ames F. , 1997). At higher altitudes and cruising speeds (when the turbines are not under high load), drops in efficiency has been observed and can be partially attributed to flow separation on the suction side of the blades. Accurately modeling turbulence to predict heat transfer and losses is one of the more important and difficult aspects of turbine design. In order to calculate heat transfer and losses, a designer must have tools that are able to predict boundary layer development, through the transition region, and into the turbulent regime (Glassman, Whitney, & Steward, 1994) (Mayle, 1991).

The  $\gamma$ - $Re_{\theta}$  transition model has been show to give good results in a wide area of transitional flows. However, the model has shown deficiency in high turbulence high Reynolds number flows, like the flows found in the hot section of a gas turbine. This is where this research on the  $\gamma$ - $Re_{\theta}$  hopes to improve the accuracy in these high turbulence high Reynolds number flows.

The goal of this research is the following:

1. Testing and validation of turbulence and transition models for compressible turbine vane flows

2. Testing and validation of turbulence and transition models for compressible flows of an incident tolerant blade design

The testing and validation of these cases can help identify areas of improvement of the transition model. These cases can also provide a base for future model refinement and improvement.



## **2. TURBULENCE AND TRANSITION REVIEW**

### **2.1. Turbulent Flow**

Most flows of interest for engineering applications are by their nature considered to be turbulent. Turbulence consists of random velocity fluctuations and contains an almost infinite range of eddy sizes and length scales. Because of the complex nature of turbulence, it remains to be an unsolved problem to researchers and engineers.

#### **2.1.1. Turbulence Background**

Turbulence is considered to be a highly complex, three-dimensional, non-linear, and time dependent phenomenon. Many different definitions of turbulence can be found in literature, but it has shown to be a rather difficult task to come up with a definition that encompasses all of the different aspects of turbulence. One of the more common informal definitions was given by Richardson in 1922 and states “Big whorls have little whorls which feed on their velocity; and little whorls have lesser whorls and so on to viscosity” (Richardson, 1922). This definition gives a good overview in describing how turbulence is a continuum phenomenon and contains essentially infinite number of scales. A formal definition given by Hinze gives a good summary of how turbulence consists of random fluctuations both in time and space and can be statistically averaged (Hinze, 1959). The definition by Hinze is says “Turbulent fluid motion is an irregular condition of the flow in which the various quantities show a random variation with time and space coordinates, so that statically distinct average values can be discerned” (Hinze, 1959).

The two previous definitions give a good overall definition of the main concept of turbulence.

As Richardson’s definition above stated that an almost infinite range of scales exist, they also coexist in turbulent flow, with the smaller scales inside of the larger scales. This wide range of sizes of turbulent eddies leads to an increase in vigorous mixing, which can be extremely large

when compared to laminar values. The term “eddies” can be defined of a local swirling motion whose characteristic dimension is the local turbulence scale. Figure 2.1 below shows a schematic of large eddies in a turbulent boundary layer.

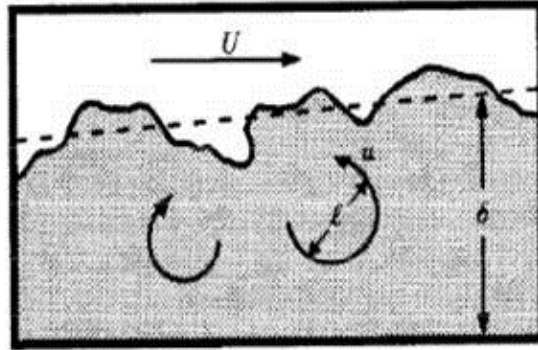


Figure 2.1: Schematic of Large Eddies In Turbulent Boundary Layer (Wilcox, 2000)

It can be seen that turbulence is a cascading process where as the turbulence decays, its kinetic energy transfers from the larger eddies to the smaller eddies. From this energy transfer it can be concluded that like any viscous flow turbulent flows are always dissipative.

### 2.1.2. Small Scales of Turbulence

From the above section, we can regard turbulence as a continuum phenomenon because even the smallest scales of turbulence are much larger than any molecular length scale. Since we know that turbulent flow is a cascading process where turbulent kinetic energy is transferred from larger eddies to smaller eddies, it can be determined that the dissipation of kinetic energy to heat thru molecular viscosity happens only at the smallest eddy scale, and that the rate at which the smaller eddies receive energy from the larger eddies is equal to the rate at which the smallest eddies dissipate the energy to heat. This is one of the main premises of Kolmogorov’s universal equilibrium theory (Kolmogorov, 1941). From this theory the motion at the smallest scales should only depends on the rate at which the larger eddies supply energy ( $\epsilon$ ), and the kinematic viscosity ( $\nu$ ).

Knowing that  $\varepsilon$  and  $\nu$  are the appropriate dimensional quantities, the length ( $\eta$ ), time ( $\tau$ ), and velocity ( $v$ ) scales can be developed and are as follows:

$$\eta \equiv \left(\frac{\nu^3}{\varepsilon}\right)^{\frac{1}{4}}, \quad \tau \equiv \left(\frac{\nu}{\varepsilon}\right)^{\frac{1}{2}}, \quad v \equiv (\nu\varepsilon)^{\frac{1}{4}} \quad (2.1)$$

These are the known as the Kolmogorov scales of length, time, and velocity (Wilcox, 2000).

### 2.1.3. Governing Equations of Motion

The basic equations for motion are the conservation of mass, conservation of momentum, and the conservation of energy equations. The momentum equations are referred to the Navier-Stokes equations, and are named after the two scientists who derived them independently.

Equation (2.2) below is the complete mass conservation equation, and equations (2.3), (2.4), and (2.5) are the x, y, and z momentum conservation equations.

$$\frac{\partial \rho}{\partial t} + \left[ \frac{\partial(\rho u)}{\partial x} + \frac{\partial(\rho v)}{\partial y} + \frac{\partial(\rho w)}{\partial z} \right] = 0 \quad (2.2)$$

$$\frac{\partial u}{\partial t} + u \frac{\partial u}{\partial x} + v \frac{\partial u}{\partial y} + w \frac{\partial u}{\partial z} = \frac{1}{\rho} \left[ -\frac{\partial p}{\partial x} + \frac{\partial \tau_{xx}}{\partial x} + \frac{\partial \tau_{yx}}{\partial y} + \frac{\partial \tau_{zx}}{\partial z} \right] \quad (2.3)$$

$$\frac{\partial v}{\partial t} + u \frac{\partial v}{\partial x} + v \frac{\partial v}{\partial y} + w \frac{\partial v}{\partial z} = \frac{1}{\rho} \left[ -\frac{\partial p}{\partial y} + \frac{\partial \tau_{xy}}{\partial x} + \frac{\partial \tau_{yy}}{\partial y} + \frac{\partial \tau_{zy}}{\partial z} \right] \quad (2.4)$$

$$\frac{\partial w}{\partial t} + u \frac{\partial w}{\partial x} + v \frac{\partial w}{\partial y} + w \frac{\partial w}{\partial z} = \frac{1}{\rho} \left[ -\frac{\partial p}{\partial z} + \frac{\partial \tau_{xz}}{\partial x} + \frac{\partial \tau_{yz}}{\partial y} + \frac{\partial \tau_{zz}}{\partial z} \right] \quad (2.5)$$

If these equations are rearranged and rewritten into vector form, they then take the form of

$$\frac{D\rho}{Dt} + \rho \operatorname{div} \mathbf{V} = 0 \quad (2.6)$$

$$\rho \frac{D\mathbf{V}}{Dt} = \rho g - \nabla p + \frac{\partial}{\partial x_j} \left[ \mu \left( \frac{\partial v_i}{\partial x_j} + \frac{\partial v_j}{\partial x_i} \right) + \delta_{ij} \lambda \operatorname{div} \mathbf{V} \right] \quad (2.7)$$

If the flow is assumed to be incompressible, constant density ( $\rho$ ), and have constant viscosity ( $\mu$ ), the continuity equation (mass) and the Navier-Stokes equations (momentum) reduce and become much simpler (White, 2006). The incompressible flow forms of the continuity equation and the Navier-Stokes equations are as follows:

$$\operatorname{div} \mathbf{V} = 0 \quad (2.8)$$

$$\rho \frac{D\mathbf{V}}{Dt} = \rho g - \nabla p + \mu \nabla^2 \mathbf{V} \quad (2.9)$$

The conservation of energy equation is shown below in equation (2.10).

$$\rho \frac{D}{Dt} \left( e + \frac{p}{\rho} \right) = \frac{Dp}{Dt} + \operatorname{div}(k\nabla T) + \tau'_{ij} \frac{\partial u_i}{\partial x_j} \quad (2.10)$$

If the concept of enthalpy is used, and the dissipation function  $\Phi$  is introduced, which is defined as

$$\Phi = \tau'_{ij} \frac{\partial u_i}{\partial x_j} \quad (2.11)$$

Equation (2.11) can be rewritten as the following:

$$\rho \frac{Dh}{Dt} = \frac{Dp}{Dt} + \operatorname{div}(k\nabla T) + \Phi \quad (2.12)$$

Once again, if the flow is assumed to be incompressible, equation (2.12) can be simplified and written in terms of thermodynamic properties and is as follows:

$$\rho c_p \frac{DT}{Dt} \approx \text{div}(k\nabla T) \quad (2.13)$$

Simplifying further, if constant thermal conductivity is assumed, equation (2.13) can be reduced to obtain the familiar incompressible heat-convection equation (White, 2006):

$$\rho c_p \frac{DT}{Dt} \approx k\nabla^2 T \quad (2.14)$$

The derived equations above represent the basic laws of fluid motion for linear (Newtonian) fluids.

#### 2.1.4. Reynolds-Averaged Equations

From the previously given definition of turbulence it is known that turbulence consists of random fluctuations of various flow properties. Because of these fluctuating values, a statistical approach can be used. One of the most widely used statistical approaches was introduced by Reynolds in 1895, in which all quantities are expressed as the sum of mean and fluctuating parts. In other words

$$u(x) = \bar{u}(x) + u'(x) \quad (2.15)$$

where  $u$  is a random turbulent variable. The nonlinearity of the Navier-Stokes equations lead to the appearance of momentum fluxes that act as stresses throughout the flow. These stresses are unknown beforehand, therefore equations must be derived. These derived equations include additional unknown quantities. This problem of creating enough equations for all of the unknowns introduces what is known as the ‘‘Turbulent Closure Problem’’.

To analyze the complex behavior of turbulence, classical statistical methods are used. The averaging concept introduced by Reynolds in 1895 is the main statistical method used. Figure 2.2 below shows multiple velocity profiles taken at different times (left) and the averaged

velocity profile (right). This shows how averaging the fluctuations to a mean value can be of great benefit when looking at turbulent values.

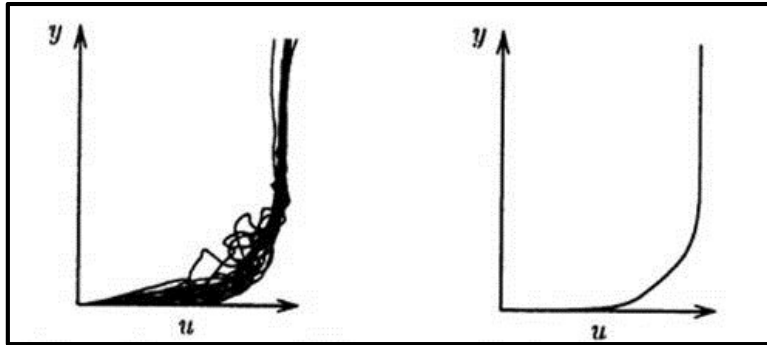


Figure 2.2: Instantaneous and Averaged Velocity Profiles (Wilcox, 2000)

The three most widely used forms of Reynolds averaging are the time average, spatial average, and the ensemble average (Wilcox, 2000). Time averaging, which in engineering is the most common form of Reynolds averaging, is used for stationary turbulence. Time averaging is the most common since most of the turbulent flows in engineering are stationary. Figure 2.2 above was obtained using time averaging. Let  $f(x, t)$  be an instantaneous flow variable, then its time average,  $F_T(x)$ , is defined by

$$F_T(x) = \lim_{T \rightarrow \infty} \frac{1}{T} \int_t^{t+T} f(x, t) dt \quad (2.16)$$

Spatial averaging is used for homogenous turbulence, which is turbulent flow that on average is uniform in all directions. This type of averaging is done by calculating a volume integral over all of the spatial coordinates. Let  $f(x, t)$  be an instantaneous flow variable, then its average,  $F_V$ , is defined by

$$F_V(t) = \lim_{V \rightarrow \infty} \frac{1}{V} \iiint_V f(x, t) dV \quad (2.17)$$

Ensemble averaging is the most general type of Reynolds averaging and is used for flows that decay in time (Wilcox, 2000). If  $N$  identical experiments are performed where  $f(x, t) = f_n(x, t)$  in the  $n^{\text{th}}$  experiment, the average,  $F_E$ , is given by

$$F_E(x, t) = \lim_{N \rightarrow \infty} \frac{1}{N} \sum_{n=1}^N f_n(x, t) \quad (2.18)$$

For turbulence that is both stationary and homogeneous, it can be assumed that all three of these averaging methods are all equal. Because they can be assumed equal, and time averaging is the most used in engineering, it will be used throughout the rest of this thesis. We will start with the incompressible and constant property flow form of the equations for the conservation of mass and momentum

$$\frac{\partial u_i}{\partial x_i} = 0 \quad (2.19)$$

$$\rho \frac{\partial u_i}{\partial t} + \rho u_j \frac{\partial u_i}{\partial x_j} = -\frac{\partial p}{\partial x_i} + \frac{\partial t_{ji}}{\partial x_j} \quad (2.20)$$

where  $u_i$  is velocity,  $x_i$  is position,  $t$  is time,  $p$  is pressure,  $\rho$  is density, and  $t_{ij}$  is the viscous stress tensor defined by

$$t_{ij} = 2\mu s_{ij} \quad (2.21)$$

where  $\mu$  is molecular viscosity and  $s_{ij}$  is the strain rate tensor,

$$s_{ij} = \frac{1}{2} \left( \frac{\partial u_i}{\partial x_j} + \frac{\partial u_j}{\partial x_i} \right) \quad (2.22)$$

Combining the previous equations and putting the convective term in conservation form, the Navier-Stokes equation becomes

$$\rho \frac{\partial u_i}{\partial t} + \rho \frac{\partial}{\partial x_j} (u_j u_i) = -\frac{\partial p}{\partial x_i} + \frac{\partial}{\partial x_j} (2\mu s_{ji}) \quad (2.23)$$

Time averaging equations (2.19) and (2.23) gives the Reynolds averaged equations of motion and they appear as the following:

$$\frac{\partial U_i}{\partial x_i} = 0 \quad (2.24)$$

$$\rho \frac{\partial U_i}{\partial t} + \rho \frac{\partial}{\partial x_j} (U_j U_i - \overline{u'_j u'_i}) = -\frac{\partial P}{\partial x_i} + \frac{\partial}{\partial x_j} (2\mu S_{ji}) \quad (2.25)$$

The only difference between these time averaged equations and the instantaneous equations above is the correlation  $\overline{u'_j u'_i}$ . In order to find all of the mean flow properties of the turbulent flow we need a method for calculating  $\overline{u'_j u'_i}$ .

Equation (2.25) can be rewritten into its more popular form and is shown below.

$$\rho \frac{\partial U_i}{\partial t} + \rho U_j \frac{\partial U_i}{\partial x_j} = -\frac{\partial P}{\partial x_i} + \frac{\partial}{\partial x_j} (2\mu S_{ji} - \rho \overline{u'_j u'_i}) \quad (2.26)$$

The resulting above equation is known as the ‘‘Reynolds-Averaged Navier-Stokes’’, or RANS, equation. The quantity  $-\rho \overline{u'_j u'_i}$  is called the ‘‘Reynolds-stress tensor’’ and can be denoted by  $\rho \tau_{ij}$ , where  $\tau_{ij}$  is the ‘‘specific Reynolds stress tensor’’ and is given by (Wilcox, 2000).

$$\tau_{ij} = -\overline{u'_i u'_j} \quad (2.27)$$

If the number of unknowns (10) is compared with the number of equations (4) we see that we have more unknowns than equations, which means our system is not closed. This is once again known as the ‘‘turbulence closure problem’’ and brings up the main function of turbulence



modeling, which is to devise approximations for the unknown correlations so enough equations exist to solve for all of the unknowns and close the system (Wilcox, 2000).

## **2.2. Laminar to Turbulent Flow Transition**

Generally there are considered three important modes of wall bounded transition. The first and most commonly thought of mode of transition is called “natural” transition. This mode of transition is initiated by a weak instability in the laminar boundary layer. This instability grows and progresses through numerous stages until it develops into fully turbulent flow (Schlichting, 1979). The second mode of transition, called “bypass” transition, is the most common mode in gas turbines and is caused by disturbances in the external flow. These disturbances include the free stream turbulence and pressure gradient (Morkovin, 1969). The third general type of transition is known as “separated-flow” transition. Transition in this mode occurs in the separated laminar boundary layer and may or may not include T-S (Tollmien-Schlichting) waves. This mode is most prevalent in the low pressure turbine section in gas turbines. Different modes of transition can occur at the same time at different locations on the same surface.

### **2.2.1. Modes of Transition**

The three general modes of transition are natural transition, bypass transition, and separated-flow transition. Bypass transition, separated-flow transition, and “periodic unsteady” transition flows make up the majority of the observed transitional flows in turbomachinery.

#### **2.2.1.1. Natural Transition**

Natural transition begins when the momentum thickness Reynolds number reaches a critical value and the laminar boundary layer becomes susceptible to small disturbances. These small disturbances then develop into two dimensional instabilities called Tollmien-Schlichting

(T-S) waves. These T-S waves then are amplified to a point where three dimensional instabilities progress into large fluctuations, then further develop into turbulent spots. These turbulent spots grow and coalesce into a fully developed turbulent boundary layer (Schlichting, 1979) (Mayle, 1991). Figure 2.3 below shows the stages of natural transition.

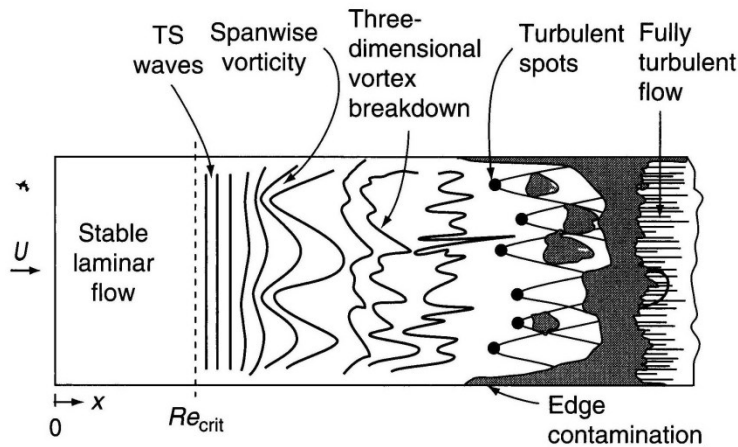


Figure 2.3: Natural Stages of Transition (White, 2006)

### 2.2.1.2. Bypass Transition

Due to the high free stream turbulence intensity levels, pressure gradients, and other large free stream disturbances, the initial stages of natural transition are completely skipped, or “bypassed”, and turbulent spots are directly produced (Mayle, 1991). Kachanov mentions that this type of transition is connected with direct nonlinear laminar-flow breakdown under the influence of large external disturbances, such as free stream disturbances and surface roughness (Kachanov, 1994). Bypass transition is a very common mode of transition in gas turbines (Mayle & Schulz, 1996).

### 2.2.1.3. Separated-Flow Transition

Separated-flow transition occurs when the laminar boundary layer separates from the surface. When this happens, transition occurs in the separated shear layer near the surface. The

flow may reattach as turbulent flow. This separation and reattachment creates a “bubble” of recirculating flow on the surface. This transition usually occurs in over speed regions near the leading edge and near the minimum pressure point on the suction surface. The bubble size or “length” depends mainly on the transition process in the shear layer. The transition over the separation bubble can include all of the stages of natural transition. Figure 2.4 below shows the stages of this transition and a separation bubble. Being able to control the size of the separation bubble (keeping it smaller) can be an effective way of forcing the flow to become turbulent (Mayle, 1991). Separated-flow transition is common in the lower Reynolds number sections of the gas turbine, mainly the low pressure turbine (LPT).

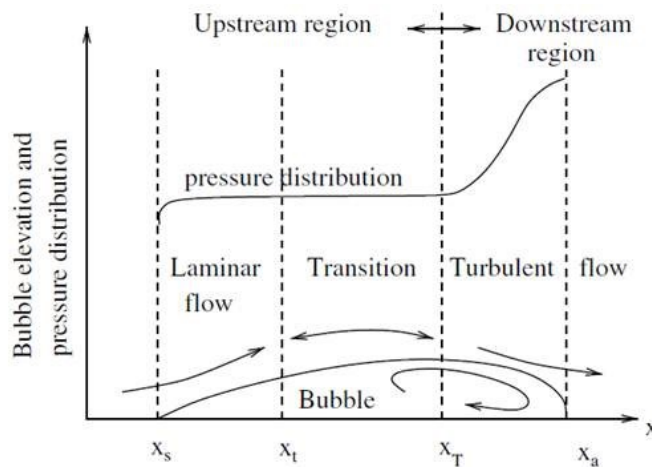


Figure 2.4: Separated-flow Transition Stages (De Palma, 2006)

#### 2.2.1.4. Periodic-Unsteady Transition

Periodic-unsteady transition occurs in gas turbines because the flow is by nature periodically unsteady. The main source of unsteadiness is caused by the periodic passing of wakes from upstream blades. This type of periodic unsteady transition is called “wake-induced” transition. Figure 2.5 below shows the unsteady wake propagation through a blade row.

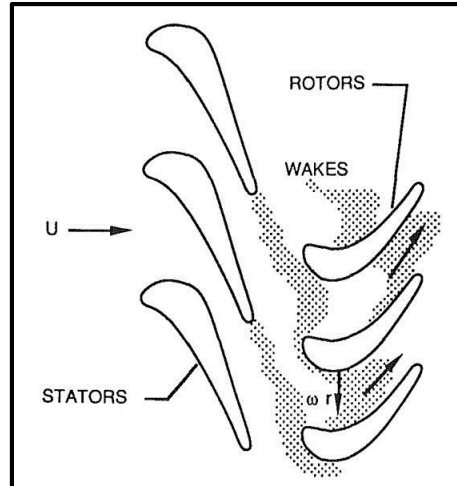


Figure 2.5: Unsteady Wake Propagation Through Blade Row (Mayle, 1991)

Shocks from upstream blades can also cause periodic unsteadiness and cause transition. Periodic-unsteady transition tends to bypass the initial stages of natural transition and instead turbulent spots form and immediately coalesce into a turbulent strip that propagates downstream (Mayle, 1991). When this bypass transition occurs flow separation can often be suppressed. At a single instance, the flow on the blade surface can include laminar flow, turbulent spots, separated flow transition, bypass transition of an attached boundary layer, and reattachment (Kaszeta, Simon, & Asphis, 2001).

#### 2.2.1.5. Reverse Transition

Reverse transition, or “relaminarization”, occurs when the flow transitions from turbulent flow to laminar flow. This type of transition usually occurs in flow through nozzles with strong accelerations. This is because near the trailing edge of the suction surface and near the leading edge of the pressure surface the acceleration values are usually higher than the values where relaminarization occurs. Relaminarization consists of a balance between convection, production, and dissipation of turbulent kinetic energy in the boundary layer (Mayle, 1991).

## **2.2.2. Factors Affecting Flow Transition**

Transition is affected by many factors, which include the pressure gradient, free stream turbulence intensity (FSTI), compressibility, surface roughness, and surface curvature. Many other factors can affect transition, but the previously mentioned play the largest role in affecting the different parameters of transition, which include the onset of transition, transition length, separation, and reattachment. Details of the major factors affecting transition will be detailed in the following sections.

### **2.2.2.1. Pressure Gradient**

When transition occurs in the bypass mode, the acceleration parameter at transition is more appropriate for flows with a favorable pressure gradient. The transition Reynolds number ( $Re_{\theta t}$ ) increases with increasing acceleration or a decrease in the FSTI. At lower turbulence levels, the acceleration parameter has a significant effect, however for higher turbulence levels (as in levels found in gas turbines), the acceleration parameter is negligible and the onset of transition is controlled by the free-stream turbulence (Mayle, 1991). Under strong adverse pressure gradients transition occurs rapidly. As the pressure gradient changes from a zero gradient to an adverse level, or even a moderate level, the transition length is substantially shortened. Measurements have shown an exponential decrease in transition length with increasing adverse pressure gradients.

### **2.2.2.2. Free Stream Turbulence**

When assessing the influence of turbulence on transition, it is important to consider the turbulence length scale and the turbulence level. At least three mechanisms have been found that show how free stream turbulence affects transition. These mechanisms include the modification of natural transition processes through two dimensional perturbations in free-stream velocity or

pressure gradient; bypass mechanisms resulting in the generation of streamwise vorticity within the boundary layer through three dimensional disturbances; and the diffusion of turbulent kinetic energy from the free-stream into the boundary layer (Walker, 1993). A less severe exponential decrease (when compared to an increasing pressure gradient) in transition length is found with an increasing turbulence level (Gostelow, Blunded, & Walker, 1994).

### **2.2.2.3. Compressibility**

The majority of flows found in the bulk of the components in gas turbines are compressible. Two distinct effects are recognized when looking at compressibility effect. The first is the effect of the Mach number on the onset of transition and the length of transition. The second is the effect of a shockwave from an upstream blade forcing transition through boundary layer separation. As the Mach number increases the turbulent spot production rate is decreased, the onset of transition is delayed, and the transition length is increased by ~8-30%. When a shockwave is passed from an upstream blade it causes a small, concentrated vortex on the pressure surface of the blade near the leading edge. This vortex induces transition as it moves along the blade surface (Mayle, 1991).

### **2.2.2.4. Surface Roughness**

Surface roughness alters transition by altering the transition Reynolds number. Increasing the surface roughness decreases the transition Reynolds number which leads to transition occurring earlier. For high free stream turbulence levels, up to a 60% reduction in transition length is seen. A smaller surface roughness corresponds to a smaller transition alteration (Mayle, 1991).

### **2.2.2.5. Surface Curvature**

Depending on the strength of the curvature and the turbulence intensity, curvature can play an important role in transition. At lower turbulence intensities transition on a convex surface is only slightly delayed, however, transition on a concave surface can occur significantly earlier. At higher turbulence intensities, concave curvature can either decrease or increase the transition Reynolds number depending on the strength of curvature and turbulence intensity. Transition length on a convex surface can increase by up to ~10% (Mayle, 1991).

## 3. TURBULENCE AND TRANSITION MODELING

### 3.1. Turbulence Modeling

Advancements in computer technology and processing power have led to advancement in turbulence modeling. This section discusses and describes common turbulence modeling approaches and types.

#### 3.1.1. Model Levels

The three main approaches for turbulence modeling are Reynolds-Averaged Navier Stokes (RANS) equations, Direct Numerical Simulation (DNS), and Large Eddy Simulation (LES). Many industrial applications using computational fluid dynamics are based on RANS, which makes it the most commonly used computational technique. RANS models solve for the mean velocity flow field by modeling all of the scales in the turbulent flow. The DNS method solves the Navier-Stokes equations by resolving all of the length and time scales that appear in the turbulent flow. The LES method directly solves the large scale motions and models the small scale motions.

##### 3.1.1.1. RANS Zero-Equation Models

The RANS zero equation models, also known as algebraic models, are the simplest of the turbulence models. These models are based on Prandtl's mixing-length hypothesis and use the Boussinesq approximation for eddy-viscosity. In his mixing-length hypothesis, Prandtl visualized a simplified model for turbulent flow in which fluid particles coalesce into lumps that cling together and move as a single unit. In this hypothesis the lumps retain their  $x$ -directed momentum for a distance in the  $y$  direction,  $l_{mix}$ . This length,  $l_{mix}$ , Prandtl called the mixing length. The Boussinesq approximation is an analogy where the turbulent shear stress is related to the gradient of the mean flow velocity, or



$$\tau_t = \mu_t \frac{\partial \bar{u}}{\partial y} = \rho \nu_t \frac{\partial \bar{u}}{\partial y} \quad (3.1)$$

where  $\mu_t$ , or  $\nu_t$ , is the eddy viscosity (Hoffman & Chiang, 1998). Algebraic models are the simplest turbulence models, and work well only for flows for which they have been fine-tuned (Wilcox, 2000).

### 3.1.1.2. RANS One-Equation Models

RANS one-equation models retain the Boussinesq approximation, but are also based on the turbulent kinetic energy equation or an equation for the eddy viscosity. The one-equation models based on the equation for turbulent kinetic energy are rarely used since they are incomplete and only relate the turbulence length scale to some typical flow dimension. One-equation models based on an equation for eddy viscosity automatically provide the turbulence length and therefore are complete and are more commonly used. The Spalart-Allmaras model is one of the most common and most used one-equation eddy viscosity based models. This model includes eight closure coefficients and three closure functions (Wilcox, 2000).

### 3.1.1.3. RANS Two-Equation Models

RANS two-equation models have been the base for much of the turbulence model research that has been done during the last several decades. The two-equation models solve an equation for the turbulent kinetic energy,  $k$ , but also solve an additional equation for the turbulence length scale or equivalent variable (Wilcox, 2000). This makes the two-equation models complete. The turbulent kinetic energy equation is defined as:

$$k = \frac{1}{2} \overline{u'_i u'_i} = \frac{1}{2} (\overline{u'^2} + \overline{v'^2} + \overline{w'^2}) \quad (3.2)$$

The transport equation for the turbulent kinetic energy is as follows:

$$\frac{\partial k}{\partial t} + U_j \frac{\partial k}{\partial x_j} = \tau_{ij} \frac{\partial U_i}{\partial x_j} - \epsilon + \frac{\partial}{\partial x_j} \left[ \nu \frac{\partial k}{\partial x_j} - \frac{1}{2} \overline{u'_i u'_i u'_j} - \frac{1}{\rho} \overline{p' u'_j} \right] \quad (3.3)$$

where the dissipation per unit mass,  $\epsilon$ , is defined as:

$$\epsilon = \nu \frac{\partial u'_i}{\partial x_k} \frac{\partial u'_i}{\partial x_k} \quad (3.4)$$

The following three two-equation models all solve the above turbulent kinetic energy equation, but differ in the second equation that is solved. The following sections briefly discuss three popular two-equation models.

### 3.1.1.3.1. $k$ - $\epsilon$ Models

Many different variations of the  $k$ - $\epsilon$  model exist, but the standard  $k$ - $\epsilon$  model is based on the eddy viscosity concept, like some of the zero-equation models. The model assumes that the turbulent kinetic eddy viscosity is linked to the turbulent kinetic energy and dissipation by the following relation (Wilcox, 2000):

$$\nu_t = C_\mu \frac{k^2}{\epsilon} \quad (3.5)$$

where  $C_\mu$  is a constant. The transport equation for the turbulence dissipation rate is as follows:

$$\frac{\partial \epsilon}{\partial t} + U_j \frac{\partial \epsilon}{\partial x_j} = C_{\epsilon 1} \frac{\epsilon}{k} \tau_{ij} \frac{\partial U_i}{\partial x_j} - C_{\epsilon 2} \frac{\epsilon^2}{k} + \frac{\partial}{\partial x_j} \left[ \left( \nu + \frac{\nu_t}{\sigma_\epsilon} \right) \frac{\partial \epsilon}{\partial x_j} \right] \quad (3.6)$$

where

$$C_{\epsilon 1} = 1.44; \quad C_{\epsilon 2} = 1.92; \quad C_\mu = 0.09 \quad \sigma_\epsilon = 1.3 \quad (3.7)$$

### 3.1.1.3.2. $k$ - $\omega$ Models

As with the  $k$ - $\epsilon$  models, many different versions of the  $k$ - $\omega$  models exist. In the standard  $k$ - $\omega$  model, the second parameter,  $\omega$ , is the dissipation per unit turbulent kinetic energy. Since

the first  $k$ - $\omega$  model by Kolmogorov was derived, the  $\omega$  equation has evolved. A production term has been added to most models after the model by Kolmogorov. The turbulent kinematic eddy viscosity is linked with the turbulent kinetic energy by the following equation:

$$\nu_t = \frac{k}{\omega} \quad (3.8)$$

The transport equation for the specific dissipation rate is as follows:

$$\frac{\partial \omega}{\partial t} + U_j \frac{\partial \omega}{\partial x_j} = C_{\omega 1} \frac{\omega}{k} \tau_{ij} \frac{\partial U_i}{\partial x_j} - C_{\omega 2} \omega^2 + \frac{\partial}{\partial x_j} \left[ (\nu + \sigma \nu_t) \frac{\partial \omega}{\partial x_j} \right] \quad (3.9)$$

where

$$C_{\omega 1} = \frac{13}{25}; \quad C_{\omega 2} = \frac{9}{125} f_{\beta}; \quad \sigma = \frac{1}{2} \quad (3.10)$$

### 3.1.1.3.3. Shear Stress Transport Model

The Shear Stress Transport (SST) model is a  $k$ - $\omega$  based model that accounts for the transport of the turbulent shear stresses. This has been shown to give highly accurate results for the onset and amount of flow separation for adverse pressure gradients. The model tends to over-predict the eddy viscosity, but the correct transfer behavior can be found by using a limiting function in the formulation of the eddy viscosity. This formulation is as follows:

$$\nu_t = \frac{a_1 k}{\max(a_1 \omega, SF_2)} \quad (3.11)$$

where  $a_1$  is a constant,  $S$  is an invariant measure of the strain rate, and  $F_2$  is a blending function that restricts the limiting function to the wall boundary layer (Wilcox, 2000).

#### **3.1.1.4. Large Eddy Simulations**

Large eddy simulations (LES) are a combination of RANS and DNS. The large eddies in the flow are directly computed, like in DNS, and the small eddies are modeled. However, instead of time-averaging, like in RANS, LES uses a spatial filtering operation to distinguish between the larger and smaller eddies, and to filter out the scales smaller than the mesh size. There are many different types of filters that are used, but some of the more common filters are the volume-average box filter, the Fourier cutoff filter, and the Gaussian filter. The filter introduces a scale that represents the smallest turbulence scale that is allowed by the filter. Scales larger than this scale are called the resolvable scales, while scales smaller are called the subgrid scales (SGS). Modeling the subgrid scales, which make up a significant portion of the turbulence spectrum, is the fundamental problem of LES (Wilcox, 2000). With many of the latest SGS models showing great promise, and with the rise in computing power, the interest in LES is going to continue to grow.

#### **3.1.1.5. Hybrid Models**

##### **3.1.1.5.1. Detached Eddy Simulation**

Detached eddy simulation (DES) combines a RANS model in the boundary layer with a coarse-mesh LES after large scale separation (Wilcox, 2000). With the RANS model being used in the boundary layer, the mesh density is not as large as it would be when compared to only LES, which reduces the amount and cost of computations. Initially DES only used the Spalart-Allmaras one equation model, but can now be used with other RANS models.

### **3.1.1.5.2. Scale Adaptive Simulation**

Scale adaptive simulation (SAS) allows unsteady turbulent flow predictions by transitioning from an LES model through various steps of eddy-resolution back to a steady RANS model. SAS models commonly behave similar to DES models, but are not dependent on the grid spacing like DES models (Menter & Egorov, The Scale-Adaptive Simulation Method for Unsteady Turbulent Flow Predictions. Part 1: Theory and Model Description, 2010).

### **3.1.1.6. Direct Numerical Simulations**

Direct numerical simulations (DNS) completely solve the three dimensional and time dependent Navier-Stokes and continuity equations. This means that DNS can give numerically accurate solutions of the exact equations of motion, and can be called the “*proper solution to the turbulence problem*” (Wilcox, 2000). DNS of turbulent flow starts at a certain time and point, and develops a transient solution. The major downside of DNS is the large grid size that comes from the fine grid spacing required and small enough time steps to resolve the smallest eddies and fluctuations (Versteeg & Malalasekera, 2007). Throughout the 1980’s and 1990’s DNS greatly matured, and with the exponential growth of computing power and storage, the interest in and number of DNS is likely to continue to rapidly grow.

## **3.2. Transition Modeling using Intermittency**

There are mainly four general methods that transition models use and can be classified by. The first method is to use stability theory. In stability theory, stability equations are solved at streamwise locations to predict the onset of transition. This method calculates only the onset of transition and does not give any information about the turbulent part of the flow. This method also requires a prior solution of the mean flow field. The second method is using an empirical correlation of the form  $e^n$ . This method, like stability theory, requires a previous solution to the

flow field and neither of these two methods are compatible with current large scale unstructured grid CFD solving methods (Suzen, Huang, Hultgren, & Ashpis, 2001).

The third method, which is compatible with current unstructured grid CFD solvers, is the use of low-Reynolds number turbulence models. Experiments done by Westing and Henkes in 1997 and Savill in 1993 indicate that none of the low-Reynolds number turbulence models could predict both the onset of transition and transition length for a range of flow conditions. This outcome is not unexpected since most of the current turbulence models are not designed to predict flow transition. The fourth method, which is an alternative to the use of low-Reynolds number turbulence models, is to use the concept of intermittency ( $\gamma$ ) to blend the flow from the laminar to the turbulent regions. This concept of intermittency is the method of predicting transition that this thesis will be based on.

### **3.2.1. Model Development**

In 1996 Steelant and Dick (Steelant & Dick, 1996) proposed a transport equation for intermittency, in which the source term of the equation was developed so as to reproduce the intermittency distribution of Dhawan and Narasimha (Dhawan & Narasimha, 1958). However, this method is not compatible with existing CFD codes. Also, this model was designed to produce accurate streamwise intermittency behavior, but does not account for the variation of intermittency in the cross-stream direction.

Cho and Chung (Cho & Chung, 1992) developed a  $k - \varepsilon - \gamma$  turbulence model for free shear flows. Their turbulence model explicitly incorporates the intermittency effect into the conventional  $k - \varepsilon$  equations by introducing an extra transport equation for  $\gamma$ . Even though this model was not designed to reproduce flow transition, it did provide a realistic  $\gamma$  profile in the cross-stream direction.

Suzen and Huang (Suzen & Huang, 1999) improved upon the  $\gamma$  transport equation by combining the streamwise prediction properties of Steelant and Dick's model and the cross-stream prediction of Cho and Chung's model. This combined model can reproduce the streamwise intermittency distribution of Dhawan and Narasimha and can also produce a realistic intermittency variation in the cross-stream direction. The intermittency given by this transport equation is incorporated into the computations by multiplying the eddy viscosity from a turbulence model with the intermittency factor  $\gamma$ . The prediction capabilities of this model have been successfully validated against the T3- series experiments of Savill (Savill, 1993) and the low-pressure turbine experiments of Simon et al. (Simon, Qiu, & Yuan, 2000).

The model developed by Suzen and Huang showed that the concept of intermittency and the transport equation for intermittency could be used to reliably predict transition. The major drawback of the model was the integral that had to be solved for the momentum thickness Reynolds number. The  $\gamma$ - $Re_\theta$  transition model uses a transport equation for intermittency, like the above model, but it also uses a transport equation for the transition onset momentum thickness Reynolds number. This second transport equation is essential as it ties the empirical correlation to the onset criteria in the intermittency equation. The intermittency function is coupled with the SST turbulence model and is used to turn on the production term of the turbulent kinetic energy downstream of the transition point (Menter & Langtry, 2012). Since this model is based only on local variables, it can be used in unstructured parallel Navier-Stokes solvers.

The  $\gamma$ - $Re_\theta$  model is based on combining experimental correlations with locally formulated transport equations. The main quantity used to trigger the transition process is the vorticity Reynolds number, which is defined as

$$Re_v = \frac{\rho y^2}{\mu} \left| \frac{\partial u}{\partial y} \right| = \frac{\rho y^2}{\mu} S \quad (3.12)$$

where  $y$  is the distance to the nearest wall and  $S$  is the shear strain rate. This vorticity Reynolds number is a local property so it can easily be calculated at each grid point. A scaled profile of the vorticity Reynolds number for a Blasius boundary layer is shown below in Figure 3.1.

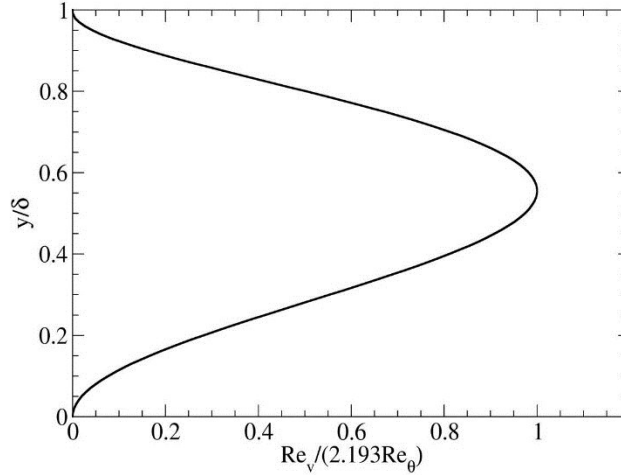


Figure 3.1:  $Re_v$  Profile for Blasius Boundary Layer (Menter & Langtry, 2012)

The scaling was chosen so that a maximum value of one is achieved inside the boundary layer. A maximum value of one was achieved by dividing the Blasius velocity profile by the corresponding momentum thickness Reynolds number and a constant of 2.193. This can then be related to transition correlations as follows:

$$Re_\theta = \frac{\max(Re_v)}{2.193} \quad (3.13)$$

This definition will serve as a local environment for correlation based transition models. It should be noted that there is a slight difference between the actual momentum thickness Reynolds number and the maximum vorticity Reynolds number, but difference is less than 10% and is usually not of great concern (Menter & Langtry, 2012).



### 3.2.2. $\gamma$ - $Re_\theta$ Model Equations

This section will discuss the transport equations for  $\gamma$  and  $Re_\theta$ , the correlations for each transport equation, and how the model is coupled to the SST turbulence model (Menter & Langtry, 2012).

The transport equation for the intermittency,  $\gamma$ , is as follows:

$$\frac{\partial(\rho\gamma)}{\partial t} + \frac{\partial(\rho U_j \gamma)}{\partial x_j} = P_\gamma - E_\gamma + \frac{\partial}{\partial x_j} \left[ \left( \mu + \frac{\mu_t}{\sigma_f} \right) \frac{\partial \gamma}{\partial x_j} \right] \quad (3.14)$$

where the transition source,  $P_\gamma$ , is defined as:

$$P_\gamma = F_{length} c_{a1} \rho S [\gamma F_{onset}]^{0.5} (1 - c_{e1} \gamma) \quad (3.15)$$

where  $S$  is the strain rate magnitude and  $F_{length}$  is an empirical correlation that controls the length of the transition region. The destruction/relaminarization source,  $E_\gamma$ , is defined as:

$$E_\gamma = c_{a2} \rho \Omega \gamma F_{turb} (c_{e2} \gamma - 1) \quad (3.16)$$

where  $\Omega$  is the vorticity magnitude. The onset of transition is controlled by the following functions:

$$Re_v = \frac{\rho y^2 S}{\mu} \quad (3.17)$$

$$F_{onset 1} = \frac{Re_v}{2.193 Re_{\theta c}} \quad (3.18)$$

$$F_{onset 2} = \min(\max(F_{onset 1}, F_{onset 1}^4), 2.0) \quad (3.19)$$

$$R_T = \frac{\rho k}{\mu \omega} \quad (3.20)$$

$$F_{onset 3} = \max\left(1 - \left(\frac{R_T}{2.5}\right)^3, 0\right) \quad (3.21)$$

$$F_{onset} = \max(F_{onset 2} - F_{onset 3}, 0) \quad (3.22)$$

where  $Re_{\theta c}$  is the critical Reynolds number where the intermittency first starts to increase in the laminar boundary layer (Menter & Langtry, 2012). Both the  $F_{length}$  and  $Re_{\theta c}$  correlations are functions of the transition Reynolds number,  $\widetilde{Re}_{\theta t}$ . Based on the Schubauer and Klebanof and T3- series test cases, a correlation for  $F_{length}$  based on  $\widetilde{Re}_{\theta t}$  and is as follows:

$F_{length}$

$$= \begin{cases} \left[ 398.198 * 10^{-1} + (-119.270 * 10^{-4})\widetilde{Re}_{\theta t} + (-132.567 * 10^{-6})\widetilde{Re}_{\theta t}^2 \right], & \widetilde{Re}_{\theta t} < 400 \\ \left[ 263.404 + (-123.939 * 10^{-2})\widetilde{Re}_{\theta t} + (119.548 * 10^{-5})\widetilde{Re}_{\theta t}^2 + (-101.695 * 10^{-8})\widetilde{Re}_{\theta t}^3 \right], & 400 \leq \widetilde{Re}_{\theta t} < 596 \\ \left[ 0.5 - (\widetilde{Re}_{\theta t} - 596.0) * (3.0 * 10^{-4}) \right], & 596 \leq \widetilde{Re}_{\theta t} < 1200 \\ [0.3188], & 1200 \leq \widetilde{Re}_{\theta t} \end{cases} \quad (3.23)$$

The correlation between  $Re_{\theta c}$  and  $\widetilde{Re}_{\theta t}$  is defined as:

$$F_{length} = \begin{cases} \left[ \widetilde{Re}_{\theta t} - \left( 396.035 * 10^{-2} + (-120.656 * 10^{-4})\widetilde{Re}_{\theta t} + (868.230 * 10^{-6})\widetilde{Re}_{\theta t}^2 \right) \right. \\ \quad \left. + (-696.506 * 10^{-9})\widetilde{Re}_{\theta t}^3 + (174.105 * 10^{-12})\widetilde{Re}_{\theta t}^4 \right], & \widetilde{Re}_{\theta t} \leq 1870 \\ \left[ \widetilde{Re}_{\theta t} - (593.11 + (\widetilde{Re}_{\theta t} - 1870.0) * 0.482) \right], & \widetilde{Re}_{\theta t} > 1870 \end{cases} \quad (3.24)$$

The constants for the intermittency equation are:

$$c_{a1} = 2.0; \quad c_{e1} = 1.0; \quad c_{a2} = 0.06; \quad c_{e2} = 50.0; \quad \sigma_f = 1.0; \quad (3.25)$$

For separation-induced transition, the following modification is made:

$$\gamma_{sep} = \min\left(s_1 \max\left[0, \left(\frac{Re_v}{3.235 Re_{\theta c}}\right) - 1\right] F_{reattach}, 2\right) F_{\theta t} \quad (3.26)$$

$$F_{reattach} = e^{-\left(\frac{R_T}{20}\right)^4} \quad (3.27)$$

$$\gamma_{eff} = \max(\gamma, \gamma_{sep}) \quad (3.28)$$

$$s_1 = 2 \quad (3.29)$$

The transport equation for the transition momentum thickness Reynolds number,  $\tilde{Re}_{\theta t}$ , is as follows:

$$\frac{\partial(\rho\tilde{Re}_{\theta t})}{\partial t} + \frac{\partial(\rho U_j \tilde{Re}_{\theta t})}{\partial x_j} = P_{\theta t} + \frac{\partial}{\partial x_j} \left[ \sigma_{\theta t} (\mu - \mu_t) \frac{\partial \tilde{Re}_{\theta t}}{\partial x_j} \right] \quad (3.30)$$

where the source term,  $P_{\theta t}$ , is defined as:

$$P_{\theta t} = c_{\theta t} \frac{\rho}{t} (Re_{\theta t} - \tilde{Re}_{\theta t}) (1.0 - F_{\theta t}) \quad (3.31)$$

$$t = \frac{500\mu}{\rho U^2} \quad (3.32)$$

where  $t$  is a time scale necessary for dimensional reasons. The blending function,  $F_{\theta t}$ , which is zero in the freestream and one in the boundary layer, is used to turn the source term on and off in the boundary layer and allow  $\tilde{Re}_{\theta t}$  to diffuse in from the freestream. The blending function is shown below:

$$F_{\theta t} = \min \left( \max \left( F_{wake} e^{-\left(\frac{y}{\delta}\right)^4}, 1.0 - \left( \frac{\gamma - 1/c_{e2}}{1.0 - 1/c_{e2}} \right)^2 \right), 1.0 \right) \quad (3.33)$$

where

$$\delta = \frac{50\Omega y}{U} * \delta_{BL}; \quad \delta_{BL} = \frac{15}{2} \theta_{BL}; \quad \theta_{BL} = \frac{\tilde{Re}_{\theta t} \mu}{\rho U} \quad (3.34)$$

$$F_{wake} = e^{-\left(\frac{Re_{\omega}}{1E+5}\right)^2}; \quad Re_{\omega} = \frac{\rho \omega y^2}{\mu} \quad (3.35)$$

The constants for the  $\tilde{R}e_{\theta t}$  equation are:

$$c_{\theta t} = 0.03; \quad \sigma_{\theta t} = 2.0; \quad (3.36)$$

The empirical correlation for the transition onset is based on the following two parameters:

$$\lambda_{\theta} = \frac{\rho \theta^2}{\mu} \frac{dU}{ds} \quad (3.37)$$

$$Tu = 100 \frac{\sqrt{2k/3}}{U} \quad (3.38)$$

As previously stated, the transition model interacts with the SST turbulence model. It does this in the following way:

$$\frac{\partial}{\partial t}(\rho k) + \frac{\partial}{\partial x_j}(\rho u_j k) = \tilde{P}_k - \tilde{D}_k + \frac{\partial}{\partial x_j} \left[ (\mu + \sigma_k \mu_t) \frac{\partial k}{\partial x_j} \right] \quad (3.39)$$

$$\tilde{P}_k = \gamma_{eff} P_k \quad (3.40)$$

$$\tilde{D}_k = \min[\max(\gamma_{eff}, 0.1), 1.0] D_k \quad (3.41)$$

The  $P_k$  and  $D_k$  terms are the original production and destruction terms in the SST turbulence model.

For numerical robustness and stability, the acceleration parameters, turbulence intensity, and empirical correlations should be limited as shown below:

$$-0.1 \leq \lambda_{\theta} \leq 0.1; \quad Tu \geq 0.027; \quad Re_{\theta t} \geq 20; \quad (3.42)$$

Also, in order to accurately capture the boundary layers, the grid must have a  $y^+$  value of approximately one at the first grid point off the wall. If the  $y^+$  spacing is too large, say greater than 5, the location of the onset of transition moves upstream.

### 3.2.3. $\gamma$ - $Re_{\theta}$ Model Validation

The  $\gamma$ - $Re_{\theta}$  transition model has been validated for multiple different test cases, including flat plate cases, turbomachinery cases, and unsteady cases. The following are some of the validation case.

- Flat plate experiments (Schubauer & Klebanoff, 1955)
- ERCOFTAC benchmarks (Savill, 1993)
- Low-pressure turbine experiments (Simon, Qiu, & Yuan, 2000)
- PAK-B blade experiments (Lake, King, & Rivir, 1999), (Huang, Corke, & Thomas, 2003), (Volino, 2002)
- Unsteady wake-blade interactions (Kaszeta, Simon, & Asphis, 2001), (Stieger, 2002)

The cases represent a wide variety of turbulence levels, Reynolds numbers, boundary conditions, and flow fields. These cases show good agreement between the experimental data and computational results, and validate the  $\gamma$ - $Re_{\theta}$  models' validity.

## **4. UND EXPERIMENTAL INVESTIGATION OF THE INFLUENCE OF TURBULENCE INTENSITY AND REYNOLDS NUMBER ON TURBINE FLOWS**

The following section details the incompressible and compressible flow experiments that look at the effect of Reynolds number and turbulence intensity on flow transition. These experiments collected heat transfer and aerodynamic loss data.

### **4.1. UND Incompressible Flow Experiments**

One important study investigating the effects of large scale turbulence in turbines due to advanced combustor design was conducted by (Ames, Wang, & Barbot, 2003) at University of North Dakota's large-scale low-speed cascade facility. The goal of these experiments was to investigate the turbulence characteristics of several new combustion configurations and how they affect vane heat transfer and aerodynamics. The vane and cascade details are shown below in Figure 4.1 & Figure 4.2. The cascade consists of 4 vanes, one of which is instrumented (vane 3).

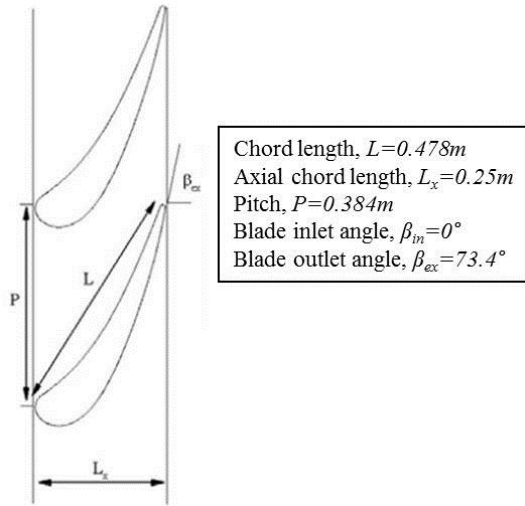


Figure 4.1: Incompressible Flow Vane Cascade Details (Ames, Argenziano, & Wang, 2004)

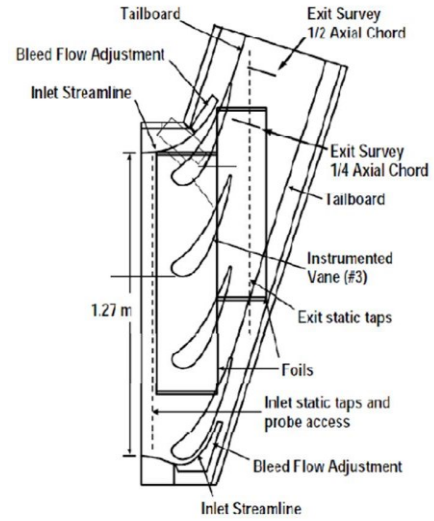


Figure 4.2: Layout of Cascade Test Section (Ames, Argenziano, & Wang, 2004)

These experiments used six different mock combustors that represent different combustion systems and their turbulence characteristics. Each mock combustor was run at three different exit Reynolds numbers, 500,000, 1,000,000, and 2,000,000 (based on true chord). The different mock combustors created different turbulence intensities that ranged from 0.6% to 14.33% (Ames, Argenziano, & Wang, 2004). Table 6.1 below shows the flow characteristics and turbulence parameters for each of the cases.

Table 4.1: Experiment Details and Turbulence Parameters (Ames, Argenziano, & Wang, 2004)

|                                      | Re        | FSTI   | U (m/s) | Lx (cm) | Lu (cm) | $T_{ke}(m^2/s^2)$ | $\epsilon (m^2/s^3)$ | $\Omega (1/s)$ | $q'' (W/m^2)$ |
|--------------------------------------|-----------|--------|---------|---------|---------|-------------------|----------------------|----------------|---------------|
| <b>Low Turbulence (LT)</b>           | 500,000   | 0.0069 | 4.96    | 8.12    | 127.0   | 1.757E-03         | 0.00005              | 0.316          | 226.8         |
|                                      | 1,000,000 | 0.0076 | 10.43   | 5.02    | 154.5   | 9.425E-03         | 0.00035              | 0.413          | 289.2         |
|                                      | 2,000,000 | 0.006  | 18.71   | 3.58    | 15.5    | 1.890E-02         | 0.0144               | 8.464          | 407.03        |
| <b>Catalytic Combustor (CC)</b>      | 500,000   | 0.0103 | 4.95    | 5.26    | 3.83    | 3.899E-03         | 0.0052               | 14.818         | 243.37        |
|                                      | 1,000,000 | 0.0153 | 9.46    | 0.62    | 5.15    | 3.142E-02         | 0.093                | 32.884         | 314.7         |
|                                      | 2,000,000 | 0.0102 | 19.63   | 0.89    | 1.75    | 6.014E-02         | 0.68                 | 125.642        | 440.87        |
| <b>Grid</b>                          | 500,000   | 0.0821 | 4.77    | 2.00    | 3.27    | 2.300E-01         | 2.7                  | 130.409        | 304.75        |
|                                      | 1,000,000 | 0.0861 | 10.19   | 2.04    | 3.35    | 1.155E+00         | 29.8                 | 286.766        | 460.1         |
|                                      | 2,000,000 | 0.0884 | 19.27   | 2.35    | 3.53    | 4.353E+00         | 206.8                | 527.897        | 743.3         |
| <b>Combustor with Spool (ACS)</b>    | 500,000   | 0.0915 | 5.11    | 5.08    | 9.03    | 3.279E-01         | 1.67                 | 56.585         | 291.99        |
|                                      | 1,000,000 | 0.095  | 9.74    | 4.61    | 8.81    | 1.284E+00         | 13.23                | 114.462        | 409.95        |
|                                      | 2,000,000 | 0.0928 | 18.19   | 4.44    | 9.49    | 4.274E+00         | 75.17                | 195.411        | 694.86        |
| <b>Aeroderivative Combustor (AC)</b> | 500,000   | 0.1313 | 5.24    | 3.68    | 7.24    | 7.100E-01         | 6.67                 | 104.376        | 258.35        |
|                                      | 1,000,000 | 0.1402 | 9.32    | 3.52    | 6.36    | 2.561E+00         | 51.5                 | 223.432        | 440.17        |
|                                      | 2,000,000 | 0.1339 | 18.39   | 3.58    | 7.35    | 9.095E+00         | 302                  | 368.934        | 799.4         |
| <b>Dry Low NO<sub>x</sub> (DLN)</b>  | 500,000   | 0.1342 | 5.17    | 4.57    | 8.78    | 7.221E-01         | 5.6                  | 86.172         | 279.77        |
|                                      | 1,000,000 | 0.1433 | 9.65    | 4.34    | 8.95    | 2.868E+00         | 43.73                | 169.394        | 420.2         |
|                                      | 2,000,000 | 0.1417 | 19.11   | 4.47    | 10.77   | 1.100E+01         | 274.5                | 277.298        | 771.2         |

## 4.2. UND Compressible Flow Experiments

The compressible flow investigation conducted at UND was designed to look at the aerodynamics losses and heat transfer of a first vane design for high altitude UAVs. This vane profile is a scaled down version of the profile in the incompressible flow experiments. The vane was scaled down to a true chord length of 12.1 cm. Data was taken at Reynolds numbers of 90K, 180K, 360K, and 720K, exit Mach numbers of 0.7, 0.8, 0.9, and low (0.8%) and high (9%) inlet turbulence levels. The cascade details are shown below in Figure 4.3. The results of these experiments will provide both upstream and downstream data, blade surface pressure data, and heat transfer data, which will be used to specify boundary conditions and for comparison with the numerical results.



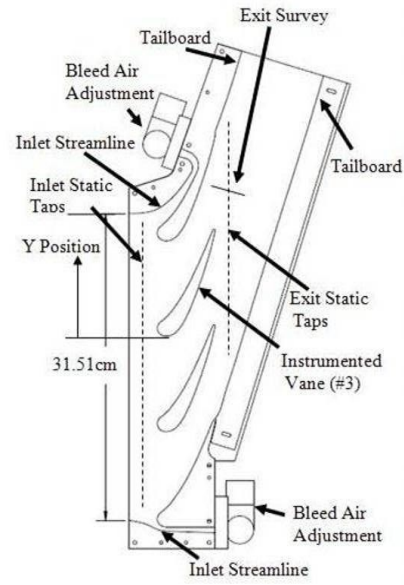


Figure 4.3: Compressible Flow Vane Cascade Details  
(Mihelish & Ames, 2013)

## **5. SIMULATIONS OF THE INFLUENCE OF TURBULENCE INTENSITY AND REYNOLDS NUMBER ON TURBINE FLOWS**

### **5.1. Incompressible Flow Simulations of (Kingery, Suzen, & Ames, 2010)**

These simulations were performed using the software package ANSYS-CFX. ANSYS-CFX is a three-dimensional, conservative, finite-element based control volume Navier-Stokes solver that uses an implicit pressure-based algorithm. All simulations were done using the SST turbulence model coupled with the  $\gamma$ - $Re_{\theta}$  transition model.

The mesh used for these simulations is shown below in Figure 5.1. This mesh contains ~400,000 nodes and has a thickness of one cell in the third direction. This one cell spacing is used to obtain the two dimensional solution. The spacing on the blade surface has a fine enough spacing to ensure a  $y^+$  value of less than one for all of the cases (Kingery, Suzen, & Ames, 2010).



Figure 5.1: Incompressible Mesh with Detail  
(Kingery, Suzen, & Ames, 2010)

The inlet boundary, located at the left boundary, condition was set with inlet velocities and turbulence parameters ( $k$  and  $\omega$ ) specified by the experiments, which were given above in Table 4.1. The outlet boundary, located at the right boundary, condition used an average static pressure condition specified from the experiments. A constant heat flux, from above table, was specified on the blade surface, as well as a no slip wall condition. The upper and lower faces were set as periodic boundaries in order to simulate a cascade. Symmetry boundary conditions were applied to the front and back of the domain. This was done to simulate the flowfield as a two dimensional flowfield (Kingery, Suzen, & Ames, 2010).

As stated above, all 18 simulations (6 turbulence intensities with 3 Reynolds numbers each) were run using the SST turbulence model and the  $\gamma$ - $Re_{\theta}$  transition model. The pressure

distribution over the blade surface is only compared to experimental data for the low turbulence (LT) case at  $Re=2,000,000$ , and can be seen below in Figure 5.2. The “zero” point for surface arc corresponds to the calculated stagnation point. The positive surface arc corresponds to the suction surface and the negative surface arc corresponds to the pressure surface.

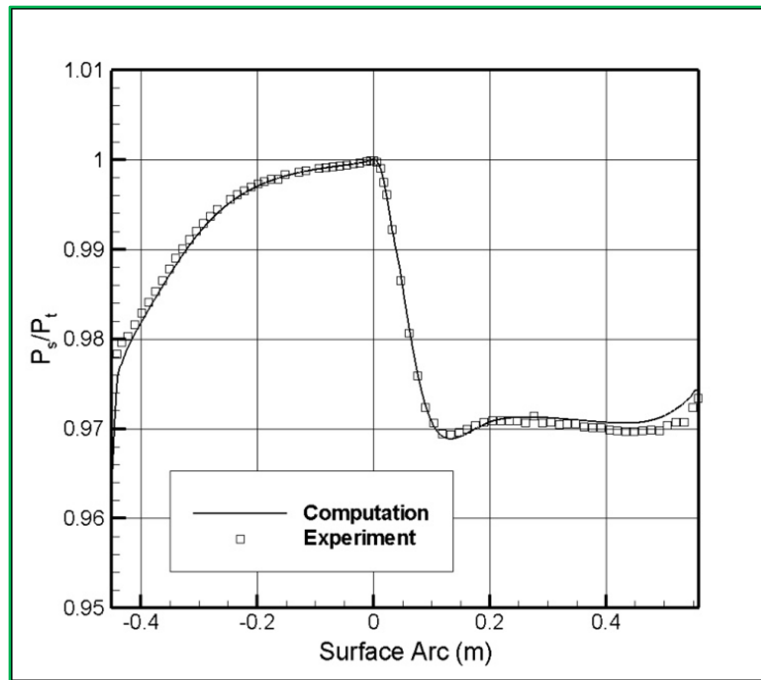


Figure 5.2: Computed vs Experimental Pressure Distribution (Kingery, Suzen, & Ames, 2010)

The computational pressure distribution and the experimental pressure distribution match very well, except for a slight overprediction near the trailing edge. This overprediction is thought to be due to a known issue with ANSYS-CFX when modeling two dimensional flows with a grid using one cell in the third direction (Kingery, Suzen, & Ames, 2010).

The wall heat transfer coefficient distributions for the LT and Catalytic Combustor (CC) cases are shown below in Figure 5.3 and Figure 5.4. Turbulence levels in these six simulations range from 0.6% to 1.53%, and represent the lower turbulence level cases.

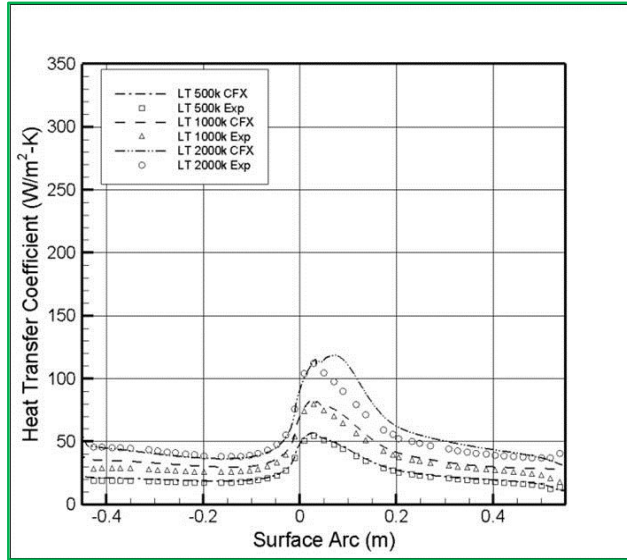


Figure 5.3: Low Turbulence (LC) Case Heat Transfer Coefficient (Kingery, Suzen, & Ames, 2010)

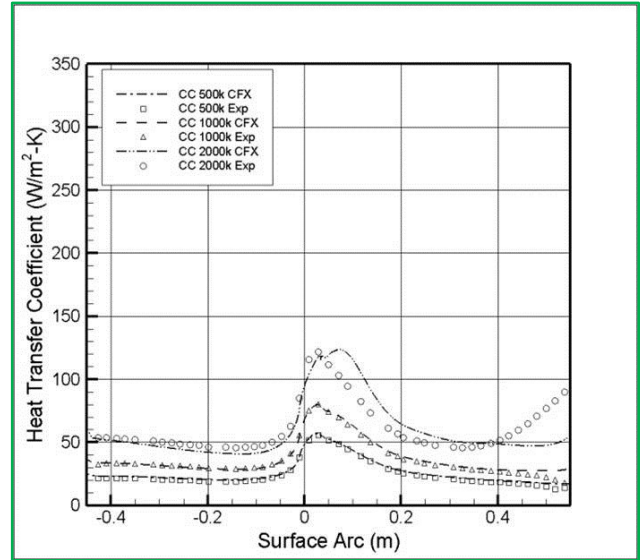


Figure 5.4: Catalytic Combustor (CC) Case Heat Transfer Coefficient (Kingery, Suzen, & Ames, 2010)

As can be seen from the above figures, the computations and experiments agree very well for the  $Re=500,000$  and  $Re=1,000,000$  cases. The  $Re=2,000,000$  cases show an overprediction on the suction side near the leading edge. For the CC  $Re=2,000,000$  case, the experimental data shows an increase in the heat transfer, which indicates onset of transition. This happens at around  $s \approx 0.35$ .

Figure 5.5 and Figure 5.6 below show the computational and experimental comparison of the heat transfer distributions for the Grid and the Aeroderivative Combustor with Spool (ACS) cases. These cases have FSTI levels that range from 8.21% to 9.5% and represent the medium turbulence level cases.

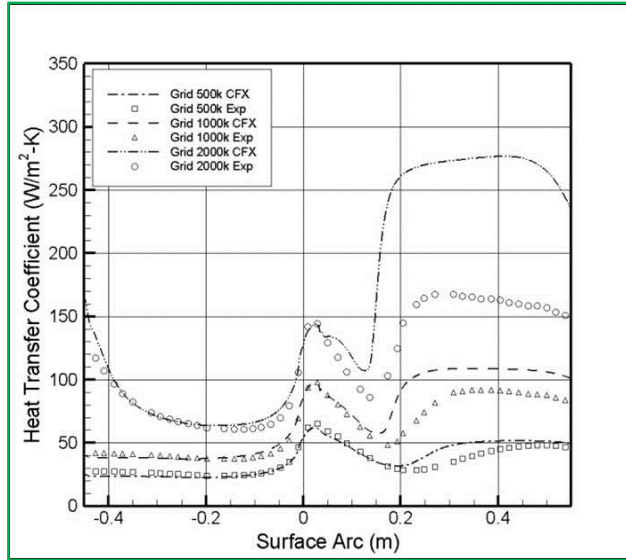


Figure 5.5: Grid Case Heat Transfer Coefficient (Kingery, Suzen, & Ames, 2010)

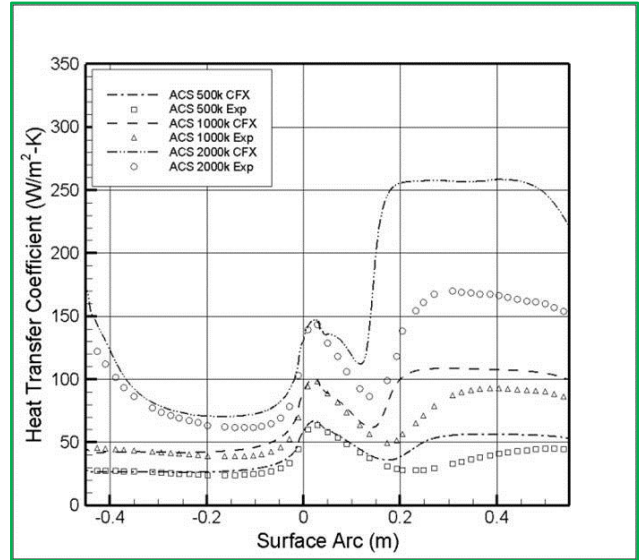


Figure 5.6: Aeroderivative Combustor with Spool (ACS) Case Heat Transfer Coefficient (Kingery, Suzen, & Ames, 2010)

For the Grid case, the computational and experimental results agree well for the  $Re=500,000$  and  $Re=1,000,000$  cases. The heat transfer is overpredicted in the  $Re=2,000,000$  case. For all three Grid cases, the onset of transition is predicted early and the length of transition is shorter than the experimental measurements. The same types of results are found for the ACS case. The heat transfer agreed well in the laminar section on the pressure surface, but as the Reynolds number increased, the overprediction on the suction side increased. Once again, the onset of transition was predicted earlier than the experiments and the transition length was shorter than measure in the experiments.

Figures show the computational and experimental comparison of the heat transfer distributions for the Aeroderivative Combustor (AC) and the Dry Low  $NO_x$  (DLN) cases. These cases have FSTI levels that range from 13.13% to 14.33% and are the highest turbulence level cases.

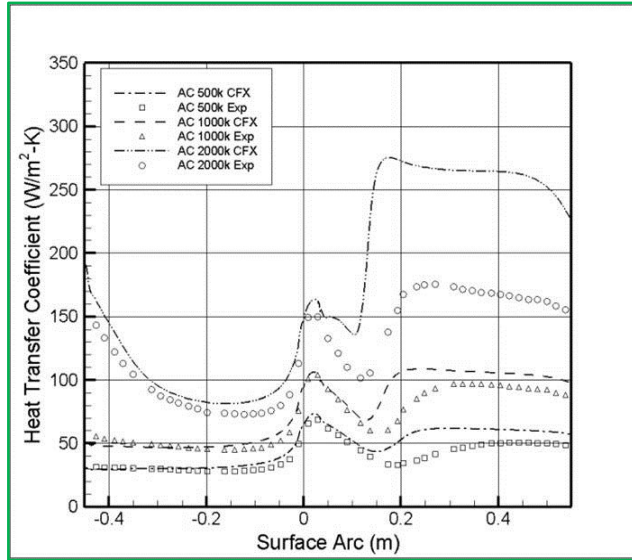


Figure 5.7: Aeroderivative Combustor (AC) Case Heat Transfer Coefficient (Kingery, Suzen, & Ames, 2010)

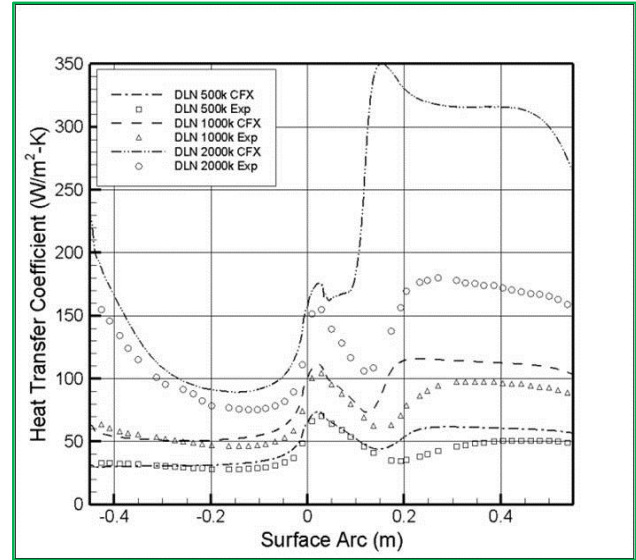


Figure 5.8: Dry Low NO<sub>x</sub> (DLN) Case Heat Transfer Coefficient (Kingery, Suzen, & Ames, 2010)

Both the AC and DLN cases showed the same trend in results as the medium intensity cases. They showed good agreement in the laminar section of the suction surface and overprediction on the suction surface, with a gross overprediction in the Re=2,000,000 cases. Once again, transition was predicted earlier and the transition length was shorter when compared to the experimental data

## 5.2. Compressible Flow Simulations

Simulations using a scaled down version of the vane profile of Kingery et al. (Kingery, Suzen, & Ames, 2010) were conducted incorporating compressible flow. The following sections will cover the meshing details, simulation setup, simulation convergence, and results for the compressible flow over a turbine vane.

### 5.2.1. Compressible Flow Vane Geometry

The geometry that was created for these simulations was a scaled down version of the profile Kingery et al (Kingery, Suzen, & Ames, 2010) used. This scaled down version had a true

chord length of 12.1 cm. A side view of the geometry can be seen below in Figure 5.9 and an isometric view can be seen below in Figure 5.10.



Figure 5.9: 2D Compressible Vane Geometry - Side View



Figure 5.10: 2D Compressible Vane Geometry - Isometric View

### 5.2.2. Compressible Flow Vane Mesh

The mesh employed for these simulations was created using the ICEM meshing software package. The meshing strategy employs inflation layers around the vane to capture the boundary layer and viscous effects. First layer spacing was refined small enough to ensure a maximum value of  $y^+ < 1$  around the vane. This meshing strategy resulted in a mesh with 280,372 nodes and 176,100 elements. This mesh can be seen below in Figure 5.11.





Figure 5.11: 2D Compressible Vane Mesh with Detail

### 5.2.3. Compressible Flow Vane Simulation Setup

This section will detail the procedure for the simulation setup and the parameters that were used in the setup. The boundary conditions for the simulations were taken from the experiments conducted at the University of North Dakota. The inlet boundary condition was specified using total pressure and total temperature conditions that correlated to the total pressure and total temperature conditions in the experiments. Turbulence parameters from the experimental data were also specified at the inlet. At the outlet, a static pressure condition and a static temperature condition were specified. The geometry was created with periodic top and bottom surfaces, so periodic boundary conditions were enforced at the top and bottom. The front and back faces were set as symmetrical boundaries as to avoid influences from a wall condition. Due to lack of heat transfer data at this time, these simulations were setup to look at the aerodynamic characteristics, and not the heat transfer.

#### 5.2.4. Compressible Flow Vane Simulation Convergence

As with the incompressible flow vane cases, these cases were also run in ANSYS-CFX. The simulations were using a high resolution advection scheme with double precision. Multiple time scale factors were tested within the solver to find the optimum scale that resulted in the best convergence. This time scale factor was found to be a 0.1. All simulations reached a RMS convergence of  $1e^{-6}$  for the momentum terms. The mass term reached a convergence level of  $\sim 1e^{-5}$  for all of the cases. The reason for the mass term not fully converging is due to the compressibility of the fluid in the simulations.

#### 5.2.5. Compressible Flow Vane Results

This section will detail the computational results of the two-dimensional compressible vane simulations. The figures below show the pressure distributions along the blade surface. The negative “S” distance represents the surface distance from the leading edge to the trailing edge on the pressure surface. The positive “S” represents the suction surface. This is shown in Figure 5.12.

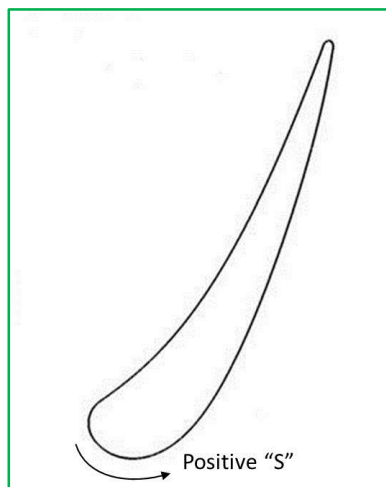


Figure 5.12: Surface Distance Diagram

The plots below show good agreement between the experiments and computations for the  $Ma=0.7$  case at every Reynolds number. As the Mach number increases ( $Ma=0.8$  and  $0.9$ ) there is still good agreement on the pressure side of the vane, but there becomes a large under-predictions of the surface pressure on the suction side of the vane. This under-prediction on the suction surface does change slightly with Reynolds number, which means that they under-prediction is somewhat dependent on Reynolds number. It is believed that the simulations being conducted with heat transfer will have a higher dependence on Reynolds number, like the results from Kingery, Suzen and Ames (Kingery, Suzen, & Ames, 2010). This under-prediction on the suction surface appears mostly independent of the Reynolds number since the lower Reynolds number cases show essentially the same under-prediction as the higher Reynolds number cases.

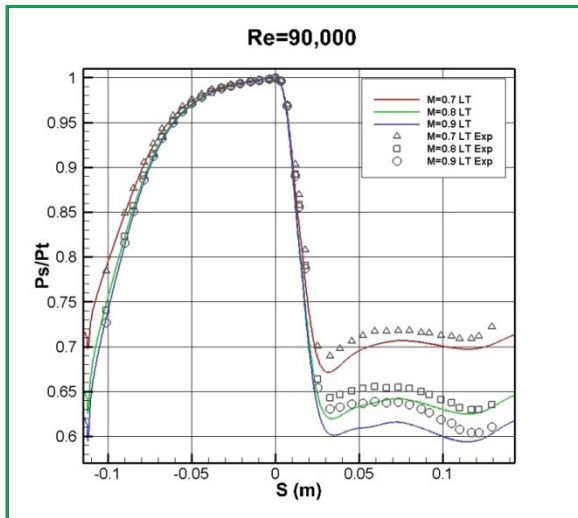


Figure 5.13:  $Re=90K$ , Low Turbulence Pressure Plot

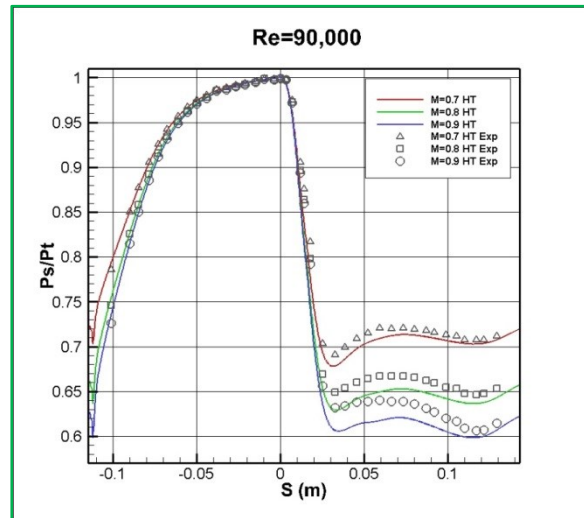


Figure 5.14:  $Re=90K$ , High Turbulence Pressure Plot

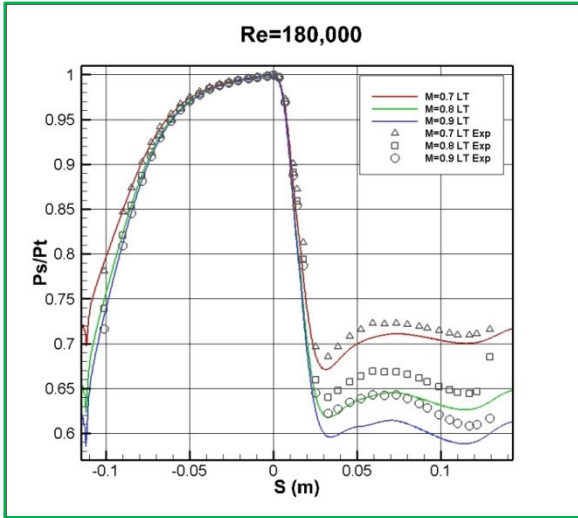


Figure 5.15: Re=180K, Low Turbulence Pressure Plot

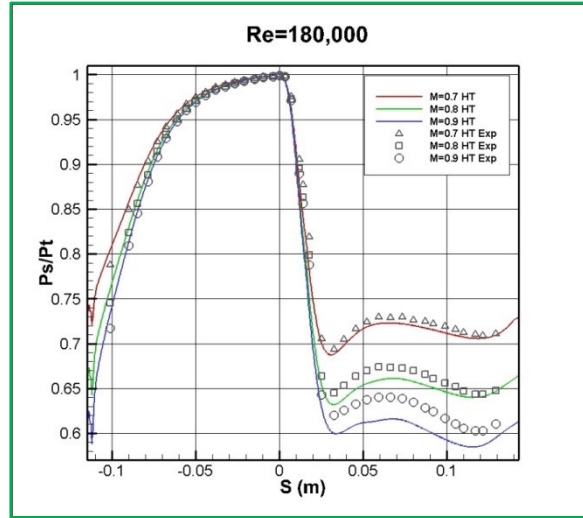


Figure 5.16: Re=180K, High Turbulence Pressure Plot

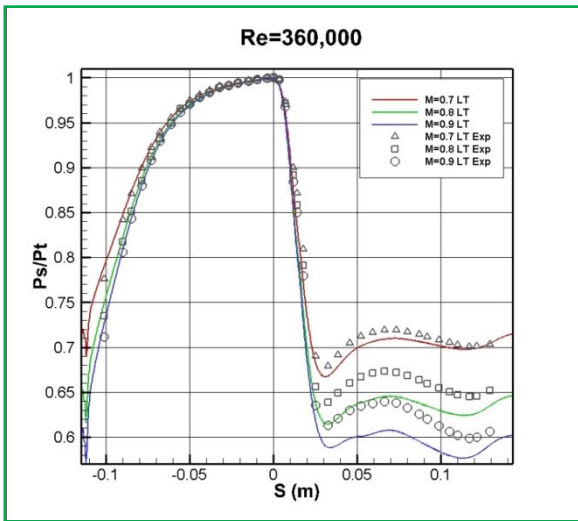


Figure 5.17: Re=360K, Low Turbulence Pressure Plot

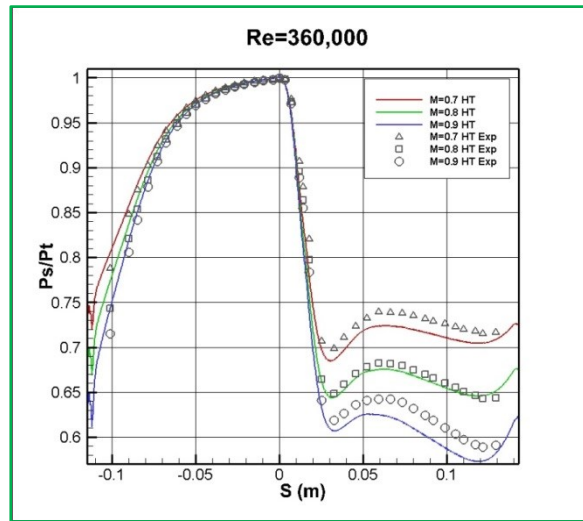


Figure 5.18: Re=360K, High Turbulence Pressure Plot

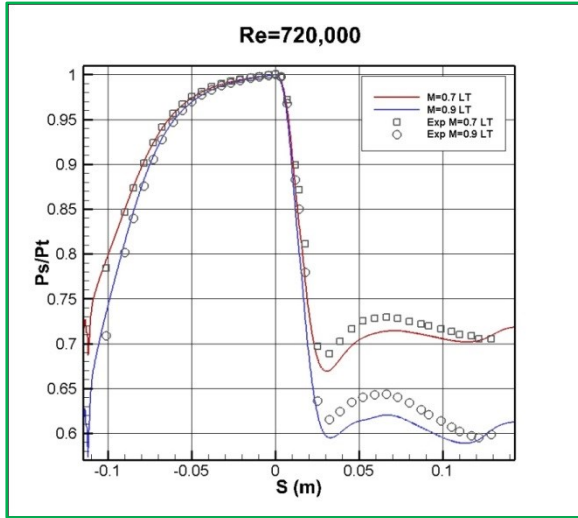


Figure 5.19: Re=720K, Low Turbulence Pressure Plot

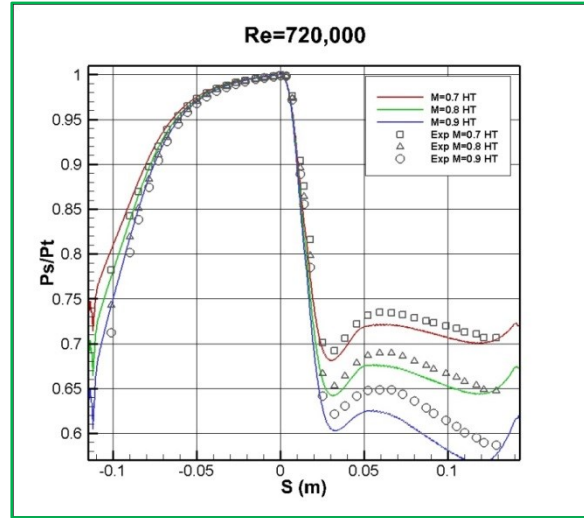


Figure 5.20: Re=720K, High Turbulence Pressure Plot

## 6. UND EXPERIMENTAL INVESTIGATION OF AN INCIDENT

### TOLERANT BLADE DESIGN

The following section details the experiments that are being conducted to look at the aerodynamics of an incident tolerant blade design. This blade geometry will be used in the NASA Large Civil Tilt-Rotor (LCTR) vehicle, which shown below in Figure 6.1.

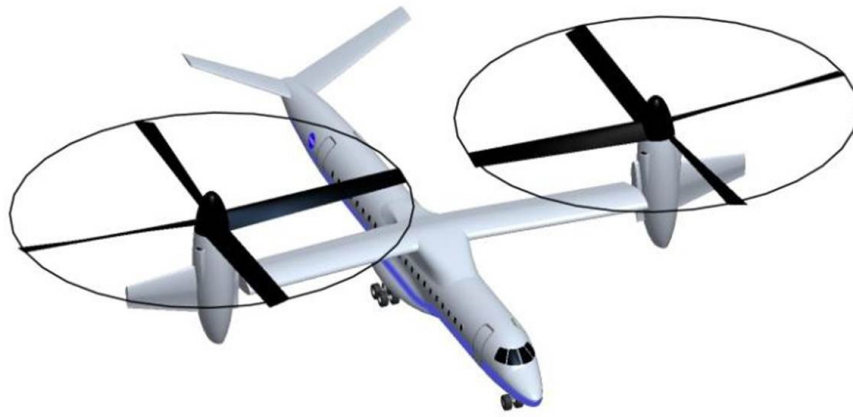


Figure 6.1: NASA LCTR Vehicle (Snyder, 2012)

The NASA LCTR uses an incident tolerant blade design in its' turbines due to the large incident angle changes that occur in the variable-speed power-turbine (VSPT). These large incident angle swings, ranging from  $40^\circ$  to  $60^\circ$ , occur due to the large changes in the work factor,  $(\Delta h_0/U^2)$ , and turbine speed between cruise and take off conditions. The work factor at cruise, where the turbine speed is approximately 54% of the maximum turbine speed, is about 3.5 times larger than the work factor at take-off, where the turbine is at its maximum speed (100%) (Welch, 2011).

The experimental work on this blade geometry is being conducted at the University of North Dakota in their large-scale low-speed cascade facility. Eight different incidence angles, or angles of attack, are being used in the experiments. These incidence angles range between  $+40^\circ$

to  $-17^\circ$ . The different incidence angles are achieved by changing the inlet ducting and bleed geometries on the test cascade. Experiments with multiple Reynolds numbers, ranging from 50,000 to 568,000 (based on true chord) were also run at each incidence angle. The SolidWorks models of the experimental cascade and nozzles are shown below in Figure 6.2.

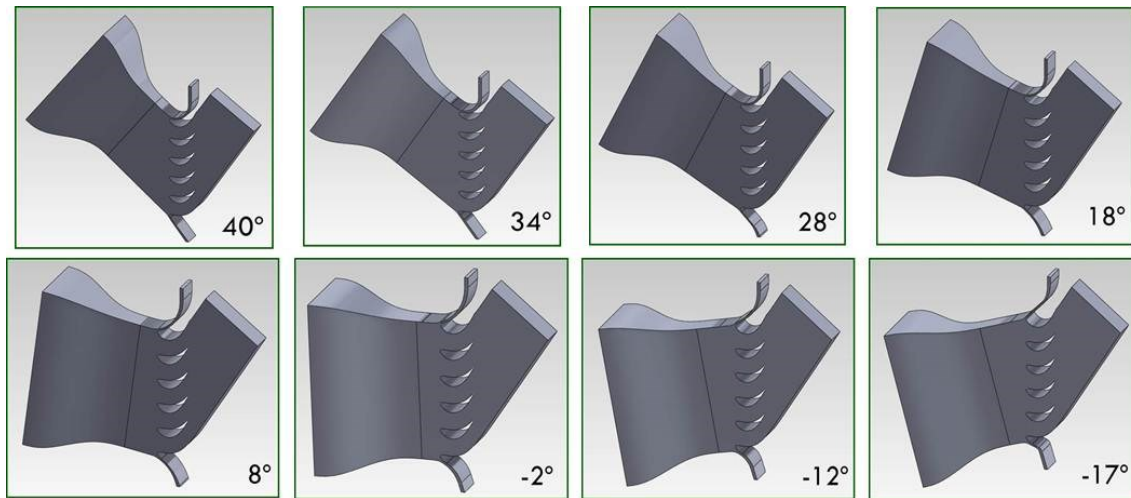


Figure 6.2: Experimental SolidWorks Models

The following figure shows the experimental surface pressures for blade 2 of the cascade. Table 4.1 below shows a tabulated list of the experimental data sets that will be run. Pressure data from 25% chord upstream and downstream, surface pressure data from blade 2, and heat transfer data will be collected in these experiments. The collected data will be used for applying boundary conditions and comparison with numerical results. The  $34^\circ$  incidence angle experimental data is shown below in Figure 6.3.

Table 6.1: Tabulated List of Simulations to be Conducted

| Incidence Angle | Turb. Level | Reynolds Numbers     |
|-----------------|-------------|----------------------|
| 40°             | LT          | 50K, 66K, 228K, 568K |
|                 | HT          | 50K, 66K, 228K, 568K |
| 34°             | LT          | 50K, 66K, 228K, 568K |
|                 | HT          | 50K, 66K, 228K, 568K |
| 28°             | LT          | 50K, 66K, 228K, 568K |
|                 | HT          | 50K, 66K, 228K, 568K |
| 18°             | LT          | 50K, 66K, 228K, 568K |
|                 | HT          | 50K, 66K, 228K, 568K |
| 8°              | LT          | 50K, 66K, 228K, 568K |
|                 | HT          | 50K, 66K, 228K, 568K |
| -2°             | LT          | 50K, 66K, 228K, 568K |
|                 | HT          | 50K, 66K, 228K, 568K |
| -12°            | LT          | 50K, 66K, 228K, 568K |
|                 | HT          | 50K, 66K, 228K, 568K |
| -17°            | LT          | 50K, 66K, 228K, 568K |
|                 | HT          | 50K, 66K, 228K, 568K |

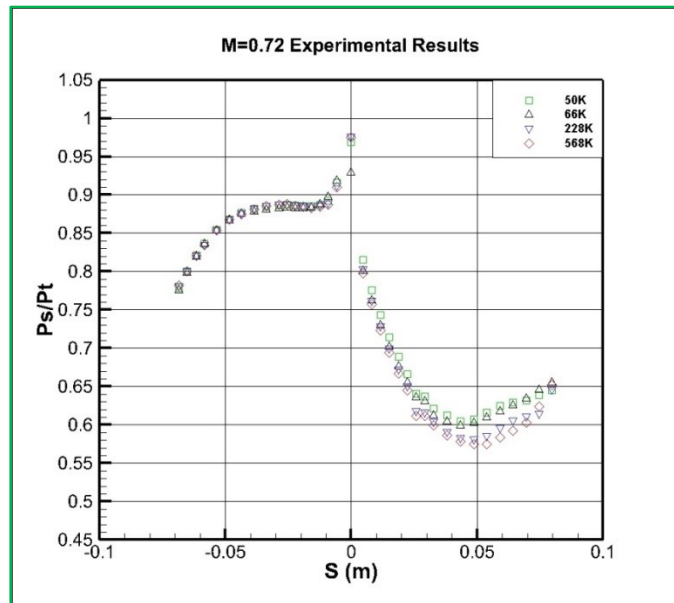


Figure 6.3: 34° Experimental Surface Pressure Data for Blade 2



## **7. SIMULATIONS OF AN INCIDENT TOLERANT BLADE DESIGN**

Two and three dimensional simulations of an incident tolerant blade design will be presented below. Due to the lack of experimental data, initial cases were run with conditions set in the expected range of the experimental data. Once experimental data was available, cases were run with boundary conditions defined by the experimental data. Currently, only data for the 34° low turbulence case is available. The preliminary and final 34° cases are presented below.

### **7.1. Two Dimensional Simulations**

Two dimensional simulations were conducted to find the “optimal” blade pressure distributions for each individual angle of attack, Reynolds number, and Mach number. The results from these two dimensional cases will also serve as a starting point for the three dimensional cases for providing several tuned boundary conditions.

#### **7.1.1. Two Dimensional Flowfield Generation**

A two dimensional flowfield was created by creating an upper streamline from the suction side of the blade, and then copying the streamline downwards by the pitch of the cascade. This created a two dimensional geometry that was periodic on the upper and lower boundaries. The MATLAB script that was created can be found in Appendix 6. Figure 7.1 below shows a picture of the geometry.



Figure 7.1: Side and Isometric View of the Two Dimensional Geometry

### **7.1.2. Two Dimensional Mesh Generation**

The mesh used for these two dimensional simulations was created in ICEM and can be seen below in Figure 7.2 and Figure 7.3. A first layer spacing that corresponds to a  $y^+ < 1$  was used to assure acceptable resolution in the boundary layer. A total of  $\sim 1,190,000$  elements and  $\sim 790,000$  nodes were in this mesh.

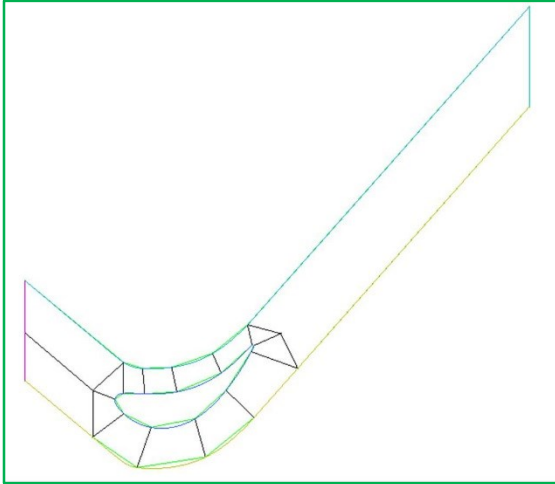


Figure 7.2: Two Dimensional Blocking Layout

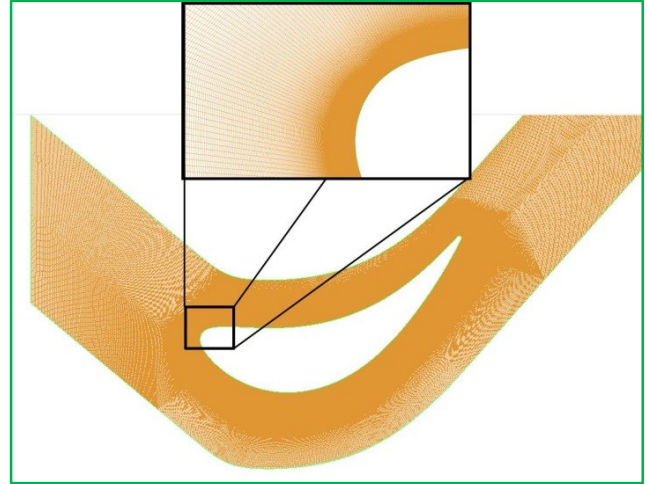


Figure 7.3: Two Dimensional Mesh with Detail

### 7.1.3. Preliminary Two Dimensional Simulation Parameters

These preliminary simulations were run before experimental data was available. They were used to perform mesh testing and make sure the simulations were ready when the experimental data was available. These preliminary simulation parameters were set to be in the range of the experimental parameters with a Reynolds number based on true chord of  $\sim 420,000$ . The boundary condition at the inlet was specified using a total pressure condition with a flow direction that corresponded to the specified angle of attack. The outlet was set using a static pressure condition. Using the periodicity of the top and bottom surfaces, these boundaries were set as periodic boundaries. The front and back surfaces were set as symmetrical boundaries as to make it a two dimensional case and eliminate any wall effects. The applied boundary conditions can be seen in the figure below.

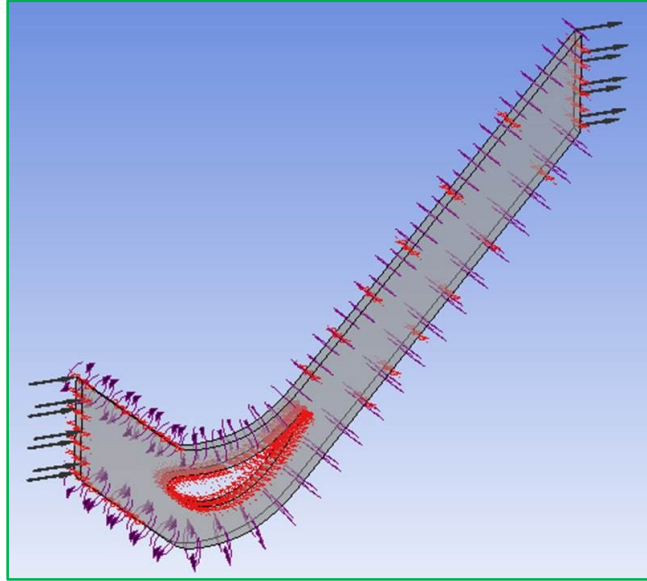


Figure 7.4: Two Dimensional Simulation Boundary Conditions

#### 7.1.4. Preliminary Two Dimensional Simulation Convergence

Simulations were run to either an error level of  $1e^{-6}$  (machine zero) or until the lowest possible convergence was achieved. The lowest error level ( $1e^{-6}$ ) was not achieved in all simulations due to fluid compressibility, and the large amount of separation and unsteadiness that occurred in the lower and negative angles of attack. Most of the cases converged smoothly, with the cases that employed the transition model have to run a higher number of iterations until convergence (~1500 iterations with transition model enabled, ~275 iterations with fully turbulent flow (transition model not enabled)). The only cases to not fully converge to an error level of  $1e^{-6}$  were the  $-12^\circ$  and  $-17^\circ$  cases with the transition model active. The two simulations not fully reaching complete convergence can be attributed to the highly chaotic flow and large separation regions on the blade surface.

#### 7.1.5. Preliminary Two Dimensional Simulation Results

Multiple aspects of the flow were looked at, some of the most important ones being the pressure distribution over the blade surface. As can be seen from the figures below, the higher

incidence angles show larger separation occurring on the suction surface of the blade, usually occurring approximately 0.075 meters of surface arc, while no separation occurs on the pressure surface. The positive “S” value corresponds to the surface distance along the suction surface. The “S=0” location corresponds to the location of the foremost pressure tap location in the experimental setup. This location and a diagram showing the “S” direction is shown in the figure below.

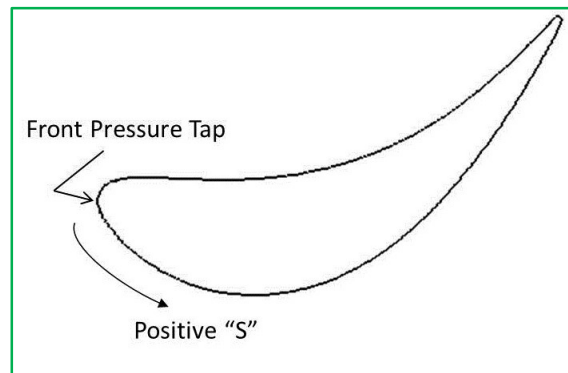


Figure 7.5: Surface Distance Diagram and Front Pressure Tap Location

The lower incidence angles show separation on the suction surface, and start to show separation on the suction surface. The  $-17^\circ$  cases show large separation on the pressure surface and highly chaotic flow on the suction surface. Figure 7.14 and Figure 7.15 show the pressure distributions for all incidence angles with and without the transition model active. The figures show the extreme changes in the surface pressures across the blade and the different areas of flow transition and separation.

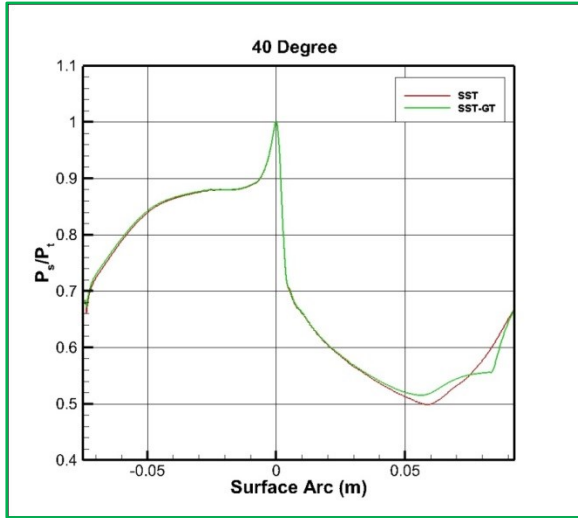


Figure 7.6: Preliminary 40° Two Dimensional Pressure Distribution

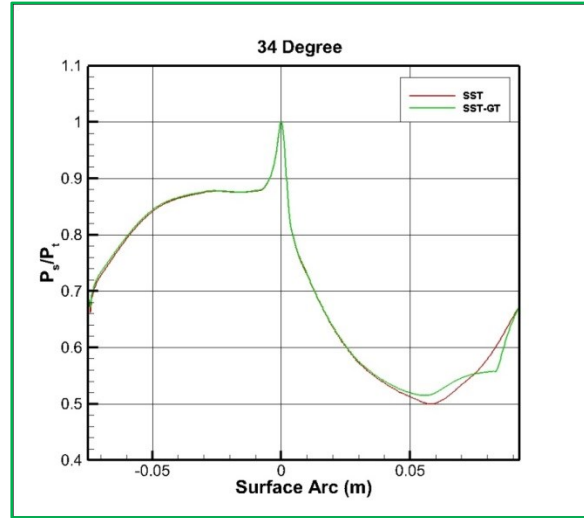


Figure 7.7: Preliminary 34° Two Dimensional Pressure Distribution

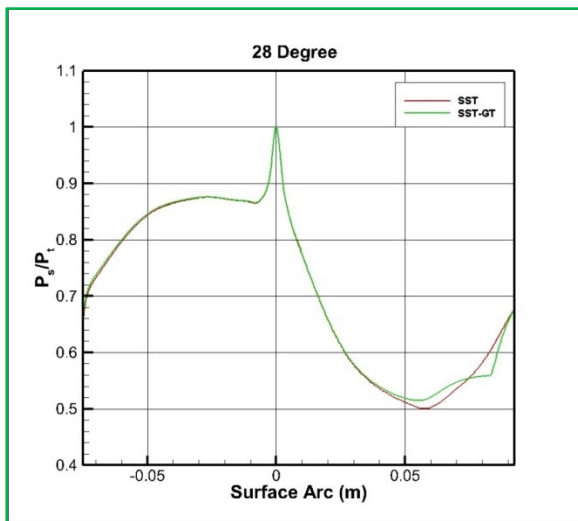


Figure 7.8: Preliminary 28° Two Dimensional Pressure Distribution

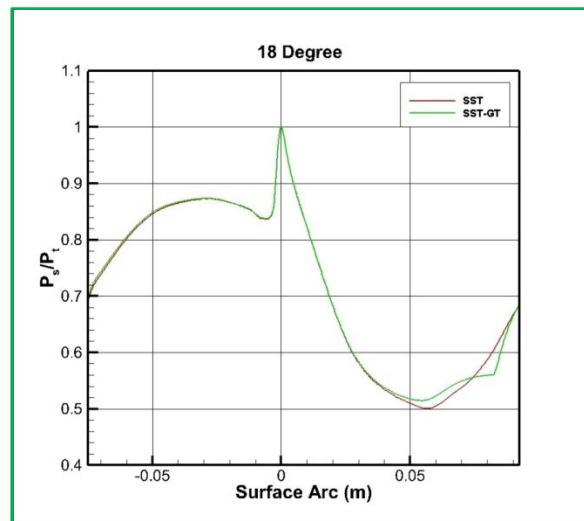


Figure 7.9: Preliminary 18° Two Dimensional Pressure Distribution

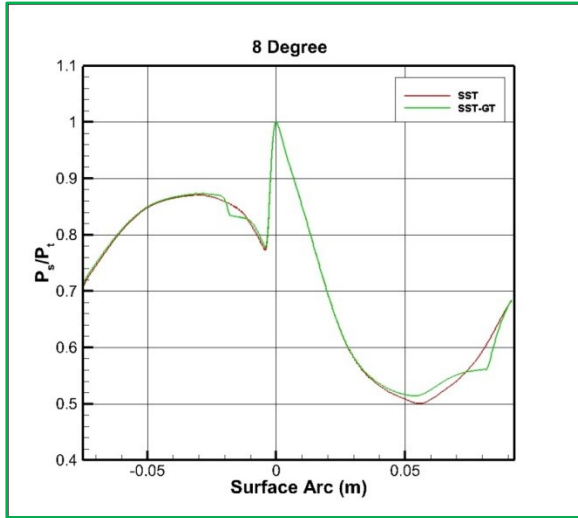


Figure 7.10: Preliminary 8° Two Dimensional Pressure Distribution

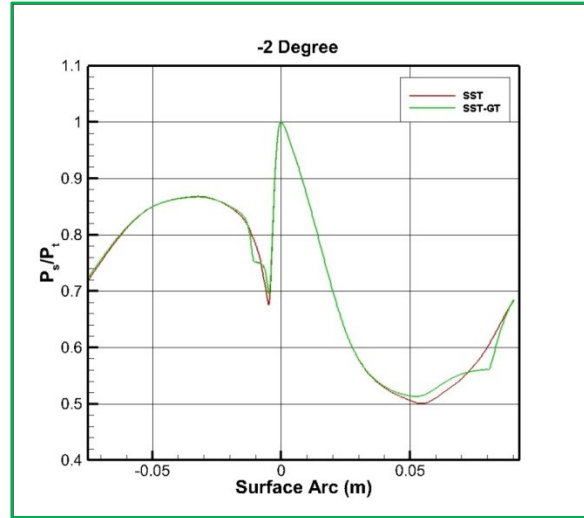


Figure 7.11: Preliminary -2° Two Dimensional Pressure Distribution

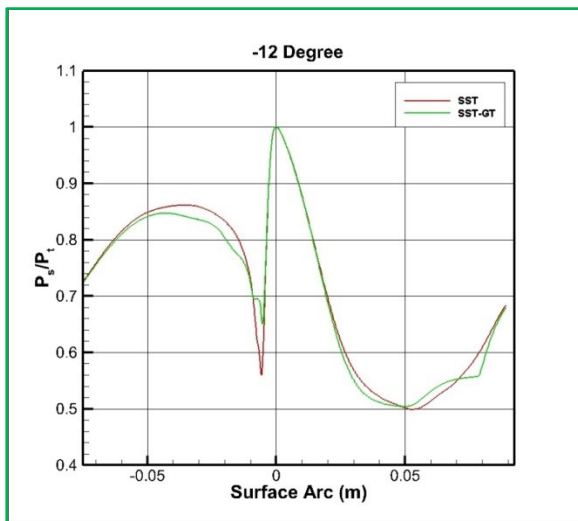


Figure 7.12: Preliminary -12° Two Dimensional Pressure Distribution

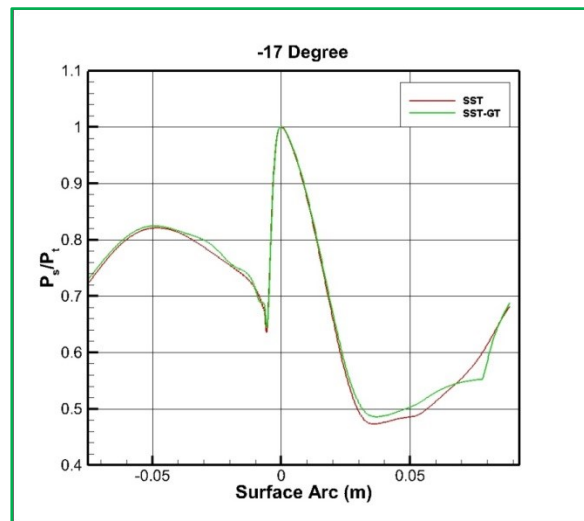


Figure 7.13: Preliminary -17° Two Dimensional Pressure Distribution

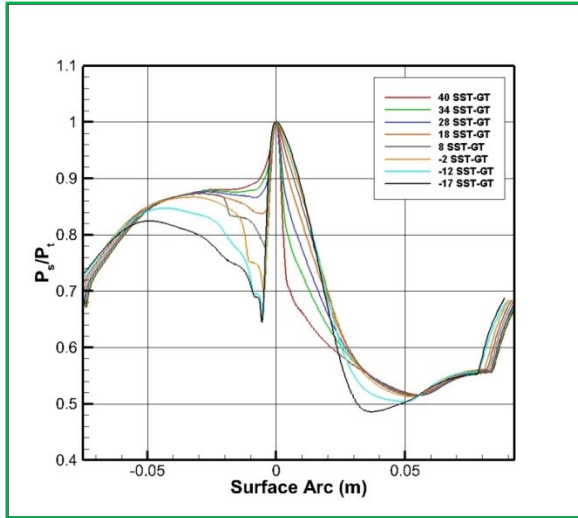


Figure 7.14: Pressure Distribution for All Incidence Angles with Transition Model Active

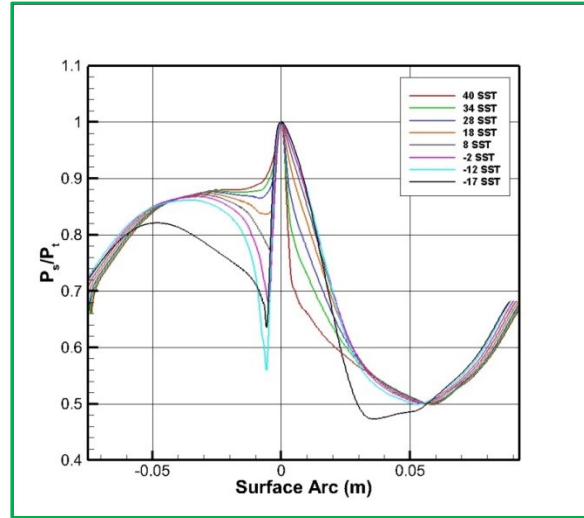


Figure 7.15: Pressure Distribution for All Incidence Angles without Transition Model Active

### 7.1.6. Two Dimensional Simulation of Incident Tolerant Blade Parameters

The input parameters for the final two dimensional simulations come from the experimental data collected at UND. This data was used to calculate boundary conditions for the inlet and outlet. The inlet boundary was specified using a total pressure and total temperature condition. The turbulence condition was defined at the inlet by the turbulent kinetic energy and dissipation rate. The outlet pressure was initially set to the domain pressure, then incrementally increased or decreased to match the experimental Mach number at a location 25% chord downstream. The top and bottom surfaces were set to be periodic with one another and the front and back faces were set to symmetrical boundaries as to negate wall effects. Figure 7.16 below shows the boundary conditions applied to the geometry.



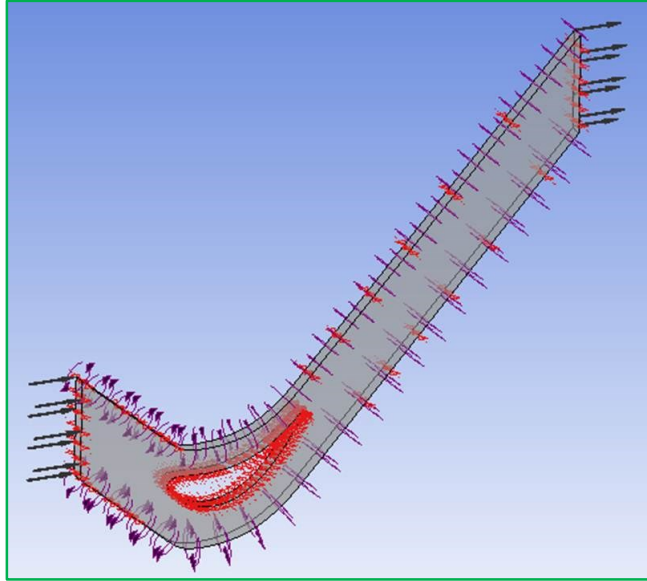


Figure 7.16: Final Two Dimensional Boundary Conditions

### 7.1.7. Two Dimensional Simulation of Incident Tolerant Blade Convergence

As with the incompressible and compressible flow vane simulation above, these simulations employed the ANSYS-CFX solver. All of the cases fully converged to a  $1e^{-6}$  level for all variables, except for the Re=50K case. The Re=50K case achieved a final convergence level of at least  $1e^{-5}$  for all variables.

### 7.1.8. Two Dimensional Simulation of Incident Tolerant Blade Results

This section will detail the final two dimensional results for the incident tolerant blade simulations with the  $\gamma$ - $Re_{\theta}$  transition model active. Figure 7.17 - Figure 7.20 shows the surface pressure distributions for the center plane of the blade. Overall, the pressures on the pressure surface agree very well with the experimental data, with just a slight overprediction of the pressure in the Re=50K case. In the Re=50K case no separation is seen in the experimental data, however, a large amount of transition and separation are seen on the suction surface. In the Re=66K case the pressure is under predicted and showed separation on the blade from S=0.6 to

$S=0.8$ . The experimental data showed a small amount of separation; much smaller than was seen in the computations. In the  $Re=228K$  case experimental and computational data agreed very well on the suction surface with the simulations showing a slightly larger length of separation. The  $Re=568K$  case showed no separation in the experimental data, but had slight separation near the trailing edge. The simulations show the separation moving further towards the trailing edge of the blade which is to be expected. The disagreement with the experimental data not showing separation is possibly due to a larger amount of free stream turbulence in the experiment than what was calculated.

Since the boundaries were periodic, the results could be duplicated and stacked to form a cascade so the results could be better visualized. Figure 7.21 - Figure 7.28 below show Mach contours of the stacked cascade and a zoomed in view around the blade. From these contours the large separation region in the lower Reynolds number cases and the small separation in the higher Reynolds number cases can be seen. Also note the much smaller wake region of the higher Reynolds number cases; this leads to a smaller loss coefficient downstream and lower aerodynamic losses.

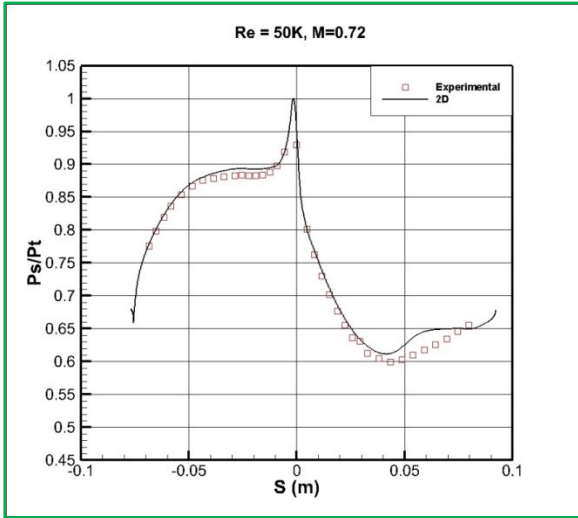


Figure 7.17: Re = 50K, Final Two Dimensional Surface Pressure Plot

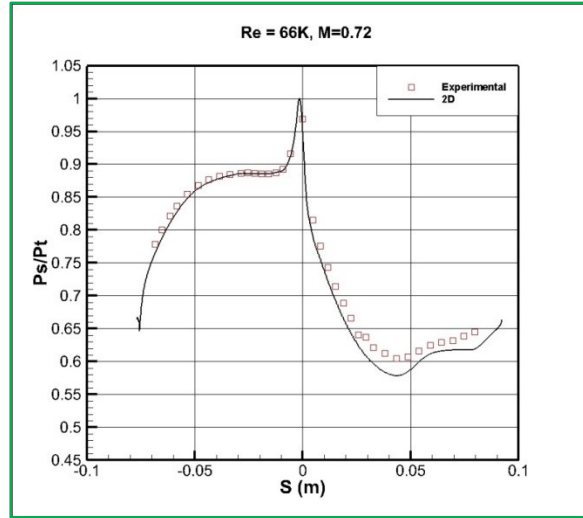


Figure 7.18: Re = 66K, Final Two Dimensional Surface Pressure Plot

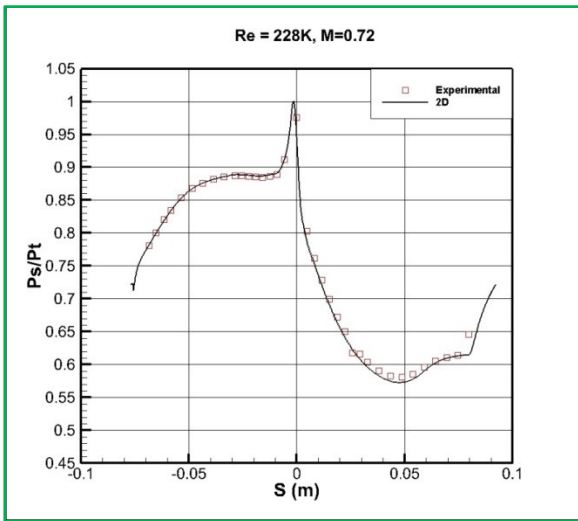


Figure 7.19: Re = 228K, Final Two Dimensional Surface Pressure Plot

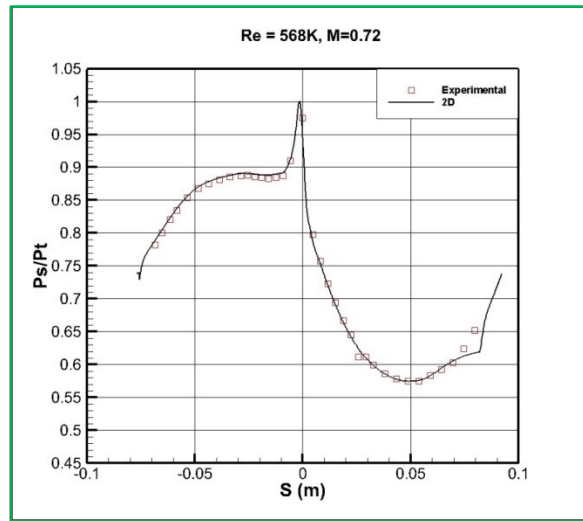


Figure 7.20: Re = 568K, Final Two Dimensional Surface Pressure Plot

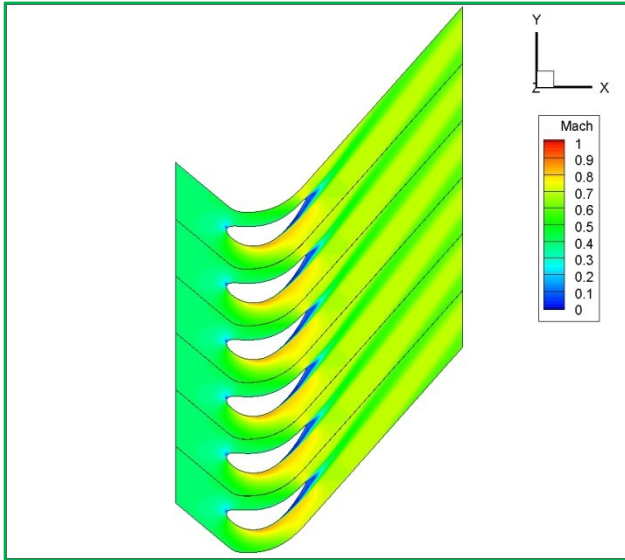


Figure 7.21: 34° Two Dimensional Re=50K Mach Contour for Simulated Cascade

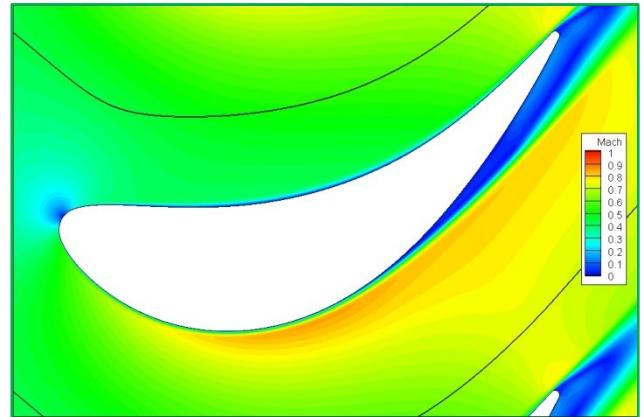


Figure 7.22: 34° Two Dimensional Re=50K Mach Contour Blade Zoom-in

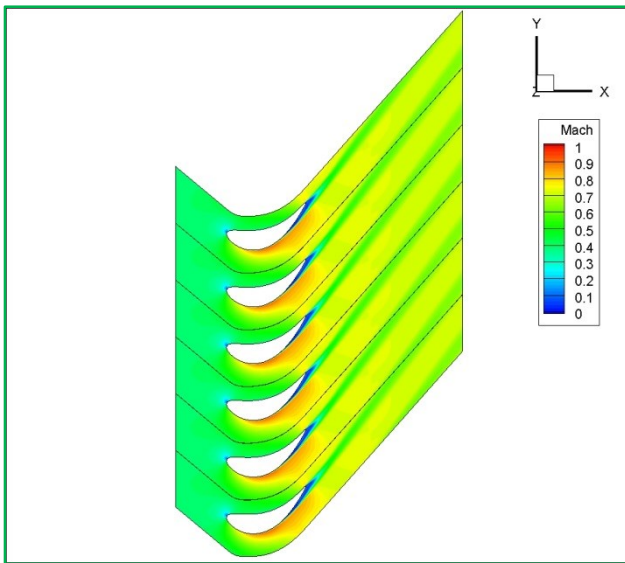


Figure 7.23: 34° Two Dimensional Re=66K Mach Contour for Simulated Cascade

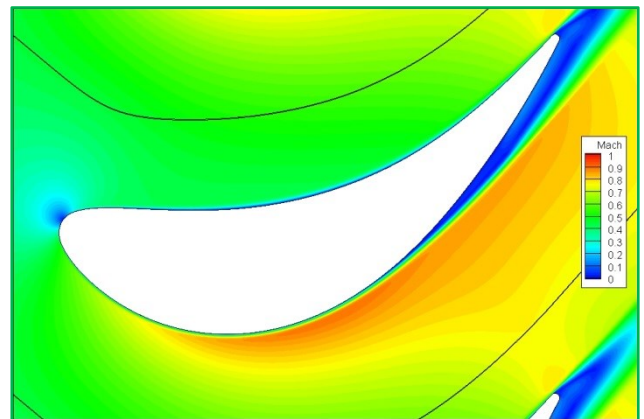


Figure 7.24: 34° Two Dimensional Re=66K Mach Contour Blade Zoom-in

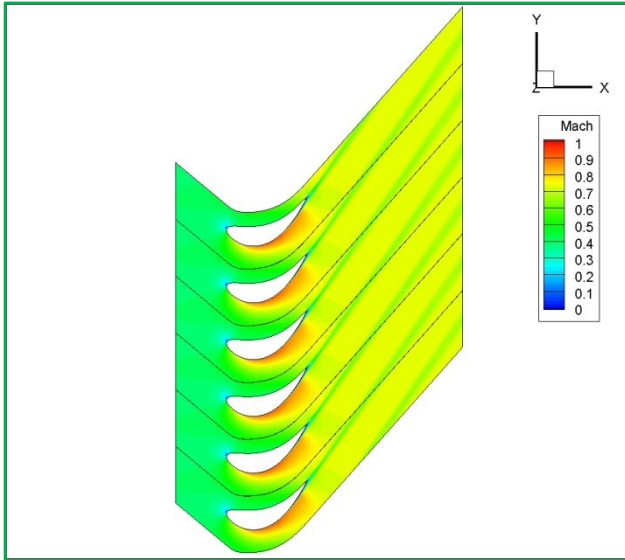


Figure 7.25: 34° Two Dimensional Re=228K Mach Contour for Simulated Cascade

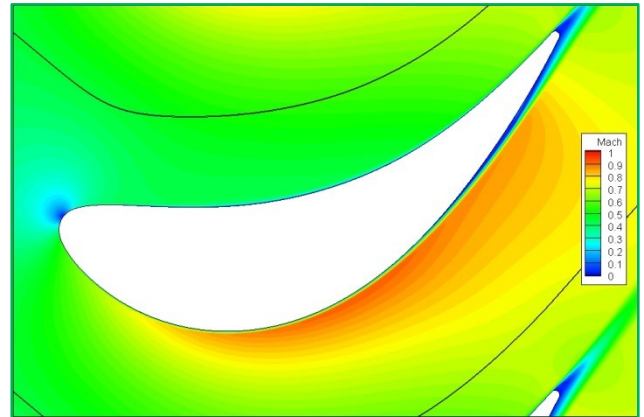


Figure 7.26: 34° Two Dimensional Re=228K Mach Contour Blade Zoom-in

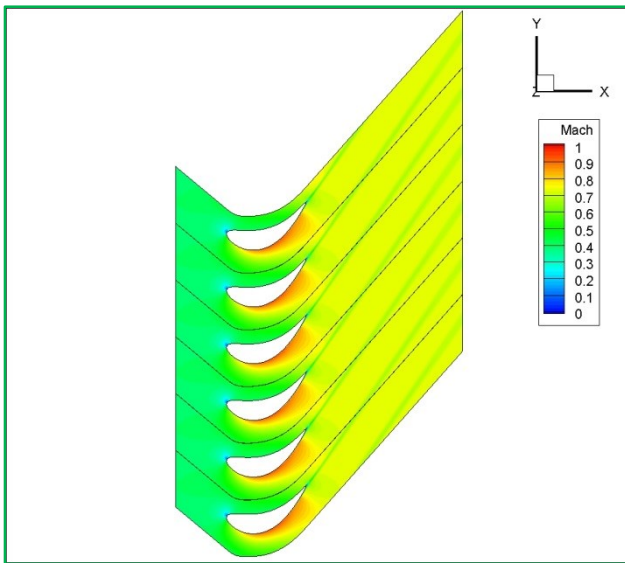


Figure 7.27: 34° Two Dimensional Re=568K Mach Contour for Simulated Cascade

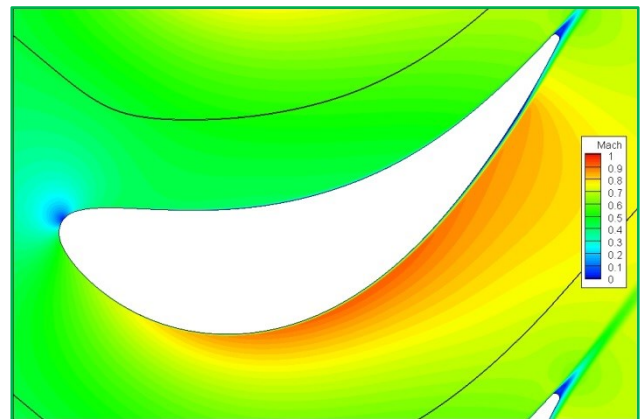


Figure 7.28: 34° Two Dimensional Re=568K Mach Contour Blade Zoom-in

## 7.2. Three Dimensional Simulations

The following sections will discuss the different aspects of the three dimensional compressible flow simulations, including the flowfield generation, mesh development, boundary conditions, convergence, and results.

### 7.2.1. Flowfield Generation

Eight different flowfields, corresponding to the eight different angles of attack, were generated for the three dimensional simulations. The flowfields were created from the original SolidWorks models of the experimental setup, and were shown previously in Figure 6.2. The flowfields consist of the inlet nozzle, the cascade, the pressure and suction bleeds, and the outlet ducting. The inlet nozzles and bleeds were different for each different incidence angle. The nozzle, cascade, and bleeds for the 40° case are shown below in Figure 7.29. A schematic of the entire 40° flowfield is shown below in Figure 7.30.

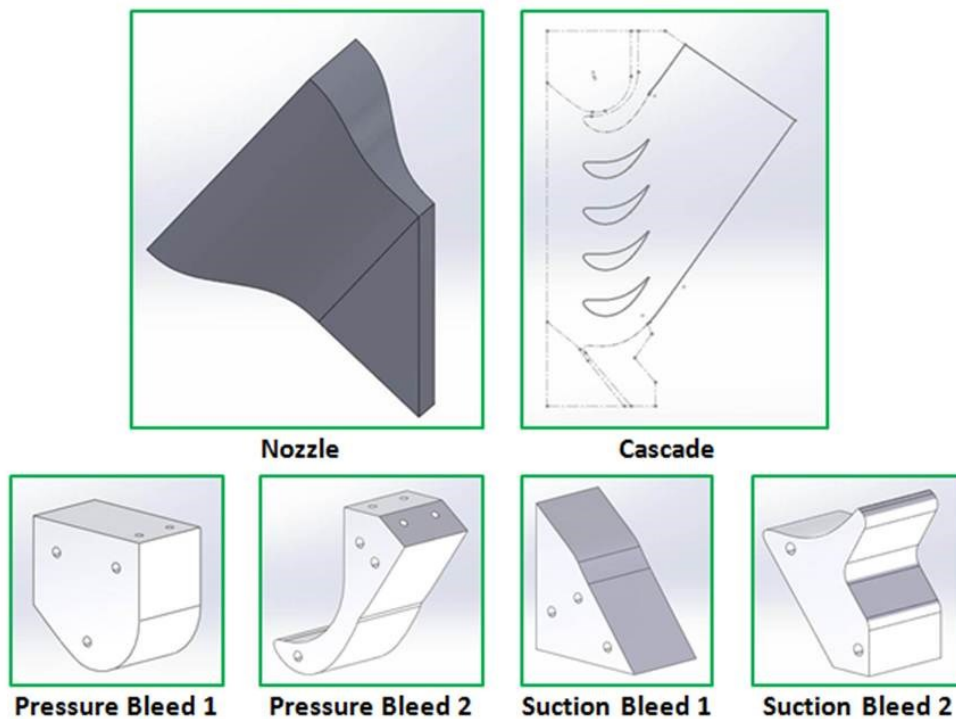


Figure 7.29: Geometry Components

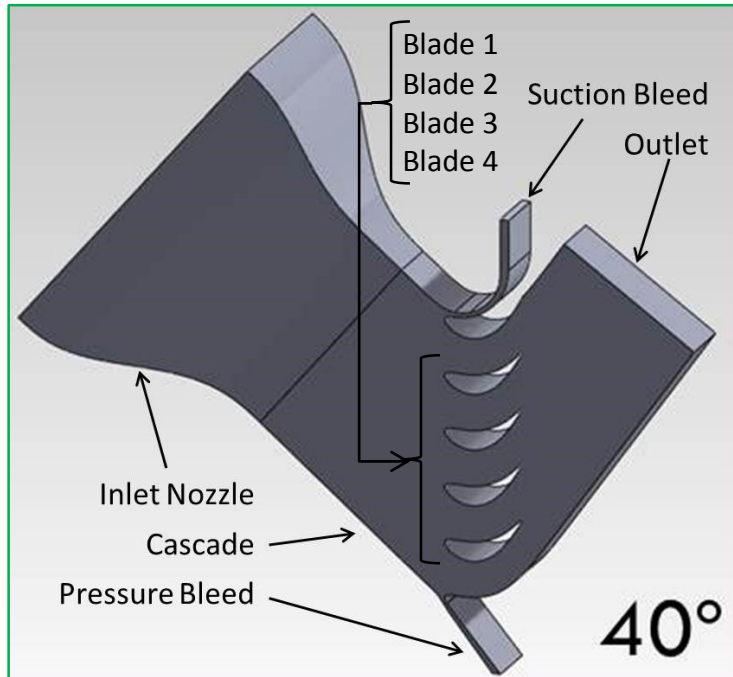


Figure 7.30: Flowfield Schematic

## 7.2.2. Mesh Generation

A mesh refinement study was first performed to find a mesh that resulted in a balance of reasonable computation time and accurate results. The following section details the mesh refinement study.

### 7.2.2.1. Mesh Refinement Study

The mesh refinement study was conducted on the 34° geometry. This angle of attack was chosen since it is the designed angle of attack for this particular blade. The final mesh to be used had to balance accurate results with a reasonable computation time. Three meshes were created using ANSYS CFX-Mesh. Different parts of the results, including convergence, blade pressure distributions, loss coefficients, and overall flowfield appearance, were used to compare the meshes and determine the best suitable mesh. Each mesh will now be discussed in detail.

### 7.2.2.1.1. Coarse Mesh

Coarse mesh was the coarsest of the three meshes used in the mesh refinement study. The mesh created a consistent mesh throughout the whole domain, with finer sections near the outer domain walls. The blades in the cascade had the highest area of mesh density in the domain. This was accomplished by a combination of small wall spacing and inflation layers. All four blades in the cascade had the same meshing parameters, which included a  $y^+ \sim 1$ . The mesh consisted of  $\sim 4,839,000$  nodes and can be seen below in Figure 7.31.

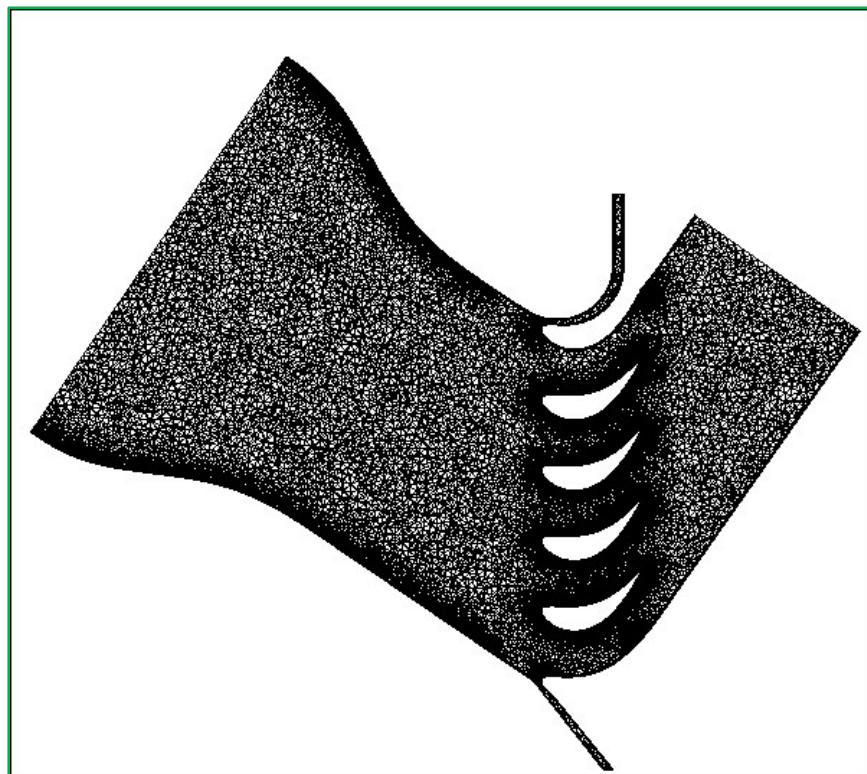


Figure 7.31: Coarse Mesh Used in Mesh Refinement Study

### 7.2.2.1.2. Intermediate Mesh

Intermediate mesh similar sizing parameters as coarse mesh in the freestream, but differed in the area around the blades. The mesh around blade two was refined to a higher mesh density on the blade surface, while the mesh around the other three blades was similar to that in



coarse mesh. This was done to create a higher resolution area around the second blade, since this blade will be the instrumented blade in the experiments. This created a mesh with  $\sim 5,586,000$  nodes. Intermediate mesh can be seen below in Figure 7.32.

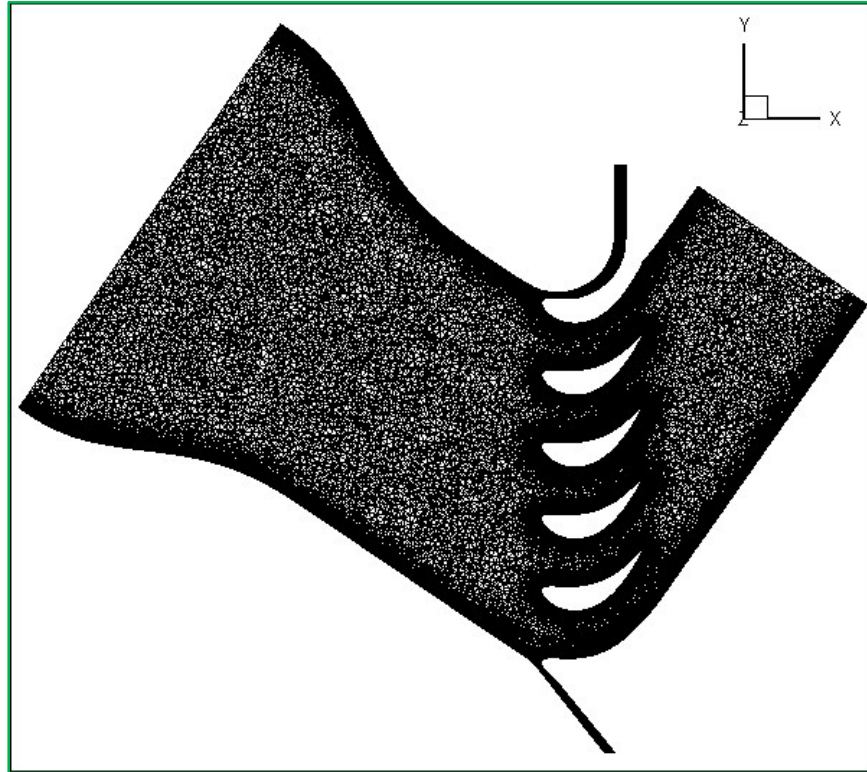


Figure 7.32: Intermediate Mesh Used in Mesh Refinement Study

#### 7.2.2.1.3. Fine Mesh

The fine mesh had the highest node count of all three meshes. Similar sizing parameters to those in the previous meshes were used in the free stream since high resolution in the freestream flow upstream of the cascade was not needed. A body of influence was used to increase the mesh density in the areas between and around the blades in the cascade. A small wall spacing near the blades coupled with small inflation layers led to a very high mesh density throughout the cascade section of the domain. The high mesh density would have a higher resolution in the blade passages, which is crucial when looking at the losses and flow structure in

the passages. Figure 7.33 below shows the body of influence and the areas that it affects in the flowfield. The fine mesh contained ~11,971,000 nodes and can be seen below in Figure 7.34.

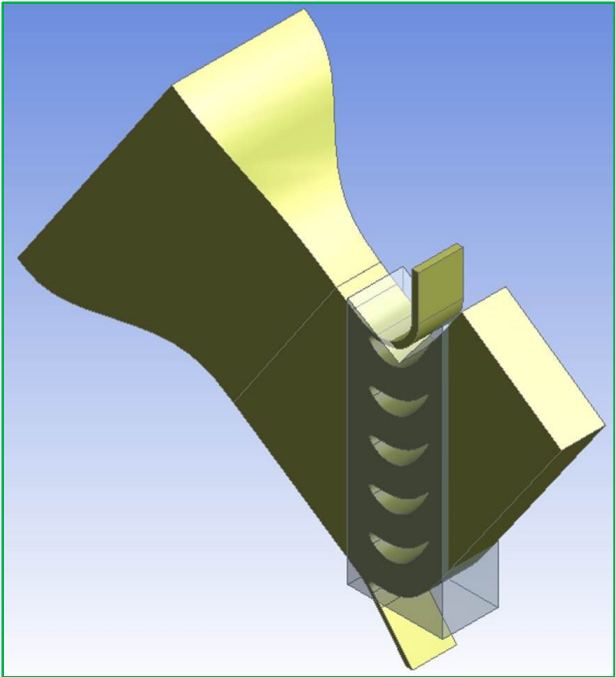


Figure 7.33: Fine Mesh Flowfield with Body of Influence

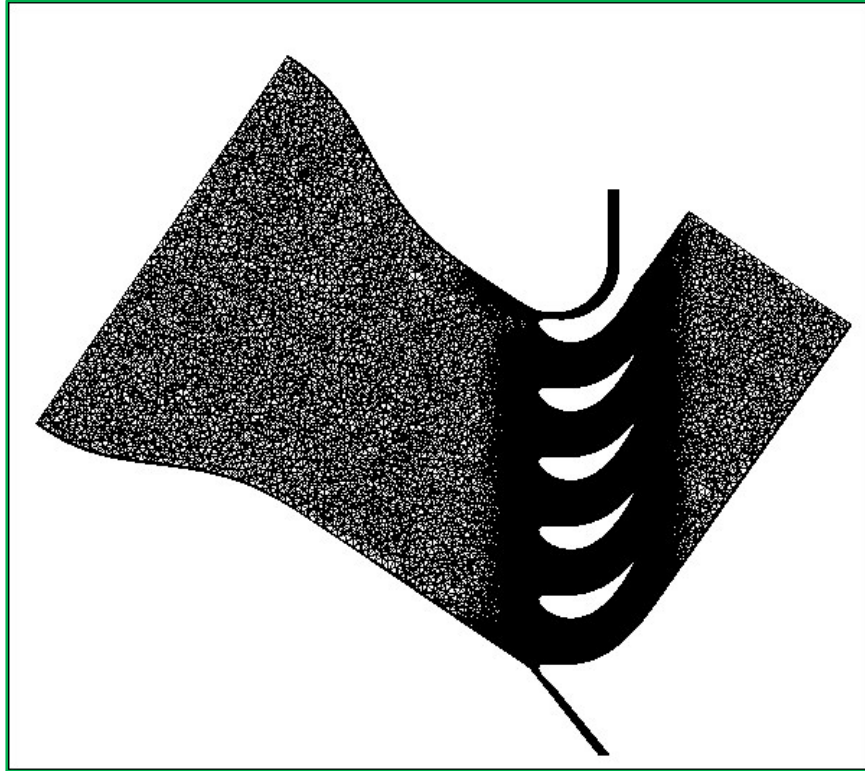


Figure 7.34: Fine Mesh Used in Mesh Refinement Study

#### 7.2.2.1.4. Mesh Refinement Simulation Parameters

A total of six different simulations were conducted with the three meshes shown above. Cases with and without the  $\gamma$ - $Re_{\theta}$  transition model activated were run for each mesh. The cases were setup using the SST model as the turbulence model. The boundary conditions applied resulted in a Reynolds number based on true chord of  $\sim 420,000$ . This Reynolds number proved satisfactory since it was within the range of the experiments at UND.

#### 7.2.2.1.5. Mesh Refinement Simulation Convergence

These simulations also employed the ANSYS-CFX solver with a target RMS convergence level for all variables of  $1e^{-6}$ . The coarse mesh converged fully and smoothly with and without the transition model enabled, with the fully turbulent simulation converging in  $\sim 245$  iterations, while the simulation with the transition model active converged in  $\sim 1500$  iterations. Neither of the simulations using the intermediate mesh fully converged. This is due to the higher

mesh density on blade 2 and the separation that is found on the blade surface. With the fine mesh, the fully turbulent simulation fully converged after ~210 iterations while the simulation with the transition model active showed converged to a level below  $1e^{-4}$ . This convergence can be improved by adjusting the time scale factor and other parameters in the solver.

#### **7.2.2.1.6. Mesh Refinement Results**

Figure 7.36, Figure 7.37, and Figure 7.38 below show the pressure distributions on the blade surfaces for the fully turbulent simulations. Figure 7.39, Figure 7.40, and Figure 7.41 show the surface pressure distributions for all three meshes with the transition model active. Simulations were run with and without the transition model to eliminate the possibility that the transition model was changing the results between the meshes. Looking at the surface pressure distributions it can be seen that the meshes gave similar results on the pressure surface of the blades. Where the differences can start be noticed is right after the stagnation point on the suction surface, and toward the trailing edge on the suction surface. As noted in the previous section, the coarse mesh had the smoothest convergence. The coarse mesh also produced results which had good agreement between the blades for the separation region near the trailing edge, while the intermediate mesh had discrepancies between the blades. The fine mesh also produced results which had good agreement between the blades, even though the convergence was not optimal.

The last three figures show the loss contours 25% chord upstream and downstream, mid-chord, and at the trailing edge. Figure 7.35 below shows the locations of the loss coefficient planes. Meshes 1 and 2 produced good results, but as can be seen in the loss contours (especially at 25% chord downstream), there is some discrepancy from passage to passage. The fine mesh

produced a more uniform flowfield. This uniformity is due the higher refinement level and mesh density in the passages of the fine mesh.

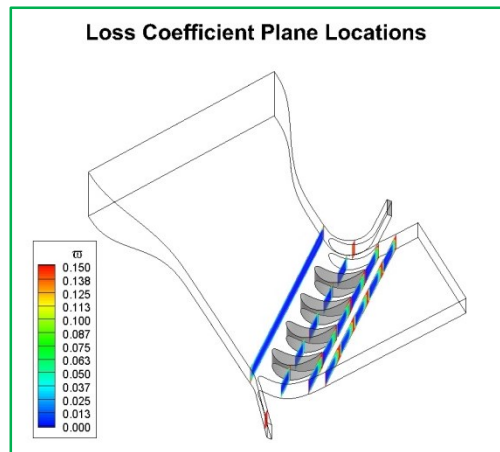


Figure 7.35: Loss Coefficient Plane Locations

This mesh refinement study has shown minimal changes in the flowfield and pressure seen on the blade surfaces; meaning that an optimal mesh with high resolution in the passage areas has been generated and a grid independent solution has been found.

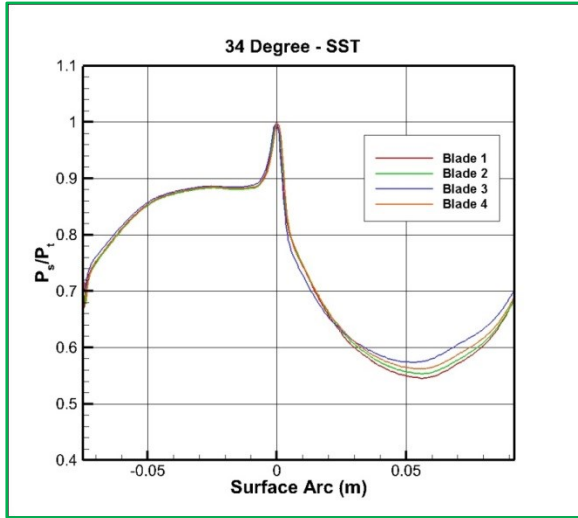


Figure 7.36: Fully Turbulent Surface Pressures Using Coarse Mesh

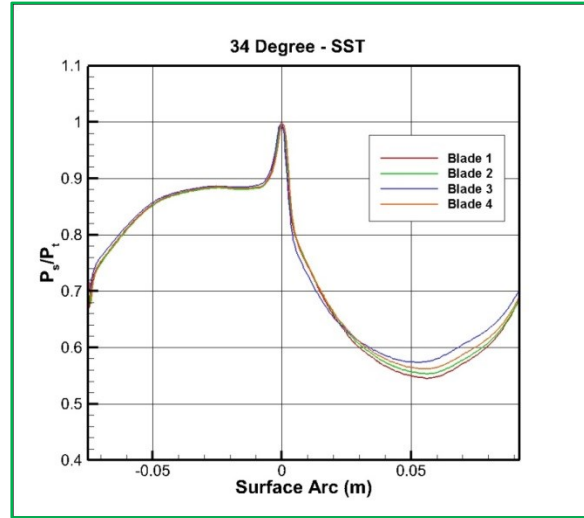


Figure 7.37: Fully Turbulent Surface Pressures Using Intermediate Mesh

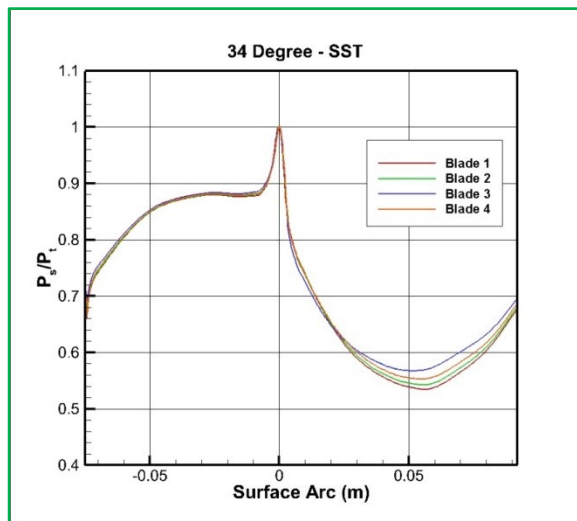


Figure 7.38: Fully Turbulent Surface Pressures Using Fine Mesh

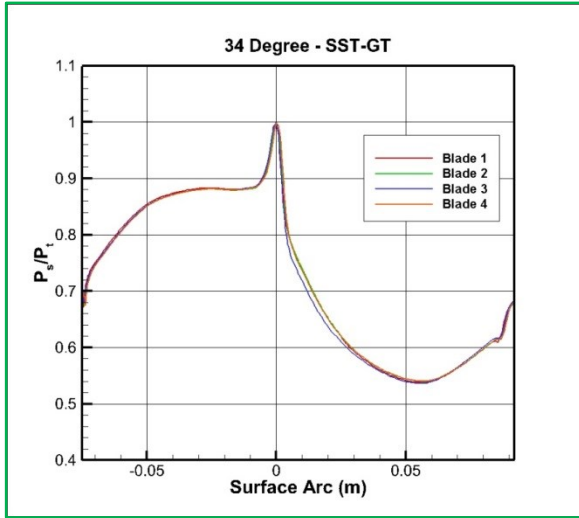


Figure 7.39: Surface Pressures Using Coarse Mesh with Transition Model Active

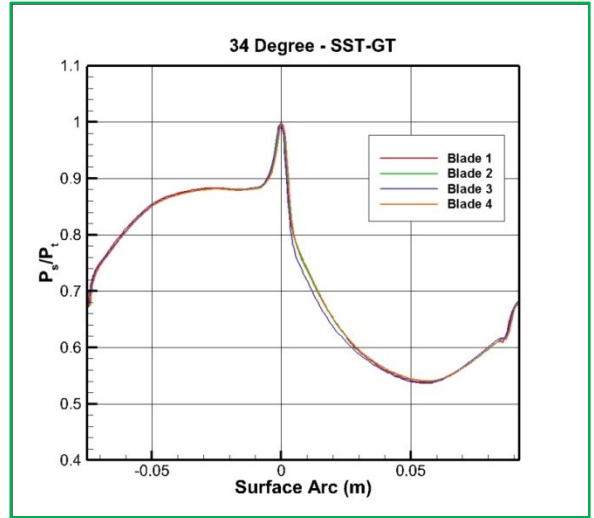


Figure 7.40: Surface Pressures Using Intermediate Mesh with Transition Model Active

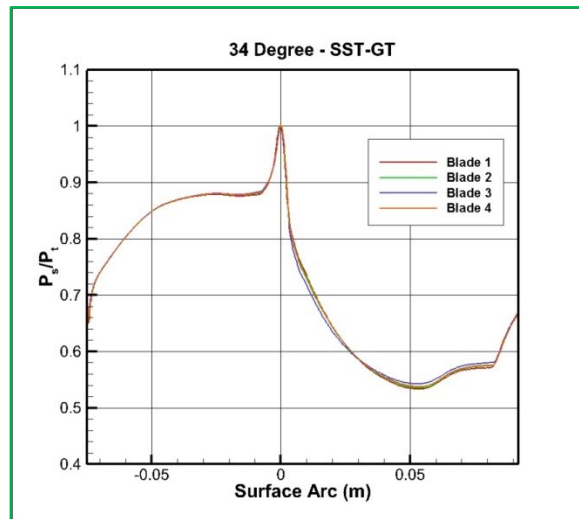


Figure 7.41: Surface Pressures Using Fine Mesh with Transition Model Active

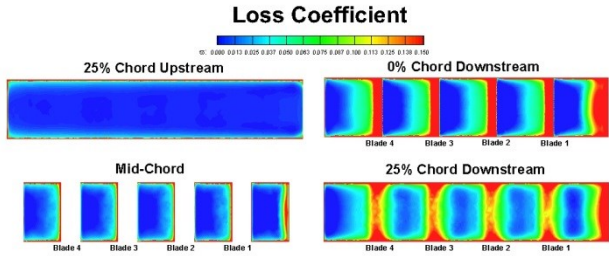


Figure 7.42: Loss Coefficient Contours Using Coarse Mesh

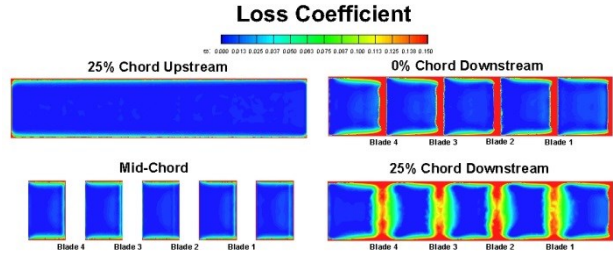


Figure 7.43: Loss Coefficient Contours Using Intermediate Mesh

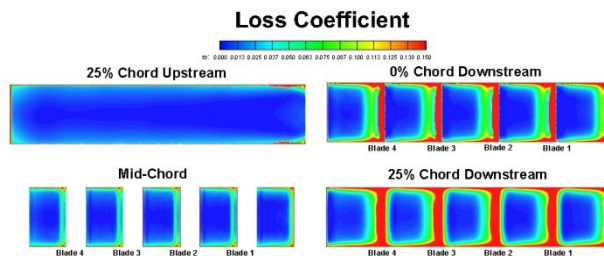


Figure 7.44: Loss Coefficient Contours Using Fine Mesh

### 7.2.3. Preliminary Three Dimensional Simulation Parameters

These preliminary simulations were run before experimental data was available. They were used check the setups and make sure the simulations were ready when the experimental data was available. The cases were setup using the SST turbulence model with the  $\gamma$ - $Re_{\theta}$  transition model. Total pressure and turbulence parameters were specified at the inlet. The outlet had a static pressure condition applied to it. The boundary conditions applied resulted in a Reynolds number based on true chord of  $\sim 420,000$ . This Reynolds number proved satisfactory since it was within the range of the experiments at UND.



## 7.2.4. Preliminary Three Dimensional Simulation Convergence

As with the two dimensional cases, these cases used the ANSYS-CFX solver set to an RMS convergence target of  $1e^{-6}$ . Convergence for all cases ranged between  $1e^{-4}$  -  $1e^{-5}$  for the momentum variables and between  $1e^{-5}$  -  $1e^{-6}$  for the mass variable.

## 7.2.5. Preliminary Three Dimensional Simulation Results

Figure 7.45 - Figure 7.52 show the pressure contours for each of the blade surfaces. For the positive incidence angles all of the blades have very similar loading, which means the flow is periodic from one passage to the next. The negative incidence angles show a slightly different loading on the suction surface of blade number three when compared to the other blades. The higher incidence angles all showed a separation region on the suction surface, with the highest angles of attack having the larger separation region. The lower angles of attack see a smaller amount of separation on the suction surface due to the smaller amount of curvature encountered by the flow. This results in a smaller over-speed region and a smaller separation zone.

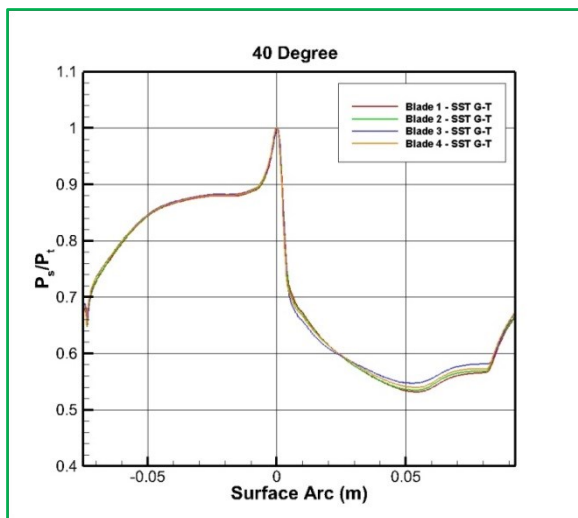


Figure 7.45: 40° Surface Blade Pressures

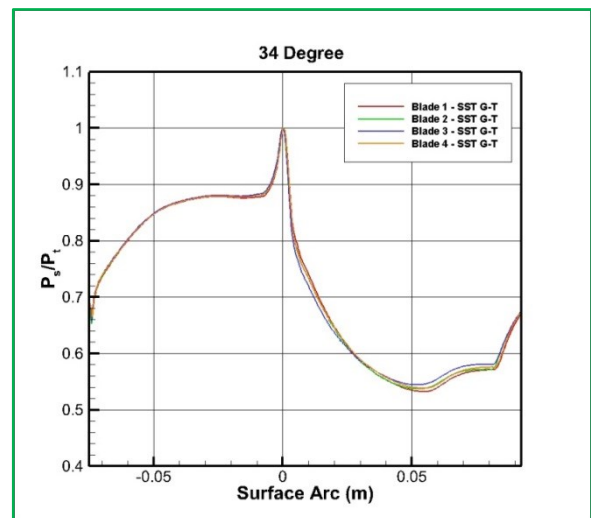


Figure 7.46: 34° Surface Blade Pressures

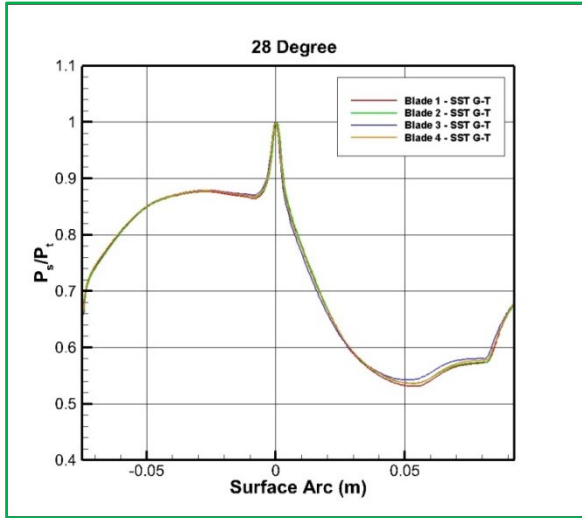


Figure 7.47: 28° Surface Blade Pressures

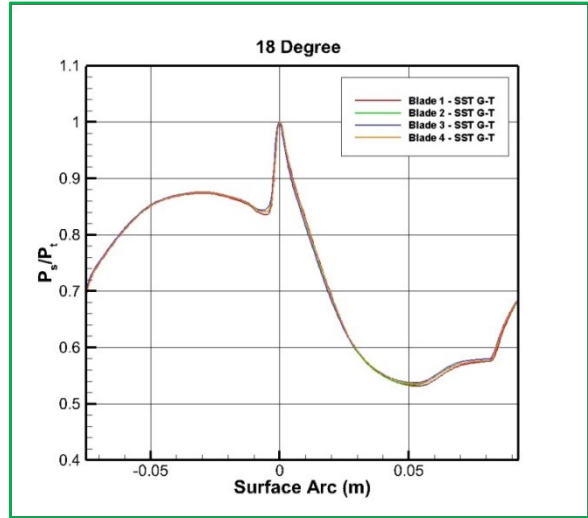


Figure 7.48: 18° Surface Blade Pressures

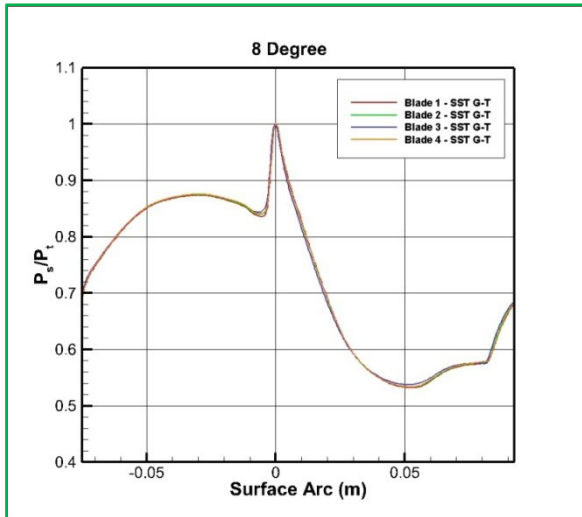


Figure 7.49: 8° Surface Blade Pressures

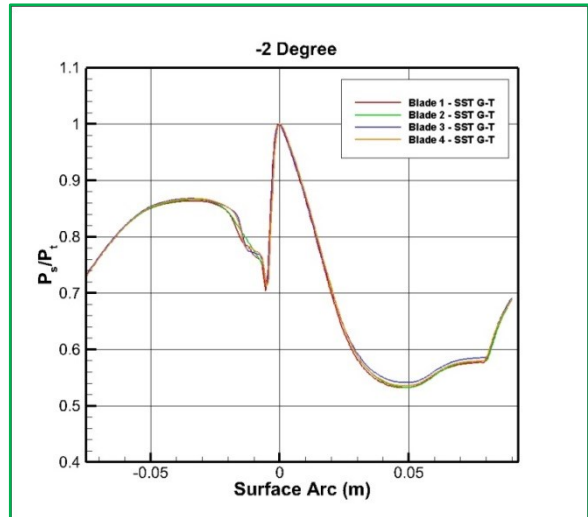


Figure 7.50: -2° Surface Blade Pressures

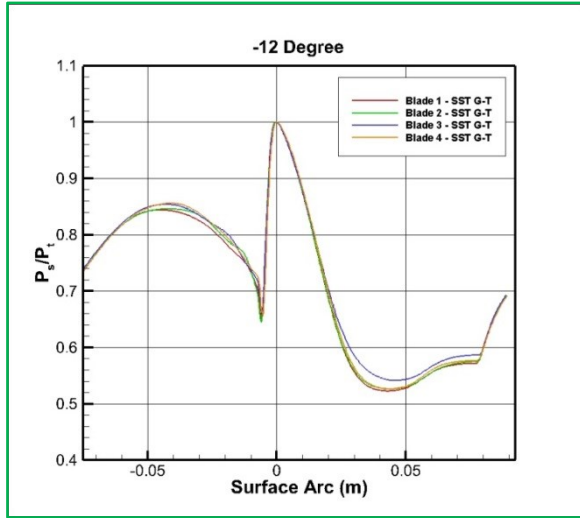


Figure 7.51: -12° Surface Blade Pressures

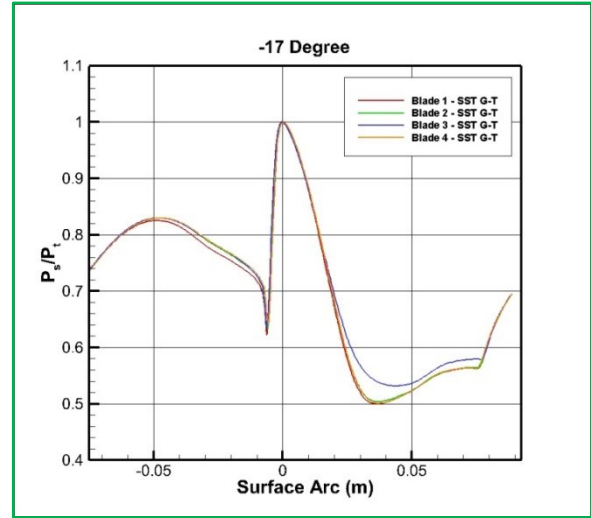


Figure 7.52: -17° Surface Blade Pressures

### 7.2.6. Three Dimensional Simulation of Incident Tolerant Blade Parameters

The simulation parameters were once again chosen to mimic the experimental work being done at UND. The cases were setup using the SST model as the turbulence model and the  $\gamma$ - $Re_{\theta}$  models as the transition model. The inlet conditions and turbulence parameters are identical to the conditions and parameters specified for the two dimensional cases. Pressure data was taken from the two dimensional cases at a location that corresponded to the exit location of the three dimensional geometry. This pressure value was set as the initial outlet pressure. The outlet pressure was then adjusted by incrementally decreasing the back pressure to speed up the flow as to match the experimental Mach number distribution 25% chord downstream of the blade cascade.

### 7.2.7. Three Dimensional Simulation of Incident Tolerant Blade Convergence

As with the preliminary cases, ANSYS-CFX was chosen as the solver with a target RMS convergence level of  $1e^{-6}$ . The Re=50K, 66K, and 228K simulations achieved a final convergence level of  $1e^{-5}$  for all variables. The Re=568K achieved a full convergence.

### 7.2.8. Three Dimensional Simulation of Incident Tolerant Blade Results

Figure 7.54 - Figure 7.57 below show the downstream Mach number calculated at 25% chord downstream. The zero reference in the plot refers to the lower section of the computational domain. This labeling convention is illustrated in Figure 7.53

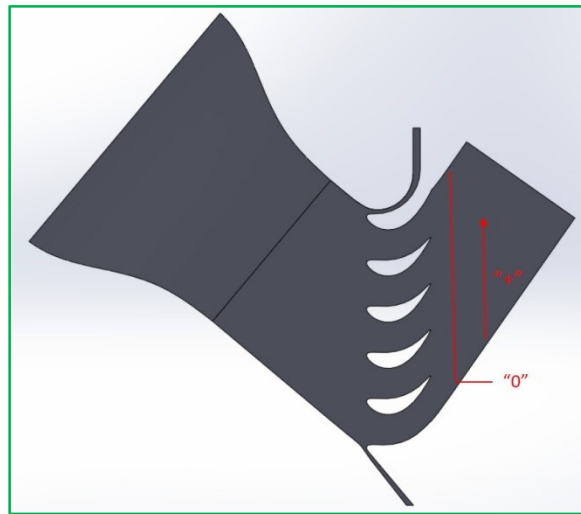


Figure 7.53: Downstream Mach Number Diagram

In all of the cases, the initial back pressure that was specified resulted in a lower downstream Mach number, as shown below in Figure 7.54 - Figure 7.57. The back pressure was adjusted resulting in a downstream Mach number distribution that matches the experimental data very well. The higher Reynolds number cases have some discrepancies in the downstream Mach number, however, the adjusted back pressure created the correct Mach distribution around blade 2; which was the goal of the back pressure correction.

The next set of figures (Figure 7.58 - Figure 7.65) show the surface pressure distributions for all four blades. The pressure surface pressures in each of the cases agree well with the experimental data and with the two dimensional results. However, on the suction surface there is a large spread between each blade in the cascade, especially in the lower Reynolds number cases. This blade to blade variation can be explained by the blockage the flow sees in the blade

passages. This variation decreases with an increase in Reynolds number. For a given Reynolds number, each blade follows the same separation trend but differs in the loading in the lower Reynolds number cases. In all cases, the surface pressures on blade 2 (the instrumented blade) show good agreement on the pressure and suction surface with the experimental data.

Figure 7.66 - Figure 7.73 show Mach contours on the center plane of the domain and a contour of the wall shear in the “x” direction on blade 2. These plots show the over speed regions and the separation regions on the suction surface. The low wall shear values (blue color) on the wall shear contours show the separated region on the suction surface of the blade. The surface pressure plots (mentioned previously) and the wall shear contours make it easy to visualize the shrinking separation region with an increase in Reynolds number. The higher Reynolds number cases show the impact of the endwall on the flowfield around the blade.

The last set of contours (Figure 7.74 - Figure 7.77) show the loss coefficients calculated at 25% chord upstream, mid chord, trailing edge, and 25% chord downstream. The loss coefficient contours show a larger amount of loss in the lower Reynolds number cases when compared to the higher Reynolds number cases. This can be attributed to the larger separation seen in the lower Reynolds number cases. A more periodic trend from passage to passage is seen in the higher Reynolds number cases.

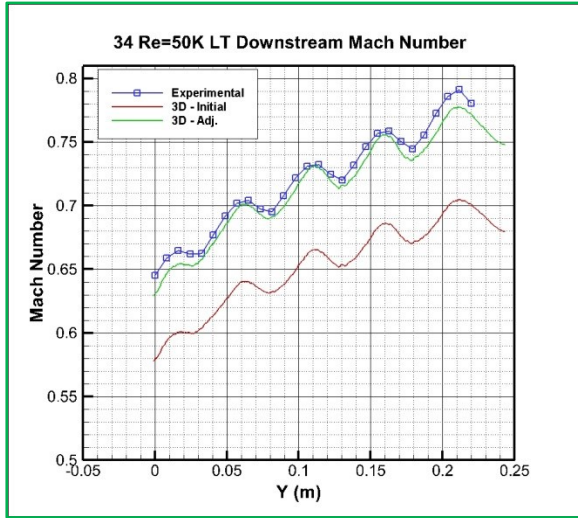


Figure 7.54: 34° Re=50K Initial and Adjusted Downstream Mach Number Comparison

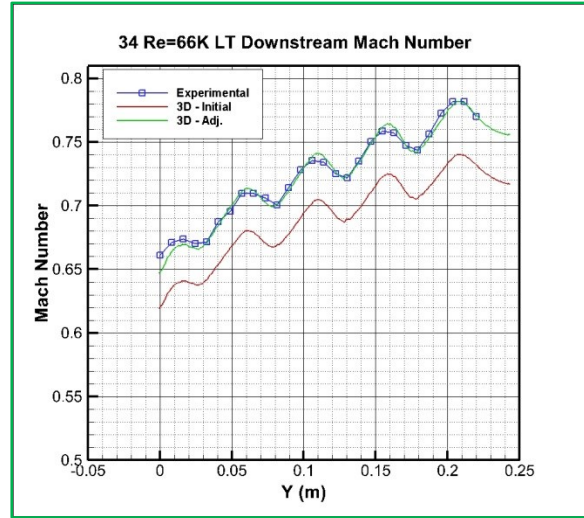


Figure 7.55: Re=66K Initial and Adjusted Downstream Mach Number Comparison

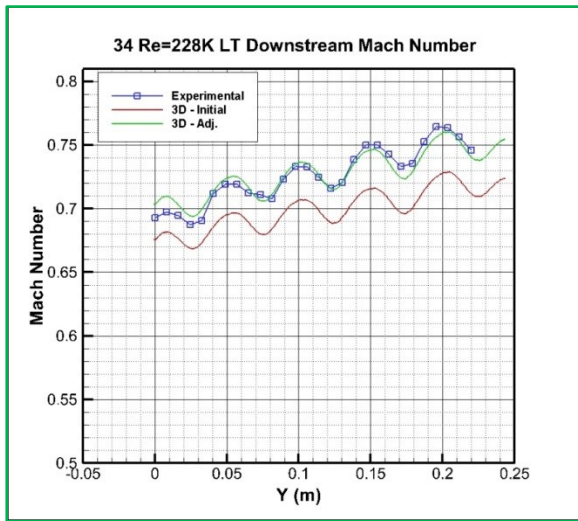


Figure 7.56: 34° Re=228K Initial and Adjusted Downstream Mach Number Comparison

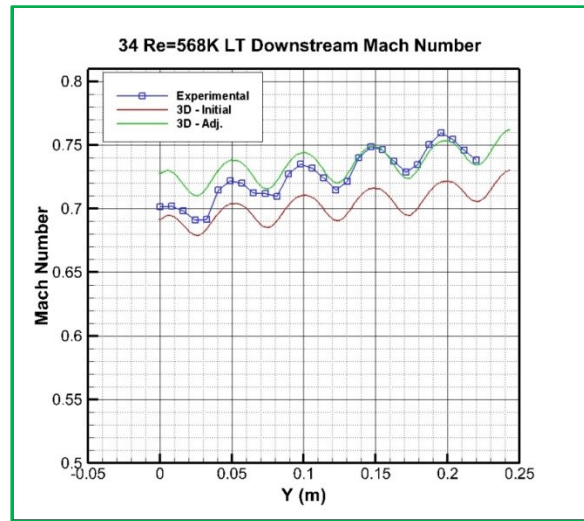


Figure 7.57: Re=568K Initial and Adjusted Downstream Mach Number Comparison

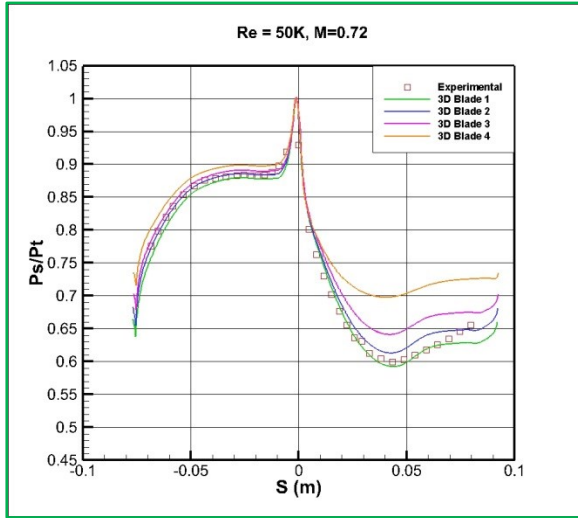


Figure 7.58: Re=50K Blade Surface Pressure Distributions

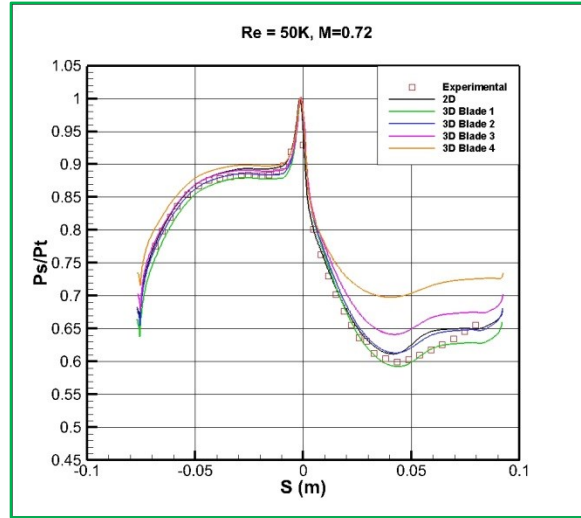


Figure 7.59: Re=50K Blade Surface Pressure Distributions with Two Dimensional Results

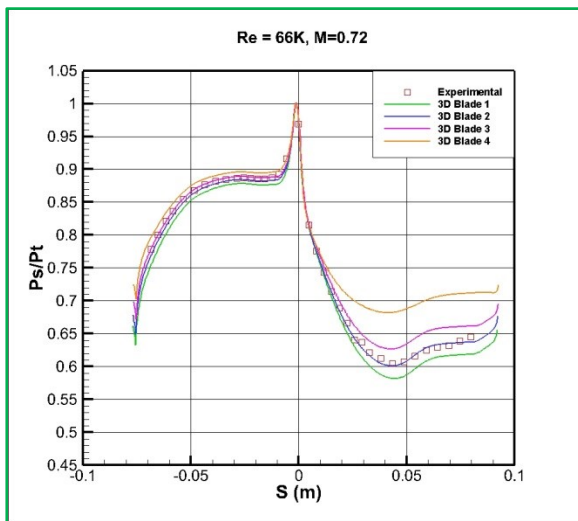


Figure 7.60: Re=66K Blade Surface Pressure Distributions

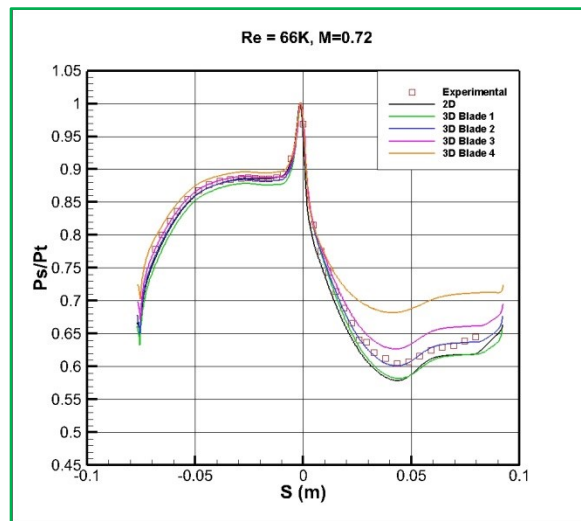


Figure 7.61: Re=66K Blade Surface Pressure Distributions with Two Dimensional Results

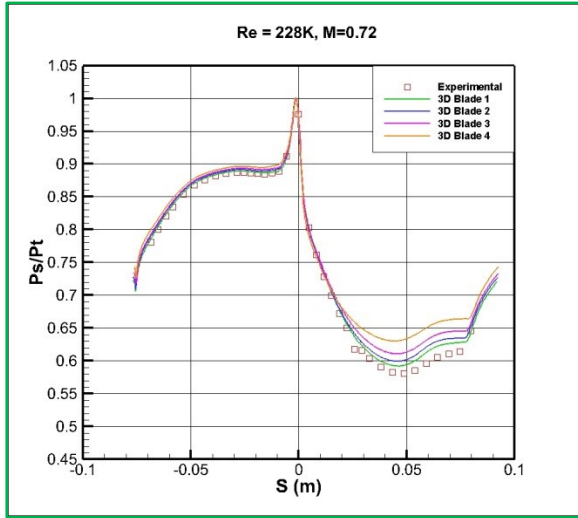


Figure 7.62: Re=228K Blade Surface Pressure Distributions

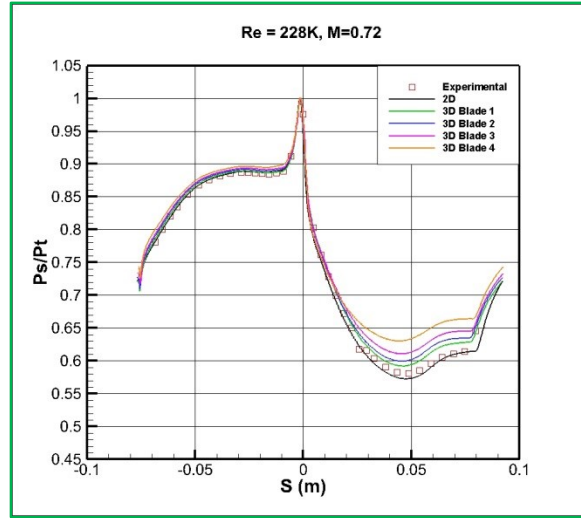


Figure 7.63: Re=228K Blade Surface Pressure Distributions with Two Dimensional Results

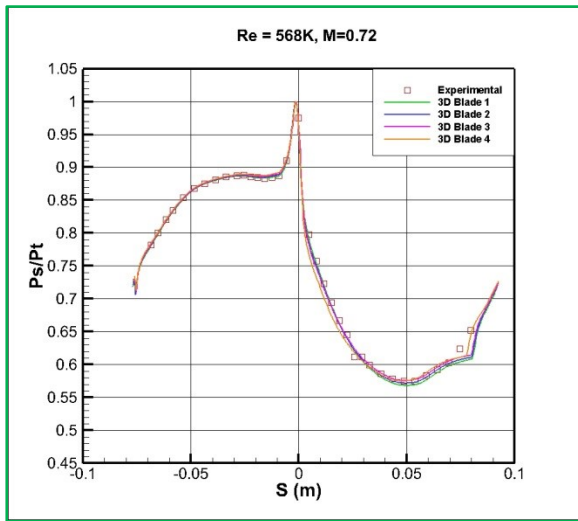


Figure 7.64: Re=568K Blade Surface Pressure Distributions

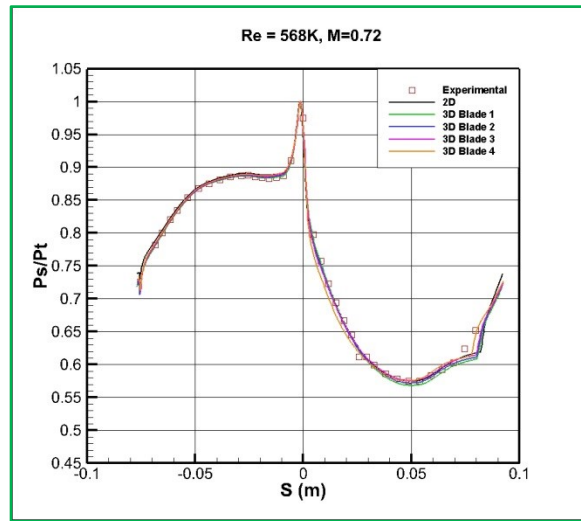


Figure 7.65: Re=568K Blade Surface Pressure Distributions with Two Dimensional Results



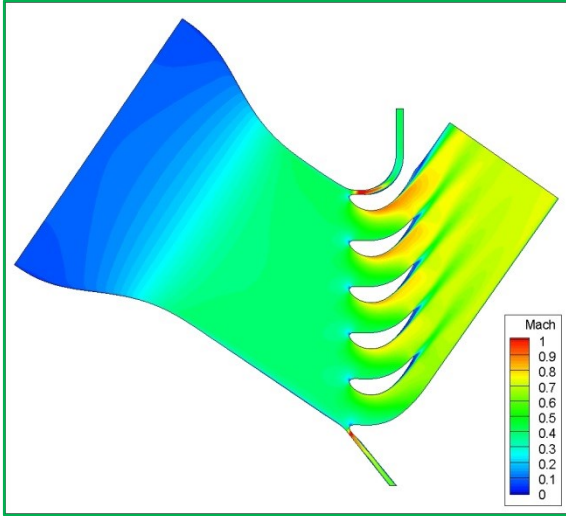


Figure 7.66: Re=50K Center Plane Mach Number Contour

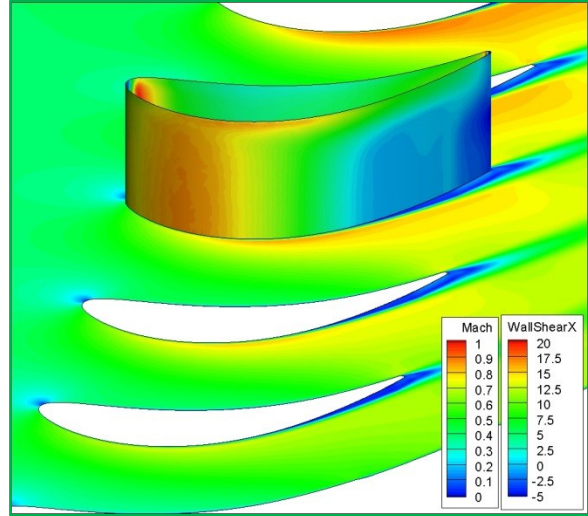


Figure 7.67: Re=50K Center Plane Mach Contour with Wall Shear Contour on Blade 2

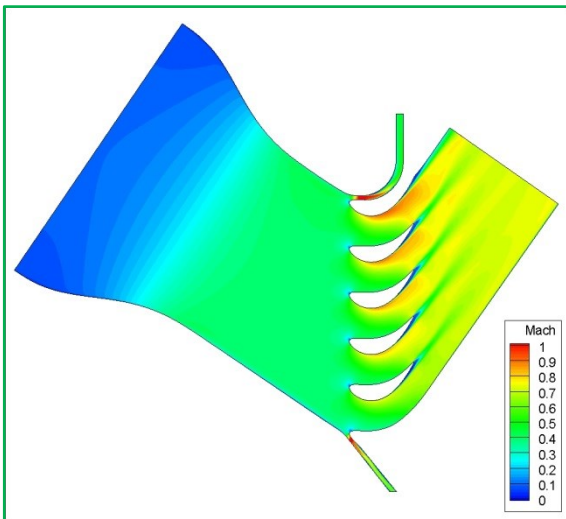


Figure 7.68: Re=66K Center Plane Mach Number Contour

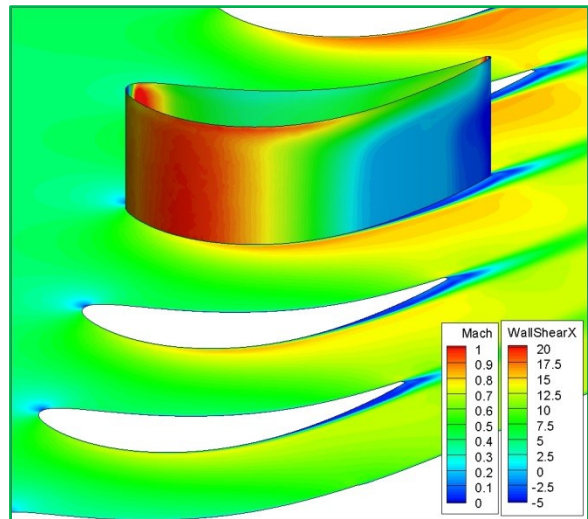


Figure 7.69: Re=66K Center Plane Mach Contour with Wall Shear Contour on Blade 2

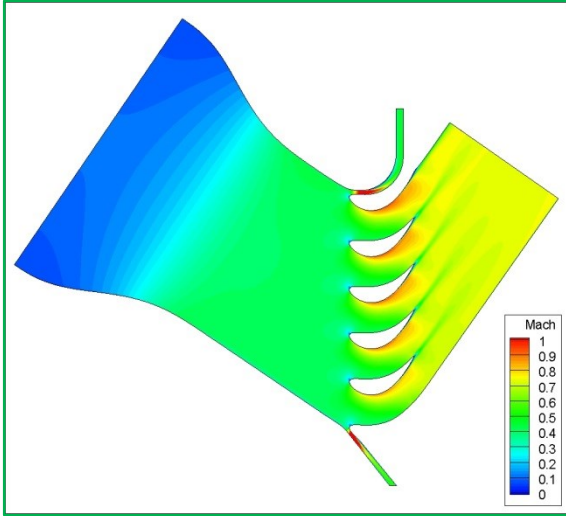


Figure 7.70: Re=228K Center Plane Mach Number Contour

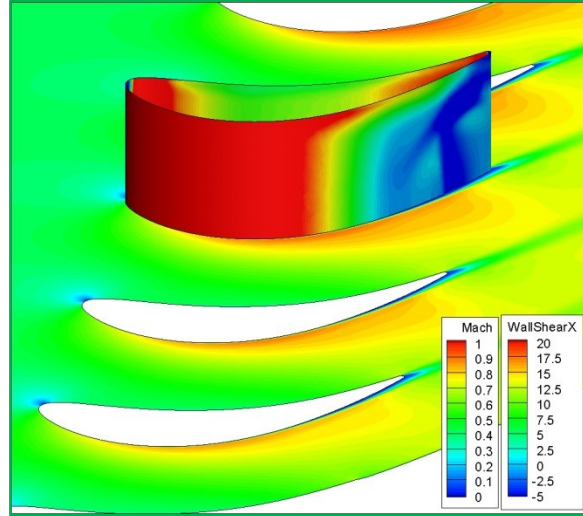


Figure 7.71: Re=228K Center Plane Mach Contour with Wall Shear Contour on Blade 2

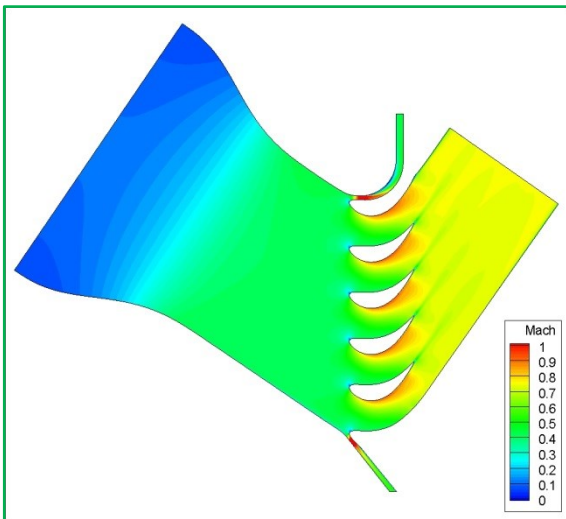


Figure 7.72: Re=568K Center Plane Mach Number Contour

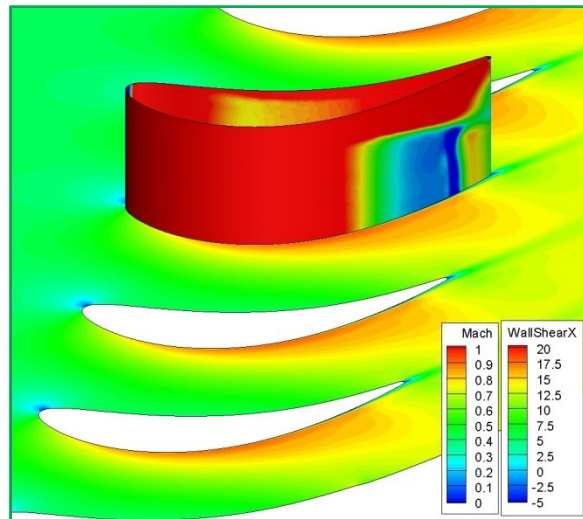


Figure 7.73: Re=568K Center Plane Mach Contour with Wall Shear Contour on Blade 2

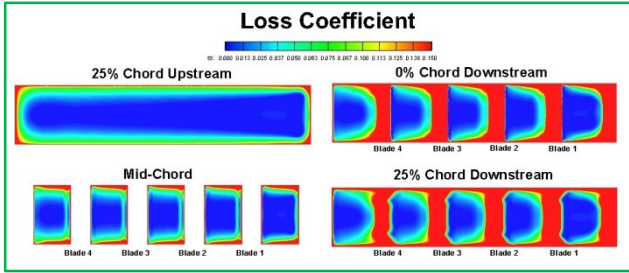


Figure 7.74: Re=50K Loss Coefficients

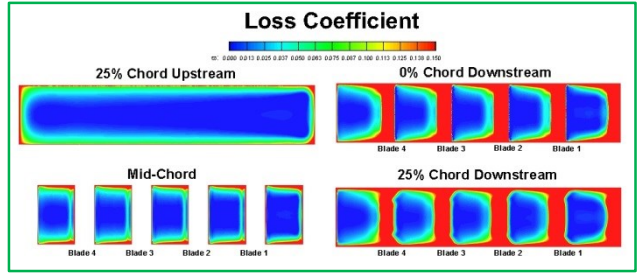


Figure 7.75: Re=66K Loss Coefficients

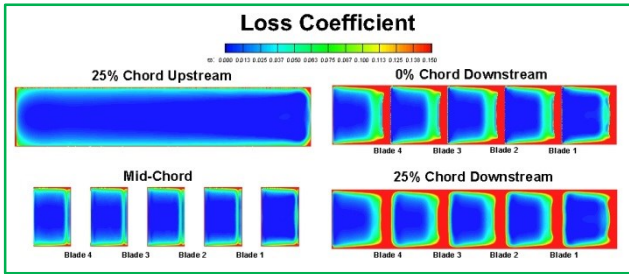


Figure 7.76: Re=228K Loss Coefficients

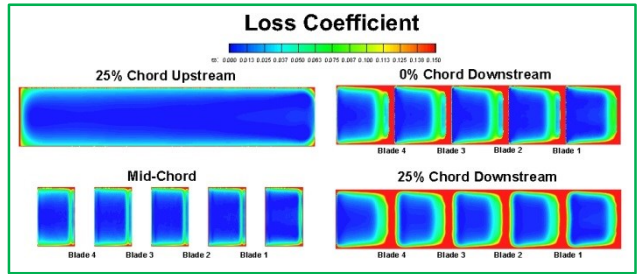


Figure 7.77: Re=568K Loss Coefficients

## 8. CONCLUSIONS AND FUTURE WORK

This section includes the conclusions of the completed work and details the future work to be completed.

### 8.1. Conclusions

Turbulence and transition modeling refinement is crucial in being able to accurately predict flowfields and heat transfer in many different fields of study, including the area of gas turbines. New technologies in aircraft are pushing the need for incident tolerant blade designs. The large incidence angles faced by these designs, and the large separation zones that are being seen, have proven challenging for current turbulence and transition models. New combustor designs are increasing efficiency by increasing the turbulent mixing in the combustors, which is leading to an increase in downstream turbulence levels. This increase in downstream turbulence levels is creating difficulties in predicting the laminar-to-turbulent flow transition that is occurring on turbine vane and blade surfaces. Improving the capabilities of turbulence and transition models will lead to more accurate prediction of aerodynamics and heat transfer values for different vane and blade designs and varying flowfield conditions.

The  $\gamma$ - $Re_{\theta}$  transition model, which has been validated for several incompressible flows, has been shown to produce good results in compressible flows. However, further refinement of this transition model is still needed. In order to refine this model further, initial simulations were conducted to provide a baseline which to compare future results.

The first set of initial computations that were performed looked at flow around a turbine vane. Incompressible flow simulations were run to look at the heat transfer coefficients on the vane surface. These results were then compared to experimental data collected at UND and showed mixed success. The model produced good results at lower Reynolds numbers and lower

turbulence intensities, but over predicted heat transfer values at higher Reynolds numbers and higher turbulence intensities (Kingery, Suzen, & Ames, 2010). Compressible flow simulations were then conducted. The first step in these simulations was to match the blade loadings with the experimental loadings. Once the blade loadings are matched, simulations incorporating heat transfer will be conducted, and the results will then be compared to the experimental data.

Current aerodynamic results show good agreement on the pressure surface of the blade, while the suction surface shows discrepancies which increase with Reynolds number.

The second set of initial computations being performed are looking at the flow over an incident tolerant blade design. This blade design is meant to operate well over a large range of incident angles. Two and three dimensional simulations were conducted using this blade design. The simulations varied the incidence angle from  $+40^\circ$  to  $-17^\circ$  with multiple Reynolds numbers and turbulence intensities at each angle. The two dimensional simulations have so far shown good agreement with the experimental data, with moderate discrepancies on the suction surface at the lower Reynolds numbers. The results from the three dimensional cases show the same discrepancies found in the two dimensional cases as well as variations in the loadings from blade to blade. These variations are found to be larger in the lower Reynolds number cases, where blockage in the blade passages due to separation on the blade surface is seen.

The discrepancies seen in the vane and blade simulations show the need of turbulence and transition refinement in high turbulence and high Reynolds numbers flows. They also show incorporating compressibility effects into the models is warranted.

This thesis provides the mesh, simulation parameters, preliminary results, and processing scripts needed for further simulations and the first steps in the improvement of the turbulence and transition models.

## 8.2. Future Work

To date, experimental data for the 40°, 34°, 8°, -12°, and -17° low turbulence cases has been received. The two dimensional simulations have only been conducted for the 34° and 40° cases, and the three dimensional simulations have only been completed for the 34° low turbulence cases. The rest of the cases will be run and processed continually as new experimental data is received.

Model refinement on the  $\gamma$ - $Re_{\theta}$  transition model will also be conducted. This will consist of employing compressibility factors and other correlations into the model. The new model will then be run and compared with the preliminary cases completed in this thesis.

## 9. REFERENCES

- Ames, F. (1997). The Influence of Large-Scale High Intensity Turbulence on Vane Surface Heat Transfer. *Journal of Turbomachinery*, 23-30.
- Ames, F. E., Argenziano, M., & Wang, C. (2004). Measurement and Prediction of Heat Transfer Distributions on an Aft-Loaded Vane Subjected to the Influence of Catalytic and Dry Low NOx Combustor Turbulence. *Journal of Turbomachinery*, 139-149.
- Ames, F. E., Wang, C., & Barbot, P. A. (2003). Measurement and Prediction of the Influence of Catalytic and Dry Low NOx Combustor Turbulence on Vane Surface Heat Transfer. *Journal of Turbomachinery*, 221-231.
- Anderson, J. (2011). *Fundamentals of Aerodynamics*. McGraw-Hill.
- ANSYS, Inc. (2011). *ANSYS CFX-Solver Theory Guide Release 14.0*.
- Cho, J. R., & Chung, M. K. (1992). A k-e-y Equation Turbulence Model. *Journal of Fluid Mechanics*, 301-322.
- Cutrone, L., Palma, P., Pascazio, G., & Napolitano, M. (2008). Predicting transition in two- and three-dimensional separated flows. *International Journal of Heat and Fluid Flow*, 504-526.
- De Palma, P. (2006). Numerical simulations of three-dimensional transitional compressible flows in turbomachinery cascades. *International Journal of Numerical Methods for Heat & Fluid Flow*, 509-529.
- Dhawan, S., & Narasimha, R. (1958). Some properties of boundary layer flow during the transition from laminar to turbulent motion. *Journal of Fluid Mechanics*, 418-436.
- Glassman, J., Whitney, W., & Steward, W. (1994). *Turbine Design and Application*. NASA SP-290.

- Gostelow, J. P., Blunded, A. R., & Walker, G. J. (1994). Effects of Free-Stream Turbulence and Adverse Pressure Gradients on Boundary Layer Transition. *Journal of Turbomachinery*, 392-404.
- Grotjans, H., & Menter, F. R. (1998). Wall Functions for General Application CFD Codes. *European Computational Fluid Dynamics Conference*.
- Hinze, J. O. (1959). *Turbulence*. New York: McGraw-Hill.
- Hoffman, K. A., & Chiang, S. T. (1998). *Computational Fluid Dynamics*. Wichita, KS: Engineering Education System.
- Huang, J., Corke, T. C., & Thomas, F. O. (2003). Plasma actuators for separation control of low pressure turbine blades. *AIAA Paper AIAA-2003-1027*.
- Kachanov, Y. S. (1994). Physical Mechanisms of Laminar-Boundary-Layer Transition. *Annual Rev. Fluid Mechanis*, 411-482.
- Kaszeta, R. W., Simon, T. W., & Asphis, D. E. (2001). Experimental Investigation of Transition to Turbulence as Affected by Passing Wakes. *ASME Turbo Expo 2001, ASME Paper No. 2001-GT-0195*.
- Kaynak, U. (2012). Transition at Low-Re Numbers for some Airfoils at High Subsonic Mach Numbers. In *Low Reynolds Number Aerodynamics and Transition*. InTech.
- Kingery, L. B., Suzen, Y. B., & Ames, F. E. (2010). Computations of Heat Transfer in Transitional Turbine Flows. *10th AIAA/ASME Joint Thermophysics and Heat Transfer Conference*.
- Kolmogorov, A. N. (1941). Local Structure of Turbulence in Incompressible Viscous Fluid for Very Large Reynolds Numbers. *Doklady Akademiya Nauk SSSR*, 299-303.



- Lake, J. P., King, P. I., & Rivir, R. B. (1999). Reduction of separation losses on a turbine blade with low Reynolds number. *AIAA Paper AIAA-99-0242*.
- Mayle, R. E. (1991). The Role of Laminar-Turbulent Transition in Gas Turbine Engines. *Journal of Turbomachinery*, 509-537.
- Mayle, R. E., & Schulz, A. (1996). The Path to Predicting Bypass Transition. *Journal of Turbomachinery*, 405-411.
- McAuliffe, B. R., & Metin, M. I. (2008). Numerical Study of Instability Mechanisms Leading to Transition in Separation Bubbles. *Journal of Turbomachinery*.
- McAuliffe, B. R., & Metin, M. I. (2010). Transition Mechanisms in Separation Bubbles Under Low- and Elevated- Freestream Turbulence. *Journal of Turbomachinery*.
- McDonough, J. (n.d.). *Introduction to Turbulence Lecture Notes*. Retrieved from <http://www.engr.uky.edu/~acfd/lctr-notes634.pdf>
- Medic, G., & Durbin, P. A. (2002). Toward Improved Prediction of Heat Transfer on Turbine Blades. *Journal of Turbomachinery*, 187-192.
- Menter, F. R. (1994). Two-Equation Eddy-Viscosity Turbulence Models for Engineering Applications. *AIAA*.
- Menter, F. R. (1997). Eddy Viscosity Transport Equations and Their Relation to the k- $\epsilon$  Model. *Journal of Fluids Engineering*, 876-884.
- Menter, F. R. (n.d.). Influence of Freestream Values on k- $\omega$  Turbulence Model Predictions. *AIAA*, 30(6).
- Menter, F. R., & Egorov, Y. (2010). The Scale-Adaptive Simulation Method for Unsteady Turbulent Flow Predictions. Part 1: Theory and Model Description. *Flow Turbulence Combust* (pp. 113-138). Springer Science.

- Menter, F. R., & Langtry, R. B. (2012). Transition Modelling for Turbomachinery Flows. In *Low Reynolds Number Aerodynamics and Transition*. InTech.
- Menter, F. R., Kuntz, M., & Bender, R. (2003). A Scal-Adaptive Simulation Model for Turbulent Flow Predictions. *AIAA*.
- Menter, F. R., Langtry, R. B., Likki, S. R., Suzen, Y. B., Huang, P. G., & Volker, S. (2006). A Correlation Based Transition Model Using Local Variables - Part 2: Test Cases and Industrial Applications. *Journal of Turbomachinery*, 423-434.
- Menter, F. R., Langtry, R. B., Likki, S. R., Suzen, Y. B., Huang, P. G., & Volker, S. (2006). A Correlation-Based Transition Model Using Local Variables - Part 1: Model Formulation. *Journal of Turbomachinery*, 413-422.
- Mihelish, M. P., & Ames, F. E. (2013). The Development of a Closed Loop High Speed Cascade Wind Tunnel for Aerodynamic and Heat Transfer Testing at Moderate to Low Reynolds Numbers. *ASME Turbo Expo*. San Antonio, Texas.
- Morkovin, M. V. (1969). On the many faces of transition. In *Viscous Drag Reduction* (pp. 1-31). New York: Plenum Press.
- NASA. (n.d.). *Goddard Institute for Space Studies*. Retrieved October 2012, from [http://www.giss.nasa.gov/research/briefs/canuto\\_01/](http://www.giss.nasa.gov/research/briefs/canuto_01/)
- Piotrowski, W., Elsner, W., & Drobniak, S. (2010). Transition Prediction on Turbine Blade Profile with Intermittency Transport Equation. *Journal of Turbomachinery*.
- Praisner, T. J., & Clark, J. P. (2007). Predicting Transition In Turbomachinery - Part 1: A Review and New Model Development. *Journal of Turbomachinery*, 1-13.
- Praisner, T. J., & Clark, J. P. (2007). Predicting Transition In Turbomachinery - Part 2: Model Validation and Benchmarking. *Journal of Turbomachinery*, 14-22.

- Richardson, L. F. (1922). *Weather Prediction by Nymerial Process*. Cambridge University Press.
- Savill, A. M. (1993). Some Recent Progress in the Turbulence Modeling of By-pass Transition. In *Near End Wall Flows* (pp. 829-848). Elsevier Sccience Publishers.
- Schlichting, H. (1979). *Boundary Layer Theory*. New York: McGraw-Hill.
- Schubauer, G. B., & Klebanoff, P. S. (1955). Contribution on the Mechanics of Boundary Layer Transition. *NASA TN 3489*.
- Simon, F. F., & Stephens, C. A. (1991). *Modeling of the Heat Transfer in Bypass Transitional Boundary-Layer Flows*. NASA.
- Simon, T. W., Qiu, S., & Yuan, K. (2000). Measurements in a Transitional Boundary Layer Under Low-Pressure Turbine Airfoil Conditions. *NASA-CR-2000-209957*.
- Snyder, C. A. (2012). Preliminary Assessment of Variable Speed Power Turbine Technology on Civil Tiltrotor Size and Performance. *Annual Helicopter Society 68th Annyal Forum*.
- Solomon, W. J., Walker, G. J., & Gostelow, J. P. (1995). Transition Length Prediction for Flows with Rapidly Changing Pressure Gradients. *ASME International Gas Turbine and Aeroengine Congess & Exposition*.
- Spalart, P. R. (2000). Strategies for turbulence modeling and simulations. *International Journal of Heat and Fluid Flow*, 252-263.
- Spalart, P. R., & Strelets, M. K. (2000). Mechanisms of transition and heat transfer in a separation bubble. *Journal of Fluid Mechanics*, 329-349.
- Steelant, J., & Dick, E. (1996). Modelling of Bypass Transition with Conditioned Navier-Stokes Equations Coupled to an Intermittency Equation. *International Journal for Numerical Methods in Fluids*, 193-220.

- Stieger, R. D. (2002). *The Effects of Wakes on Separating Boundary Layers in Low-pressure Turbines* (Vol. PHd dissertatoin). Cambridge University, Engineering Department.
- Suzen, Y. B., & Huang, P. G. (1999). Modeling of Flow Transition Using an Intermittency Transport Equation. *NASA/CR-1999-209313*.
- Suzen, Y. B., & Huang, P. G. (2005). Comprehensive validation of an intermittency transport model for transitional low-pressure turbine flows. *The Aeronautical Journal of the Royal Aeronautical Society*.
- Suzen, Y. B., & Huang, P. G. (2005). Numerical Simulation of Unsteady Wake/Blade Interactions in Low-Pressure Turbine Flows Using an Intermittency Transport Equation. *Journal of Turbomachinery*, 431-444.
- Suzen, Y. B., Huang, P. G., & Ashpis, D. E. (2007). A Computational Fluid Dynamics Study of Transitional Flows in Low-Pressure Turbines Under a Wide Range of Operating Conditions. *Journal of Turbomachinery*, 527-541.
- Suzen, Y. B., Huang, P. G., Hultgren, L. S., & Ashpis, D. E. (2001). Predictions of Separated and Transtional Boundary Layers Under Low-Pressure Turbine Airfoil Conditions Using an Intermittency Transport Equation. *39th AIAA Aerospace Sciences Meeting & Exhibition AIAA 2001-0446*.
- Suzen, Y. B., Xiong, G., & Huang, P. G. (2002). Predictions of Transitional Flows in Low-Pressure Turbines Using Intermittency Transport Equation. *AIA Journal*, 254-266.
- Versteeg, H. K., & Malalasekera, W. (2007). *An Introduction to Computational Fluid Dynamics: The Finite Volume Method*. Pearson Education Limited.
- Vicedo, J., Vilmin, S., Dawes, S., & Savill, A. M. (2004). Intermiency Transport Modeling of Separated Flow Transition. *Journal of Turbomachinery*, 424-431.

- Volino, R. J. (2002). Separated Flow Transition Under Simulated Low-Pressure Turbine Airfoil Conditions - Part 1: Mean Flow and Turbulence Statistics. *Journal of Turbomachinery*, 656-664.
- Volino, R. J. (2002). Separated Flow Transition Under Simulated Low-Pressure Turbine Airfoil Conditions - Part 2: Turbulence Spectra. *Journal of Turbomachinery*, 645-655.
- Walker, G. (1993). The Role of Laminar-Turbulent Transition in Gas Turbine Engines: A Discussion. *Journal of Turbomachinery*, 207-217.
- Wang, L., Fu, S., Carnarius, A., Mockett, C., & Theile, F. (2010). A modular RANS approach for modelling laminar-turbulent transition in turbomachinery flows. *International Journal of Heat and Fluid Flow*.
- Welch, G. E. (2011). Computational Assessment of the Aerodynamic Performance of a Variable-Speed Power Turbine for Large Civil Tilt-Rotor Application. *American Helicopter Society 67th Annual Forum*. Virginia Beach, VA.
- White, F. (2006). *Viscous Fluid Flow*. McGraw-Hill.
- Wilcox, D. (2000). *Turbulence Modeling for CFD*. DCW Industries, Inc.

# APPENDIX

## A.1. MATLAB Script for Creating Two Dimensional Geometry

```
%Jamison Huber
%Reads in Blade Points and Creates Outer Boundaries

clear all;
clc;
close all;

%Reads in Blade Points, Finds Pitch, and
%separates blade data into top and bottom
%Specifies Inlet AOA
blade2=dlmread('Blade2_XY.txt');
blade3=dlmread('Blade3_XY.txt');
pitch=blade2(1,2)-blade3(1,2);
axialchord=max(blade3)-min(blade3);
axialchord=axialchord(1,1);
[C,l]=min(blade2);
blade2lower=blade2(1:l(1),:);
blade2upper=blade2((l(1)+1):length(blade2),:);
blade2lower(24,:)=[];

inletAOA=40;

%Removes end of curves for upper blade surface
i=1;
blade2upper=sortrows(blade2upper,1);
while blade2upper(i+1,2)-blade2upper(i,2)>=0
    i=i+1;
end
blade2uppermod=blade2upper;
blade2uppermod(1:i,:)=[];

i=1;
blade2uppermod=sortrows(blade2uppermod,-1);
while blade2uppermod(i+1,2)-blade2uppermod(i,2)>=0
    i=i+1;
end
blade2uppermod(1:i+30,:)=[];

%Adds outlet line
outletlength=2*axialchord;
outletslope=(blade2uppermod(1,2)-blade2uppermod(2,2))...
    /(blade2uppermod(1,1)-blade2uppermod(2,1));
outletline=[blade2uppermod(1,1)+outletlength,...
    (blade2uppermod(1,2)+(outletlength*outletslope))];
blade2uppermod=[outletline;blade2uppermod];
```

```

%Adds inlet line
blade2uppermod=sortrows(blade2uppermod,1);
num=400;
inletlength=axialchord;
points=linspace((inletlength/num),inletlength,num);
inletslope=(blade2uppermod(1,2)-blade2uppermod(2,2))...
/(blade2uppermod(1,1)-blade2uppermod(2,1));
for i=1:length(points)
    point=points(i);
    inletline(i,:)=[blade2uppermod(1,1)-(point*(cosd(inletAOA)+inletslope)),...
        blade2uppermod(1,2)+(point*(sind(inletAOA)+inletslope))];
end
inletline=sortrows(inletline,1);
blade2uppermod=[inletline;blade2uppermod];

%Smoothes inlet/blade connection
i=num+1;
for j=0:305
    for m=0:j
        blade2uppermod(i-m,:)=(blade2uppermod(i-(m+1),:)+blade2uppermod(i-(m-1),:))/2;
        blade2uppermod(i+m,:)=(blade2uppermod(i+(m+1),:)+blade2uppermod(i+(m-1),:))/2;
    end
end

%Creates upper and lower boundaries and trims upper boundary inlet
tempx=blade2uppermod(:,1);
tempy=blade2uppermod(:,2);
tempyupper=tempy+(pitch/4);
tempylower=tempyupper-pitch;
tempz=zeros(length(tempx),1);
upperboundary=[tempx,tempyupper,tempz];
lowerboundary=[tempx,tempylower,tempz];
blade2=[blade2upper;blade2lower;blade2upper(1,:)];
tempz=zeros(length(blade2),1);
blade2=[blade2,tempz];

%Adds on to inlet length
% sum=0;
% i=1;
% while sum<pitch*cosd(90-inletAOA)
%     sum=sum+sqrt(((upperboundary(i+1,1)-upperboundary(i,1))^2+...
%         (upperboundary(i+1,2)-upperboundary(i,2))^2));
%     i=i+1;
% end
% upperboundary(1:i,:)=[];

hold on
plot(upperboundary(:,1),upperboundary(:,2));
plot(lowerboundary(:,1),lowerboundary(:,2));
plot(blade2(:,1),blade2(:,2));

```

```
fid=fopen('Blade2Points.txt','w');
fprintf(fid, '%f\t%f\t%f\r\n',blade2);
fclose(fid);
fid=fopen('40_UpperBoundaryPoints.txt','w');
fprintf(fid, '%f\t%f\t%f\r\n',upperboundary);
fclose(fid);
fid=fopen('40_LowerBoundaryPoints.txt','w');
fprintf(fid, '%f\t%f\t%f\r\n',lowerboundary);
fclose(fid);
```



## A.2. MATLAB Script for Creating Three Dimensional Case Plots

```
%Jamison Huber
%Reads in data from all blades and outputs pressure distribution .txt files
%%Also outputs Cp distributions

clear all;
clc;

%Number of blades in cascade
numblades=4;

%Domain & Total Pressures
domain_pressure=5425.04886;
total_pressure=7691.12;

%Manuall enter downstream pressures for Blades 1-4
static_pressure=[-124.864, -38.34, 57.49, 177.128];

%Reads in Data from .txt files
for i=1:numblades
    filename1=sprintf('Blade_%d_X_vs_Pressure.txt',i);
    filename2=sprintf('Blade_%d_Y_vs_WallShear.txt',i);
    X_vs_Pressure_Temp=dlmread(filename1, ',',5,0);
    Y_vs_WallShear_Temp=dlmread(filename2, ',',5,0);
    eval(['Blade' num2str(i) ' _X_Pressure=X_vs_Pressure_Temp;']);
    eval(['Blade' num2str(i) ' _Y_WallShear=Y_vs_WallShear_Temp;']);
end

%Splits data up by blade number
%Format is X Y Pressure WallShear
for i=1:numblades
    eval(['Blade' num2str(i) ' _Data(:,1)=Blade' num2str(i) ' _X_Pressure(:,1);']);
    eval(['Blade' num2str(i) ' _Data(:,3)=Blade' num2str(i) ' _X_Pressure(:,2);']);
    eval(['Blade' num2str(i) ' _Data(:,2)=Blade' num2str(i) ' _Y_WallShear(:,1);']);
    eval(['Blade' num2str(i) ' _Data(:,4)=Blade' num2str(i) ' _Y_WallShear(:,2);']);
    eval(['[C,l]=max(Blade' num2str(i) ' _Data,[],1);']);
    maxX(i)=C(1);
    maxXLocation(i)=l(1);
end

%Rearranges data
for i=1:numblades
    eval(['tempup=Blade' num2str(i) ' _Data(1:maxXLocation(' num2str(i)...
        '-1,:);']);
    eval(['templo=Blade' num2str(i) ' _Data(maxXLocation(' num2str(i)...
        '):length(Blade' num2str(i) ' _Data,:);']);
    eval(['Blade' num2str(i) ' _Data_Sorted=[templo;tempup;']);
end
```

```

%Calculates S
for i=1:numblades
    eval(['C,I]=min(Blade' num2str(i) '_Data_Sorted,[],1);');
    eval(['Blade_Sorted_Slope=(Blade' num2str(i) '_Data_Sorted(:,1:2));']);
    for n=1:length(Blade_Sorted_Slope)

        if i == 1
            xlow=-0.0197;
            xhigh=-0.0193;
            ylow=-0.0543;
            yhigh=-0.0537;
            if Blade1_Data_Sorted(n,1)>xlow && Blade1_Data_Sorted(n,1)<xhigh
                if Blade1_Data_Sorted(n,2)>ylow && Blade1_Data_Sorted(n,2)<yhigh
                    tap_index=n;
                    break
                end
            end
        end

        if i == 2
            xlow=-0.0197;
            xhigh=-0.0193;
            ylow=-0.1032;
            yhigh=-0.1027;
            if Blade2_Data_Sorted(n,1)>xlow && Blade2_Data_Sorted(n,1)<xhigh
                if Blade2_Data_Sorted(n,2)>ylow && Blade2_Data_Sorted(n,2)<yhigh
                    tap_index=n;
                    break
                end
            end
        end

        if i == 3
            xlow=-0.0197;
            xhigh=-0.0193;
            ylow=-0.1519;
            yhigh=-0.1514;
            if Blade3_Data_Sorted(n,1)>xlow && Blade3_Data_Sorted(n,1)<xhigh
                if Blade3_Data_Sorted(n,2)>ylow && Blade3_Data_Sorted(n,2)<yhigh
                    tap_index=n;
                    break
                end
            end
        end

        if i == 4
            xlow=-0.0197;
            xhigh=-0.0193;
            ylow=-0.2008;
            yhigh=-0.2005;
            if Blade4_Data_Sorted(n,1)>xlow && Blade4_Data_Sorted(n,1)<xhigh

```

```

        if Blade4_Data_Sorted(n,2)>ylow && Blade4_Data_Sorted(n,2)<yhigh
            tap_index=n;
            break
        end
    end
end
end

end

tap_location(i)=tap_index;
eval(['utemp=sum(Blade' num2str(i) '_Data_Sorted(1:tap_location('...
    num2str(i) '),3));']);
eval(['ltemp=sum(Blade' num2str(i) '_Data_Sorted(tap_location('...
    num2str(i) '):length(Blade' num2str(i) '_Data_Sorted),3));']);
eval(['Blade' num2str(i) '_Data_Sorted(tap_location(' ...
    num2str(i) '),5)=0;']);

if utemp>ltemp
    fprintf('Upper - \n')
    for j=tap_location(i):-1:2
        eval(['Blade' num2str(i) '_Data_Sorted(j-1,5)=-((((abs(Blade' ...
            num2str(i) '_Data_Sorted(j,1)-Blade' num2str(i) ...
            '_Data_Sorted(j-1,1))^2)+(abs(Blade' num2str(i) ...
            '_Data_Sorted(j,2)-Blade' num2str(i) ...
            '_Data_Sorted(j-1,2))^2))^0.5)+abs(Blade' num2str(i)...
            '_Data_Sorted(j,5));']);
    end
    eval(['datalength=length(Blade' num2str(i) '_Data_Sorted);']);
    for j=tap_location(i):datalength-1
        eval(['Blade' num2str(i) '_Data_Sorted(j+1,5)=-((((abs(Blade'...
            num2str(i) '_Data_Sorted(j+1,1)-Blade' num2str(i) ...
            '_Data_Sorted(j,1))^2)+(abs(Blade' num2str(i) ...
            '_Data_Sorted(j+1,2)-Blade' num2str(i) ...
            '_Data_Sorted(j,2))^2))^0.5)+abs(Blade' num2str(i)...
            '_Data_Sorted(j,5));']);
    end
else
    fprintf('Lower - \n')
    for j=tap_location(i):-1:2
        eval(['Blade' num2str(i) '_Data_Sorted(j-1,5)=-((((abs(Blade' ...
            num2str(i) '_Data_Sorted(j,1)-Blade' num2str(i)...
            '_Data_Sorted(j-1,1))^2)+(abs(Blade' num2str(i)...
            '_Data_Sorted(j,2)-Blade' num2str(i) ...
            '_Data_Sorted(j-1,2))^2))^0.5)+abs(Blade' num2str(i) ...
            '_Data_Sorted(j,5));']);
    end
    eval(['datalength=length(Blade' num2str(i) '_Data_Sorted);']);
    for j=tap_location(i):datalength-1
        eval(['Blade' num2str(i) '_Data_Sorted(j+1,5)=-((((abs(Blade'...
            num2str(i) '_Data_Sorted(j+1,1)-Blade' num2str(i) ...
            '_Data_Sorted(j,1))^2)+(abs(Blade' num2str(i)...

```

```

        '_Data_Sorted(j+1,2)-Blade' num2str(i)...
        '_Data_Sorted(j,2))^2)^0.5)+abs(Blade' num2str(i)...
        '_Data_Sorted(j,5));'];
    end
end
end

%Calculates Ps/Pt
for i=1:numblades
    eval(['Blade' num2str(i) '_Data_Sorted(:,6)=(Blade' num2str(i) ...
        '_Data_Sorted(:,3)+' num2str(domain_pressure) ')' ...
        num2str(total_pressure) ');']);
end

%Calculates Cp
%Cp=(P - Pt)/(Pt-Pexit_static)
for i=1:numblades
    eval(['Blade' num2str(i) '_Data_Sorted(:,7)=((Blade' num2str(i) ...
        '_Data_Sorted(:,3)+' num2str(domain_pressure) ')-(' ...
        num2str(total_pressure) '))/(' num2str(total_pressure) ')-(' ...
        num2str(static_pressure(i) '+' num2str(domain_pressure) ');']);
end

%Output Plotting Files (.txt)
for i=1:numblades
    %Outputting Ps/Pt Files
    eval(['Blade' num2str(i) '_Data_Sorted_Plot=Blade' num2str(i) ...
        '_Data_Sorted(:,5:6);']);
    filename1=sprintf('S vs PsPt Blade%d.txt',i);
    filename2=eval(['Blade' num2str(i) '_Data_Sorted_Plot']);
    fid=fopen(filename1, 'w');
    fprintf(fid,'%f\t%f\n', filename2);
    fclose(fid);
    %Outputting Cp Files
    eval(['Blade' num2str(i) '_Data_Sorted_Plot_Cp=Blade' num2str(i) ...
        '_Data_Sorted(:,[5,7]);']);
    filename1=sprintf('S vs Cp Blade%d.txt',i);
    filename2=eval(['Blade' num2str(i) '_Data_Sorted_Plot_Cp']);
    fid=fopen(filename1, 'w');
    fprintf(fid,'%f\t%f\n', filename2);
    fclose(fid);
end

%Plotting
hold on
axis equal
plot(Blade1_Data_Sorted(:,1),Blade1_Data_Sorted(:,2),'-go');
[C,l]=min(Blade1_Data_Sorted,[],1);
minx=Blade1_Data_Sorted(l(1),1);
miny=Blade1_Data_Sorted(l(1),2);
plot(minx,miny,'--rs')

```

```
tapx=Blade1_Data_Sorted(tap_location(1),1);
tapy=Blade1_Data_Sorted(tap_location(1),2);
plot(tapx,tapy,'--ko')
```

```
hold on
axis equal
plot(Blade2_Data_Sorted(:,1),Blade2_Data_Sorted(:,2),'-go');
[C,I]=min(Blade2_Data_Sorted,[],1);
minx=Blade2_Data_Sorted(I(1),1);
miny=Blade2_Data_Sorted(I(1),2);
plot(minx,miny,'--rs')
tapx=Blade2_Data_Sorted(tap_location(2),1);
tapy=Blade2_Data_Sorted(tap_location(2),2);
plot(tapx,tapy,'--ko')
```

```
hold on
axis equal
plot(Blade3_Data_Sorted(:,1),Blade3_Data_Sorted(:,2),'-go');
[C,I]=min(Blade3_Data_Sorted,[],1);
minx=Blade3_Data_Sorted(I(1),1);
miny=Blade3_Data_Sorted(I(1),2);
plot(minx,miny,'--rs')
tapx=Blade3_Data_Sorted(tap_location(3),1);
tapy=Blade3_Data_Sorted(tap_location(3),2);
plot(tapx,tapy,'--ko')
```

```
hold on
axis equal
plot(Blade4_Data_Sorted(:,1),Blade4_Data_Sorted(:,2),'-go');
[C,I]=min(Blade4_Data_Sorted,[],1);
minx=Blade4_Data_Sorted(I(1),1);
miny=Blade4_Data_Sorted(I(1),2);
plot(minx,miny,'--rs')
tapx=Blade4_Data_Sorted(tap_location(4),1);
tapy=Blade4_Data_Sorted(tap_location(4),2);
plot(tapx,tapy,'--ko')
```